University College London

Department of Electrical and Electronics Engineering

PhD Thesis

“Integrated photonics for millimetre wave transmitters and receivers”

By

Ahmad Wasfi Mahmoud Mohammad

Supervised by

Prof. Cyril C. Renaud

Prof. John E. Mitchell

‘I, Ahmad Wasfi Mahmoud Mohammad, confirm that the work presented in this thesis is my own. Where information has been derived from other sources, I confirm that this has been indicated in the thesis'.

February 2019

To the memory of

my mother

Wajiha Rushdi Mohammad

Abstract

This PhD thesis entitled “Integrated photonics for millimetre wave transmitters and receivers” aimed at investigating the possibility of employing the uni-traveling carrier photodiode (UTC-PD) in millimetre wave (MMW) wireless receivers and, eventually, demonstrating a photonic integrated transceiver, by exploiting the concept of optically-pumped mixing (OPM).

Previously, the UTC-PD has been successfully demonstrated as an OPM, by mixing an optically-generated local oscillator (LO) with a high frequency RF signal to generate a replica of the RF signal at a low intermediate frequency (IF), defined by the difference between the LO and the RF signal.

This concept forms the foundation of this PhD thesis. The principal idea is to deploy the UTC-PD mixer in MMW wireless receivers to down-convert the high frequency data signal into a low frequency IF, where it can be easily processed and recovered.

The main challenge to this approach is the low conversion efficiency of the UTC-PD mixer. For example, a conversion loss of 32 dB has been reported at 100 GHz. Also, the detection bandwidth in previous demonstrations was very narrow (around 100 Hz), which is too narrow to be useful in high-speed data communications. Consequently, a significant effort was made, in this thesis, to improve these parameters before the implementation in wireless receivers.

The characterization and optimization works done in this thesis on the input parameters to the UTC-PD mixer have advanced the state of the art significantly. For example, conversion losses as low as 22 dB have been reported here. Also, the detection bandwidth has been increased to up to 10 GHz, allowing for multi-Gbps communication links.

Based on these promising results, proof of concept wireless data transmission experiments were successfully conducted at different carrier frequencies (33 GHz, 35 GHz, and 60 GHz) using separate non-integrated UTC-PDs at the receiver with speeds of up to 5 Gbps. To the best of the author's knowledge, this is the first demonstration of the UTC-PD at the receiver.

Upon these successful demonstrations, further research was done on a photonic integrated circuit, which comprises UTC-PDs, lasers, optical amplifiers and modulators. The outcome of this research was the first demonstration of a photonic integrated transceiver.

This transceiver is suitable for short distance communications and could find interesting applications in 5G and future networks, including: high definition (HD) video streaming, file transfer, and wireless backhaul.

Impact Statement

The demand for higher speeds in data communications has been growing dramatically in recent years. Consequently, the international telecommunications union (ITU) proposed the fifth generation of mobile communications systems (5G) to cope with the foreseen demands in the coming few years. The requirements set by the ITU for 5G include orders of magnitude improvement on the data rates, latency, connection density and network efficiency compared to the current 4G technologies.

For 5G to be able to deliver such high speeds it will rely heavily on the MMW technology as it contains multi-gigahertz-wide chunks of unutilized frequency bands. With the recent advancements in complementary metal oxide semiconductor (CMOS) technology, MMW transceivers became commercially available. However, such transceivers are, generally, not tuneable, which makes them less flexible in terms of frequency of operation. On the other hand, photonic technologies have shown excellent performance as MMW transmitters using optical heterodyning on photomixers such as the UTC-PD, which can generate widely tuneable MMW signals simply by adjusting the spacing between the optical LO tones. This offers flexibility on the frequency of operation and simplifies the architecture in multicast systems, for example. However, the large conversion loss of the UTC-PD as an optoelectronic mixer (32 dB at 100 GHz) has been a significant obstacle to its utilization in MMW receivers.

Throughout this PhD work, several novel contributions have been made. Firstly, the characterization and optimization works on the input parameters of the UTC-PD mixer (optical power, bias voltage, and frequency) have improved the state of the art in terms of the conversion efficiency and detection bandwidth.

For example, the best conversion loss reported here is 22 dB compared to 32 dB reported previously. Also, the detection bandwidth in the previous demonstrations was limited to 100 Hz, which is not enough for high-speed data communications, while 10 GHz of detection bandwidth has been reported here, which allowed for multi-Gbps communication links.

Secondly, wireless communication links implementing UTC-PDs at the receiver have been successfully realized at 35 GHz, 33.5 GHz, and 60 GHz with speeds of 5 Gbps, 2 Gbps and 1 GHz, respectively, using different modulation formats. To the best of the author's knowledge, this is the first implementation of the UTC-PD in wireless receivers.

Thirdly, the first demonstration of a photonic integrated transceiver has been reported here. In the transmitter mode, the transceiver operates with 1 Gbps speed and 0.5 meters of wireless distance, while it operates with 500 Mbps speed and 3 meters of wireless distance in the receiver mode.

To the best of the author's knowledge, this is the first demonstration of a photonics integrated transceiver. As an integrated solution, this transceiver provides reduction in size, weight, and power consumption, compared to the non-integrated solutions. Also, being a photonic transceiver allows for its integration with the high-speed fibre networks [1], which is beneficial to 5G as it provides low signal-transport losses (typically, 0.4 dB/km at 1550 nm [2]), high-capacity (up to 500 Gbps/wavelength [3]), low-latency links (typically, 5 μs/km at 1550 nm [4]), and immunity against electromagnetic interference. Further, it simplifies the access network since it allows for the separation of the signal generation unit and the radio access units.

The transceiver works at around 60 GHz, which is a candidate frequency for 5G. At this frequency band, atmospheric absorption is high, which limits the propagation distance. This is advantageous in cellular communications as it reduces the interference between neighbouring cells, allows for frequency reuse and offers more security.

Therefore, this transceiver is suitable for short distance communications and could find interesting applications in 5G and future networks, including: high definition (HD) video streaming, file transfer, and wireless backhaul.

Finally, an experimental investigation on photonic-electronic hybrid receivers at 60 GHz, with a wireless distance of 3 meters and a speed of 1 Gbps, has shown that hybrid integration is a viable solution to overcome the limitations of electronics and photonics, and to benefit from advantages offered by both technologies.

List of Publications

Peer-reviewed journal publications:

1. **Ahmad W. Mohammad**, Haymen Shams, Katarzyna Balakier, Chris Graham, Michele Natrella, Alwyn J. Seeds, and Cyril C. Renaud, “5 Gbps wireless transmission link with an optically pumped uni-traveling carrier photodiode mixer at the receiver,” Opt. Express 26, pp. 2884-2890 (2018).
2. **Ahmad W. Mohammad,** Haymen Shams, Chin-Pang Liu, Chris Graham, Michele Natrella, Alwyn J. Seeds, and Cyril C. Renaud, "60 GHz Transmission Link using Uni-Travelling Carrier Photodiodes at the Transmitter and the Receiver", J. Lightw. Technol., vol. 36, no. 19, pp. 4507-4513, Oct.1, 2018. doi: 10.1109/JLT.2018.2849938.

Conference publications:

1. **Ahmad W. Mohammad**, Haymen Shams, Chin-Pang Liu, Katarzyna Balakier, Chris Graham, Michele Natrella, Alwyn J. Seeds, and Cyril C. Renaud, “1 Gbaud QPSK wireless receiver using an opto-electronic mixer,” Proc. IEEE Topical Meeting Microw. Photon., pp. 1-3 (2017).
2. **Ahmad W. Mohammad**, Andrzej Jankowski, Frederic van Dijk, and Cyril C. Renaud, “Optically Pumped Mixing in Photonically Integrated Uni-Travelling Carrier Photodiode”, International Conference on Infrared, Millimeter, and Terahertz Waves (IRMMW-THz), pp. 1-2 (2018).
3. **Ahmad W. Mohammad**, Katarzyna Balakier, Haymen Shams, Frédéric van Dijk, Chin-Pang Liu, Chris Graham, Michele Natrella, Xiaoli Lin, Alwyn J. Seeds, and Cyril C. Renaud, “60 GHz Wireless Link Implementing an Electronic Mixer Driven by a Photonically Integrated Uni-Traveling Carrier Photodiode at the Receiver”, Proc. IEEE Topical Meeting Microw. Photon., pp. 1-4 (2018).

4. Cyril C. Renaud, Katarzyna Balakier, Martyn Fice, Luis Gonzalez Guerrero, **Ahmad W. Mohammad,** James Seddon, and Alwyn J. Seeds, “Integrated Photonic Technologies for THz coherent systems”, Proc. The 7th International Symposium on Terahertz Nanoscience (TeraNano VII), (2016).
5. Cyril C. Renaud, Katarzyna Balakier, Luis Gonzalez Guerrero, James Seddon, **Ahmad W. Mohammad**, Martyn Fice, and Alwyn J. Seeds, “Recent development in integrated photonic solutions for THz systems”, The 19th European Conference on Integrated Optics, pp. 1-2 (2017).

Acknowledgment

First, I would like to express my gratitude to my advisor Prof. Cyril C. Renaud for his unlimited support while working on this PhD thesis. His guidance, motivation and patience were very essential for the completion of this work. Also, I thank Professor John Mitchell for co-supervising this PhD project.

Second, I sincerely thank my colleagues Dr. Haymen Shams and Dr. Katarzyna Balakier for their support in setting up the experiments and their important feedbacks and discussions. Moreover, I express my appreciation to all the member of the ultra-fast photonics group at UCL: Professor Alwyn J. Seeds, the head of the group, Dr. Chin-Pang Liu, Dr. Chris Graham, Dr. Michele Natrella, Dr. Will Yang, Dr. Martyn Fice, Dr. Valeria Vercesi, Dr. Lalitha Ponnampalam, Dr. Rodolfo Hermans, Mr. Luis Gonzalez Guerrero, Mrs. Xiaoli Lin, Mr. James Seddon, and Mrs. Lucy Hale for the valuable ideas and discussions during the group meetings, as well as their reviews of my papers, which significantly improved the quality of my work. Further, I extend my appreciation to my colleagues and friends in the electrical engineering department at UCL for the good times we had throughout the past three years.

Besides, I am grateful for the funding from FiWiN5G Marie Sklodowska-Curie European Union's Horizon 2020 Research and Innovation Programme under Grant 642355, and to my colleagues in FiWiN5G for the great experiences we had during the trainings and the summer and winter schools. In this regard, I specifically thank Dr. Frédéric van Dijk from III-V Labs, the industrial partner of this project, for hosting me at III-V Labs to conduct characterization experiments, and for providing the photonic integrated circuits, which were essential for successful completion of the project.

Also, I thank both of Dr. Eszter Udvary from Budapest University of Technology and Economics (BME) and Dr. Attila Hilt from Nokia – Hungary for hosting me at their organizations for a period of ten weeks to perform my project secondment.

Last but not the least, I would like to thank my parents, family and friends for their spiritual support while working on this project and throughout my life in general.

Thank you all,

Ahmad Wasfi Mahmoud Mohammad

January 2019

List of Abbreviations

4G : fourth generation of mobile systems

5G : the fifth generation of mobile communications systems

ADC : analog to digital convertors

ASE : amplified spontaneous emission

AWG : arbitrary waveform generator

BER : bit error rate

CL : conversion loss

CMA : constant modulus algorithm

CMOS : complementary metal oxide semiconductor

CPW : coplanar waveguides

CR: cognitive radio

D2D: device-to-device

DAC : digital to analog convertors

DFB : distributed feedback

DSP : digital signal processing

EAMs : electro-absorption modulators

ECLs : external cavity lasers

EDFAs : erbium-doped fiber amplifiers

ESA : electrical spectrum analyzer

EVM : error vector magnitude

FD : full duplex

FEC : forward error correction

FET : field effect transistor

FFT : fast Fourier transform

FWM : four-wave mixing

HBT: heterojunction bipolar transistor

HD : high definition

HEB : hot electron bolometer

HEMT : high-electron-mobility transistor

IF : intermediate frequency

IMPATT :impact ionization Avalanche transit-time

IoT: internet of things

ITU : international telecommunications union

LNA : low noise amplifier

LO : local oscillators

LoS : line of sight

LTG-GaAs : low temperature grown GaAs

M2M : machine to machine

MIMO : multiple input and multiple output

MLLD: mode-locked laser diodes

MMI : multimode interference

MMW : millimeter wave

MZM : Mach-Zehnder modulator

NDR: negative differential resistance

NF : noise figure

NOMA : non-orthogonal multiple access

NRZ : non-return to zero

OBPF : optical bandpass filter

OFC : optical frequency comb

OIPLL : optical injecting phase locked loops

OOK : on-off keying

OPLL/OFLL : optical phase/frequency locked loops

OPM : optically pumped mixer

OSA : optical spectrum analyzer

PA : power amplifier

PCs : polarization controllers

PIC : photonic integrated circuit

PRBS : pseudo random bit sequence

QoS : quality of service

QPSK : quadrature phase shift keying

RF : radio frequency

RoF : radio over fibre

RRC : root raised cosine

RTD : resonant tunnelling diodes

RTO : real-time oscilloscope

SBD : Schottky barrier diode

SNR : signal to noise ratio

SOAs : semiconductor optical amplifiers

SIS: superconductor insulator superconductor

TUNNETT : tunnel injection transit time

TW : traveling wave

UEs : user entities

UTC-PD : uni-traveling carrier photodiode

XGM : cross gain modulation

XPM : cross phase modulation

Table of Contents

List of Figures

List of Tables

Chapter 1: Introduction

1.1 Motivation

The global mobile data traffic is predicted to reach 49 Exabyte per month by 2021, which is a 7-fold increase compared to 2016 [5]. Such a high demand will be impossible to meet using the current fourth generation of mobile systems (4G) technologies, especially with the rapid rise of new applications that require very low end-to-end latency in machine to machine (M2M) communications and the internet of things (IoT) [6], which is expected to account for about 29% of connected devices in 2021 [5]. To address these issues and others, the ITU has defined the minimum requirements for 5G in terms of data rate, capacity, latency, quality of service (QoS), energy efficiency and other parameters, as illustrated in Fig. 1-1.

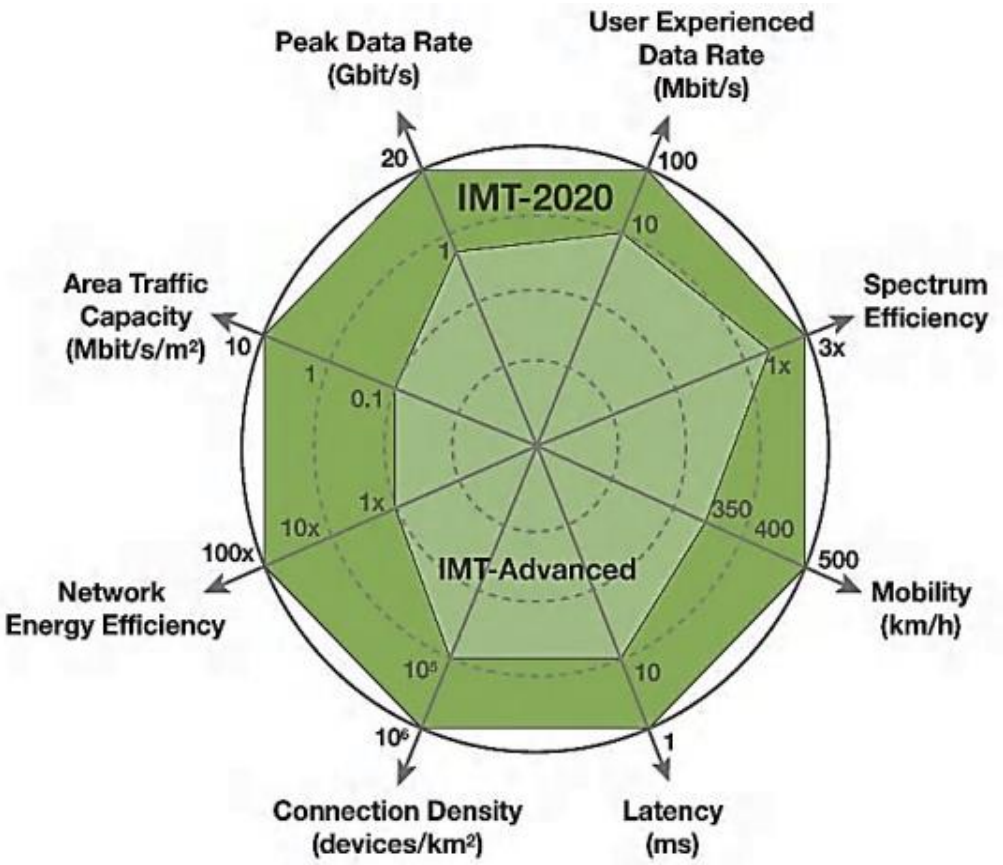

Fig. 1-1: 5G requirements as defined by the ITU (Reprinted with kind permission from ITU) *[7]*.

1.2 Requirements for 5G

The key requirement for 5G can be summarized as follows [8]:

- A peak data rate of at least 20 Gbit/s for the downlink, and 10 Gbit/s for the uplink.
- A user experienced data rate of at least 100 Mbit/s for the downlink, and 50 Mbit/s for the uplink.
- A spectral efficiency of at least 30 bit/s/Hz for the downlink, and 15 bit/s/Hz for the uplink.
- A mobility of up to 500 km/h.
- A latency as low as 1 ms for both the uplink and the downlink.
- A minimum connection density of 10^6 devices per km^2.
- Two orders of magnitude enhancement on the network's energy efficiency compared to IMT-Advanced.
- A total traffic throughput per area of at least 10 Mbit/s/m^2 in the indoor hotspot downlink.
- A reliability requirement of at least ($1-10^{-5}$) success probability of transmission.
- A bandwidth of at least 1 GHz for frequency bands above 6 GHz.

1.3 Candidate Technologies for 5G

For 5G to be able to deliver these requirements it must utilize innovative technologies and adapt new network architectures. Some of the key technologies that have been considered as candidates for 5G include [9] [10]: non-orthogonal multiple access (NOMA) [11], massive multiple input and multiple output (MIMO) [12], network coding [13], full duplex (FD) [14], device-to-device (D2D) communications [15], MMW communications [16], software defined networks [17], cognitive radio (CR) [18], and green communications [19].

1.4 MMW Technology for 5G

5G cannot rely on the current low frequencies (<3 GHz) because they are almost fully occupied by other communication systems, such as mobile, broadcast and satellite services [20]. As a result, researchers have been exploring MMWs because of the abundance of spectrum in the MMW range (30 GHz - 300 GHz) that will allow for high speed communications even at low spectral efficiency. Moreover, at such high frequencies the antenna size becomes smaller, and it becomes practical to develop integrated antenna arrays [21] and enjoy the benefits of massive MIMO, which include increasing the capacity, energy efficiency, and flexibility [22]. Further, the high propagation losses in the MMW range limits the effective communication distance to about 200 m in dense urban environments [23], making it more secure and allows for frequency reuse.

According to the ITU's world radiocommunication conference (WRC), several frequency bands in the MMW range, between 24 GHz and 86 GHz, will be considered for 5G [24]. A list of these bands is provided in Table 1-1. Most of these bands have been already allocated to mobile, while others do not currently have global mobile allocation. Of these bands, the (24 GHz – 40 GHz) bands are expected to be the initial 5G bands above 6 GHz [25].

Table 1-1: A list of frequency bands in the MMW range which are being considered for 5G *[26] [24]*.

Frequency Group	Already Allocated	Not Allocated Yet
Group 30 GHz	• 24.25 – 27.5 GHz.	• 31.8 – 33.4 GHz.
Group 40 GHz	• 37 – 40.5 GHz. • 42.5 – 43.5 GHz.	• 40.5 – 42.5 GHz.
Group 50 GHz	• 45.5 – 47 GHz. • 47.2 – 50.2 GHz. • 50.4 – 52.6 GHz.	• 47 - 47.2 GHz.
Group 70/80 GHz	• 66 – 71 GHz. • 71 – 76 GHz. • 81 – 86 GHz.	

1.5 State-of-the-Art MMW Transceivers

Electronics and photonics are two competing technologies in the field of MMWs generation. For MMW generation, electronic techniques rely on high frequency diode-based sources, or transistor-based sources, or low frequency oscillators followed by frequency multiplication stages [27], while photonic techniques use optical heterodyning on photomixers [28] and laser pulse techniques [29].

As for MMW detection, electronics have proven to be very efficient. For example, electronic mixers based on Schottky barrier diodes (SBD) have conversion losses as low as 5 dB even at 180 GHz [30] compared to 32 dB conversion loss of UTC-PD opto-electronic mixer at 100 GHz [31].

There are some issues with electronic-based MMW generation techniques. For example, frequency multiplication introduces large losses, and this requires an amplification stage after each frequency multiplication stage [32]. This results in a degradation in the phase noise of the generated signal. Similarly, diode-based sources such as resonant tunnelling diodes (RTDs), Gunn diodes, and impact ionization Avalanche transit-time (IMPATT) diodes generally suffer from large phase noise. The presence of high phase noise limits the data rates of communications systems especially in multi-antenna systems [33] and when higher order modulation formats are used [34]. Finally, as will be discussed in the following chapter, transistor-based sources such as complementary metal oxide semiconductor (CMOS) have better phase noise than the other two electronic techniques. However, they do not generate as much power, so, they utilize power combining techniques to increase the power of the generated signal. In addition, as for the other electronic techniques, transistor-based sources have narrow tuning

range, which makes the communication systems less flexible in terms of frequency of operation.

Despite these issues, electronic-based techniques have successfully been demonstrated as MMW transceivers, and their performance have been constantly improving. The following discussion illustrates the evolution of electronic-based transceivers at 60 GHz. In 1996, a 20 Mbit/s transceiver was demonstrated based on monolithic microwave integrated circuit (MMIC) technology at 60 GHz [35]. After that, in 2004, a 3.5 Gbit/s transceiver was demonstrated using the same technology and at the same frequency [36]. Later, in 2005, a 900 Mbit/s integrated transceiver was demonstrated using SiGe bipolar transistor technology [37]. Five years later, a 4 Gbit/s quadrature phase shift keying (QPSK) transceiver was demonstrated using 90 nm CMOS technology [38], followed by an 11 Gbit/s 16-quadrature amplitude modulation (QAM) demonstration using 65 nm CMOS process [39]. In 2015, a SiGe bipolar transistor transceiver demonstrated 2.5 Gbit/s transmission over 20 meters [40]. Finally, in 2017, an ultra-high data rate transceiver was demonstrated using 65 nm CMOS technology with data rates up to 42.24 Gbit/s [41]. This transceiver consumes 544 mW and 432 mW in the transmitter and receiver modes, respectively.

Similar to electronics, photonic MMW-generation techniques have improved in recent years. Table 1-2 below provides a list of the most recent transmission experiments at 60 GHz based on electronic and photonic technologies. For example, in 1998, 155 Mbit/s wireless transmission was demonstrated at 60 GHz by heterodyning two optical tones after propagating in a 12.5 km-long radio over fibre (RoF) link [42]. Later, in 2008, a 12.5 Gbit/s RoF link with on-off keying (OOK) data modulation was demonstrated at 60 GHz [43].

Also, in the same year, a 2.1 Gbit/s wireless transmission link was demonstrated after 50 km of RoF [44]. One year later, a 27 Gbit/s RoF was demonstrated at 60 GHz [45]. In 2015, a photonic integrated UTC-PD-based transmitter of 1 Gbit/s was demonstrated at 90 GHz [46]. Finally, in 2016, a 1.2 Gbit/s RoF link was demonstrated at 60 GHz implementing a PIC for MMW generation [1].

Table 1-2: A summary of the most prominent electronic and photonic based wireless transmission experiments at 60 GHz.

Electronic-based	Photonic-based
• **2011 [39]:** ▪ **65-nm CMOS.** ▪ **16 QAM transceiver.** ▪ **Data rate: 11 Gbps.** ▪ **Wireless distance: 5 cm.** ▪ **BER: < 10^{-3}.** ▪ **phase noise: -95 dBc/Hz @ 1 MHz offset.**	• **2008 [43]:** ▪ **Wireless RoF.** ▪ **OOK transmitter.** ▪ **Data rate: 12.5 Gbps.** ▪ **Wireless distance: 3.1 m.** ▪ **BER: 10^{-9}.** ▪ **Fibre length: 50 m.**
• **2015 [40]:** ▪ **130 nm SiGe BiCMOS.** ▪ **QPSK transceiver.** ▪ **Data rate: 2.5 Gbps.** ▪ **Wireless distance: 20 m.** ▪ **phase noise: -88 dBc/Hz @ 1 MHz offset.**	• **2009 [45]:** ▪ **Wireless RoF transmitter.** ▪ **16 QAM OFDM.** ▪ **Data rate: 27.04 Gbps.** ▪ **Wireless distance: 2.5 m.** ▪ **BER: 4.2*10^{-3}.** ▪ **Fibre length: 10 m.**
• **2017 [41]:** ▪ **65-nm CMOS.** ▪ **64 QAM transceiver.** ▪ **Data rate: 42.24 Gbps.** ▪ **Wireless distance: 3 cm.** ▪ **BER: < 10^{-3}.**	• **2016 [1]:** ▪ **Wireless RoF with PIC.** ▪ **16 QAM OFDM. transmitter.** ▪ **Data rate: 1.2 Gbps.** ▪ **Wireless distance: 4 m.** ▪ **BER: 1.27*10^{-4}.** ▪ **Fibre length: 100 m.**

However, when it comes to MMW detection, photonics has been unfavoured because of the lack of efficient optoelectronic mixers at room temperature. For example, the conversion loss of the UTC-PD optoelectronic mixer has been reported at 32 dB [31].

Despite the low efficiency of the UTC-PD optoelectronic mixer, there are scenarios where it is advantageous to use this photonic technology in Radar and communication systems [47]. In communications, for example, implementing a photonic-based transmitter or photonic-based receiver facilitates the integration with the high-capacity fibre network by employing RoF techniques, which eliminates the need for the heavy, lossy and expensive coaxial cables [48]. The result is a considerable reduction in weight, latency, and signal transport losses, as illustrated in Table 1-3. Also, this allows for the generation of high-purity signals with high data rates, and ensures immunity to electromagnetic interference.

Table 1- 3: A summary of the advantages of replacing coaxial cables with optical fibre cables [49].

Parameter	Optical Fibre Cables	Coaxial Cables
Data Rates	• > 60 Tbps.	• 10 Gbps.
Transport Distance	• > 19 km @10 Gbps.	• 91 m @ 1 Gbps.
Weight	• 6 kg/km.	• 58 kg/km.
Energy Consumed	• 2 W/user.	• > 10 W/user.
EM/RF Interference	• Immune.	• Susceptible.
Security	• Nearly impossible to tap.	• Susceptible to tapping.
Lifecycle	• 30 – 50 years.	• 5 years.

Further, implementing a photonic-based receiver simplifies the access network especially when multiple antenna units used, and simplifies the phased-array antenna systems used for beamforming [47]. The concept is illustrated in Fig. 1-2, where an optical signal originating from a single laser source can be distributed to feed several phased array antenna units, at which, an optical to RF conversion takes place using a photodiode such as the UTC-PD. The relative phase between the distributed signals can be controlled using optical time delay lines. By controlling the relative phase of the RF signals feeding the antennae, a beam can be created in a specific direction.

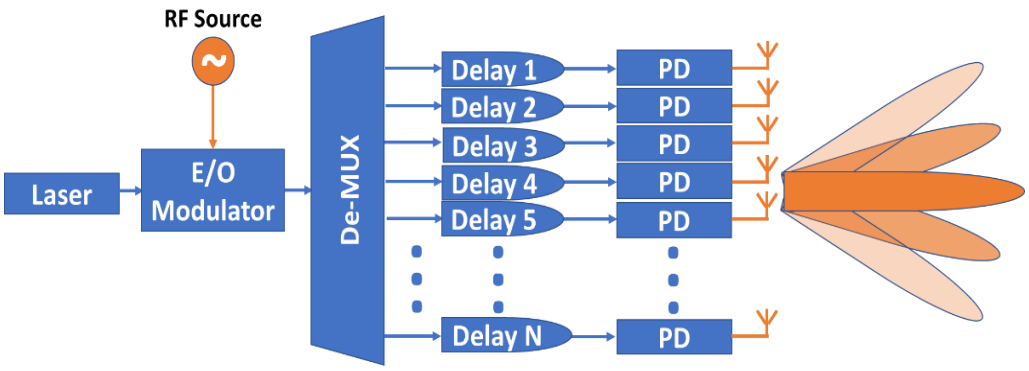

Fig. 1-2: A use case of photonic techniques in beam steering [47].

Also, photonics offers wide tuneability simply by changing the spacing between the optical tones used. This wide tuneability is a desired feature as it offers flexibility on the frequency of operation of the system, and simplifies the architecture of some systems, such as the multicast systems [50]. As shown in Fig. 1-3, with RoF techniques, it is possible to separate the signal generation unit from antenna units, thus, simplifying the antenna units and allowing for reaching remote locations, thanks to the low signal transport losses in fibre.

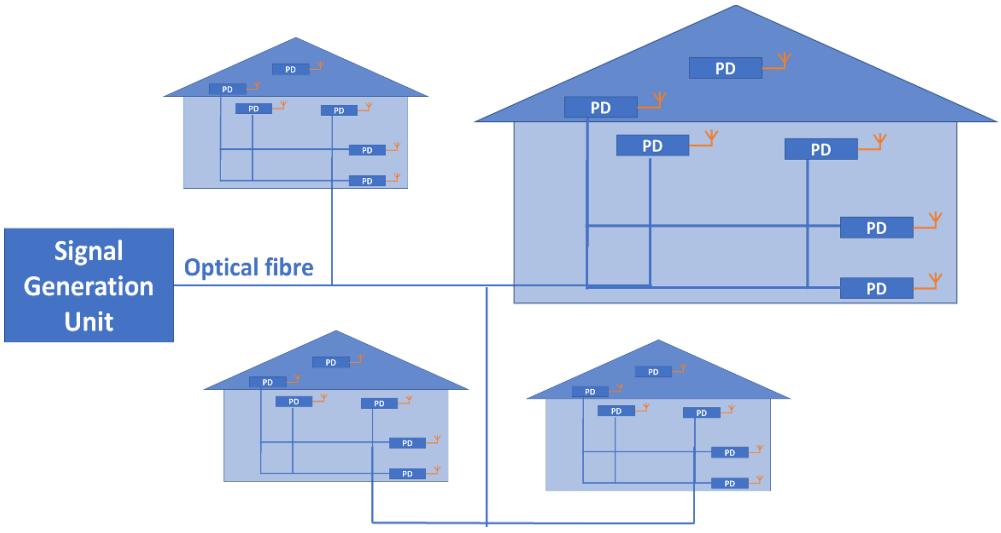

Fig. 1-3: A use case for photonics in multi-cast systems *[47]*.

Considering these advantages of photonics and the great integration potential of UTC-PD, this PhD thesis aimed at demonstrating UTC-PD-based MMW wireless receivers.

In this work, the first demonstration of UTC-PDs in MMW wireless receivers is presented, in Chapter 3, with data rates of 5 Gbps, 2 Gbps QPSK and 1 Gbps at 35.1 GHz, 33.5 GHz, and 60 GHz, respectively, as they belong to the range of interest to 5G, as discussed in Sec. 1.4.

Then, Chapter 4 presents the first demonstration of a photonic integrated transceiver at 60 GHz. As an integrated solution, this transceiver offers reduction in size, weight, and power consumption. However, the cost could be an issue due to the expensive packaging. The transceiver demonstrated here operates at 1 Gbit/s at the uplink and 0.5 Gbit/s in the downlink. The performance of the demonstrated transceiver reported in this thesis is below its counter parts in electronics in terms of the achieved data rates. However, there are scenarios where it can be more advantageous to use a photonic solution, as mentioned earlier in this section.

It is clear from the discussion above that both photonics and electronics have advantages and limitations. This raised a question as to whether it is reasonable to integrate them to benefit from the advantages of the two worlds. For this reason, an experiment implementing a hybrid receiver was conducted at 60 GHz, which is presented in Chapter 5. Results were comparable to those of the photonic integrated receiver, thus, illustrating the viability of this option.

1.6 Thesis Objectives

The objective of this PhD thesis entitled “Integrated photonics for millimetre wave transmitters and receivers” is to demonstrate an MMW photonic integrated transceiver for 5G and future networks. To achieve this target, proof of concept experiments were conducted, first, using non-integrated photonic components at 35.1 GHz and 33.5 GHz. Then, experiments were extended to 60 GHz due to the significance of this frequency band to 5G as it contains 9 GHz of

unlicensed spectrum. Later, a transceiver was demonstrated using a single UTC-PD on a monolithically integrated photonic circuit.

1.7 Thesis Structure

The rest of the thesis is organized as follows. Chapter 2 focuses on MMW technology; its electronic and photonic generation and detection techniques as well as its deployment scenarios and deployment challenges. In Chapter 3, wireless transmission experiments implementing the UTC-PD at the receiver are presented. In these experiments, the UTC-PD is used to receive Gbps data of different modulation formats and at different frequency bands. After that, the results of a photonic integrated transceiver are discussed in Chapter 4. Then, Chapter 5 investigates the feasibility of hybrid receivers. Finally, conclusions and future work are discussed in Chapter 6.

Chapter 2: Millimetre Wave Transceivers

2.1 Introduction

This chapter starts by reviewing the state of the art of MMW generation technologies, which are classified into two categories: electronics-based and photonics-based technologies. Then, it discusses the advantages and the limitations of these technologies. Also, this chapter provides a review of state of the art of MMW receivers and compares them. Finally, the chapter discusses the deployment scenarios and challenges for MMW technology.

Special emphasis is made, in this chapter, on the UTC-PD as a promising photonic technology in 5G transceivers due to its excellent performance in MMW generation, its potential utilization in MMW receivers, and its monolithic integrability with other photonic components.

2.2 MMW Generation with Electronic-based Techniques

Millimetre waves can be generated indirectly using low frequency sources followed by frequency multipliers, or directly from high frequency diode-based or transistor-based sources [27].

2.2.1 Frequency Multiplication

This method implements several stages of frequency multipliers to generate high frequency signals from a low frequency source. Frequency multiplication introduces losses (theoretically: 7.4 dB, typically: 10 dB [51]), so, an amplifier should follow each frequency multiplication stage, which can be complex and costly [27] [32]. In addition, each multiplication stage degrades the noise performance by 6 dB [21] [52].

Nevertheless, the continuous progress in the CMOS technology has facilitated the generation of high-power signals at hundreds of GHz [53]. For instance, Nikpaik et al demonstrated signal generation at 225 GHz (with 5% tuneability) using this method. The oscillator consumed 68 mW of DC power and

generated a 3 dBm RF signal yielding a DC to RF efficiency of 3%, while the phase noise was measured at -94 dBc/Hz at 227 GHz @ 1MHz offset [54].

2.2.2 Diode-based Sources

Diode-based sources like Gunn diodes [55], RTDs [56], IMPATT diodes [57] and tunnel injection transit time (TUNNETT) diodes [58] rely on negative differential resistance (NDR) to generate high frequency oscillations. The difference between these diodes is in the method used to achieve the NDR [27], which results in variations in their performance parameters (oscillation frequency, output power, and phase noise).

IMPATT and Gunn diodes can generate high power tones at high frequencies (20 dBm at 100 – 200 GHz) [27], but their noise performance is poor [32]. TUNNETT diode is a variation of IMPATT diode that can oscillate at higher frequencies with lower noise but with lower output powers [59]. Finally, RTD can generate the highest frequencies among diode-based technologies (up to 1.5 THz) [27] [60]. However, it has the lowest output power among them (below 0 dBm) [27] and the phase noise is high. For example, it's about -64 dBc/Hz at 1MHz in the D-band (110 to 170 GHz) [61].

Fig. 2-1 compares different diode-based sources in terms of their output power and oscillation frequency. Also, Table 2-1 lists examples of diode-based oscillators below 100 GHz with their respective performance parameters.

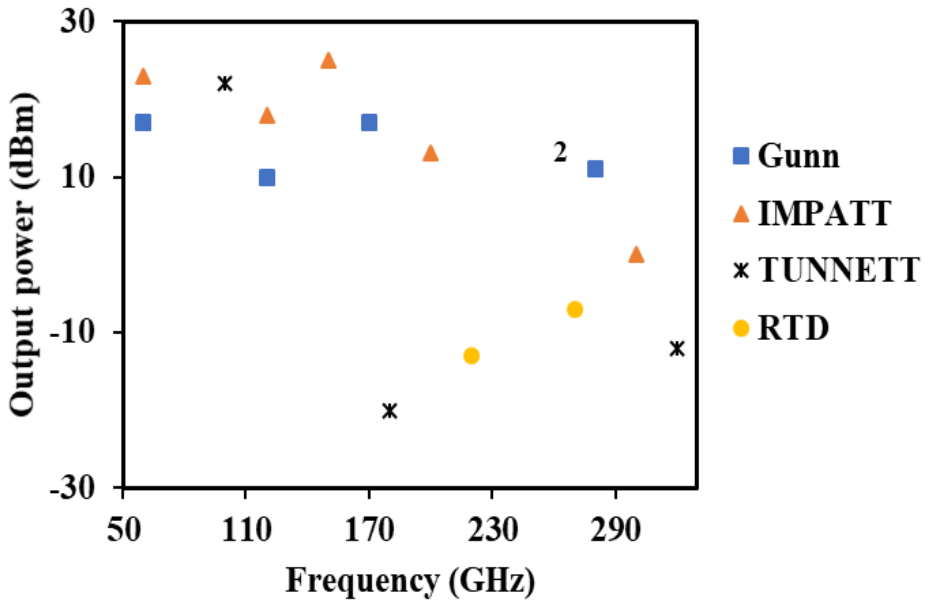

Fig. 2-1: Comparison between different diode-based sources in terms of their output power and frequency of oscillation *[59] [62] [63]*.

Table 2-1: Examples of diode-based sources for MMW generation and their performance parameters.

Technology	Frequency	Output Power	Phase Noise
Gunn [64]	• 78.9 GHz.	• 14 dBm.	• -107 dBc/Hz at 1 MHz offset.
RTD [65]	• 28.7 GHz.	• -0.7 dBm.	• -114 dBc/Hz at 1 MHz offset.
IMPATT [66]	• 82.2 GHz.	• 18.4 dBm.	• Not given.
TUNNETT [67]	• 84 GHz.	• 10 dBm.	• -70 dBc/Hz at 100 kHz offset.

As can be seen in Fig. 2-1 and Table 2-1, the output power of diode-based oscillators is generally high. However, the high phase noise of the signals generated by diode-based oscillators makes them less attractive in high speed communication systems, since this high phase noise limits the maximum data rates that can be transmitted. For example, A. Waheed [34] has shown that for the same signal-to-noise ratio per bit (E_b/N_o), the bit error rate (BER) increases dramatically with modulation format in the presence of high phase noise. For example, at an E_b/N_o = 9 dB, and a phase noise of -90 dBc/Hz, the BER is $3x10^{-5}$, $1x10^{-4}$, and $1x10^{-2}$, for BPSK, QPSK, and 16 QAM systems, respectively.

2.2.3 Transistor-based Sources

While diode-based sources rely on device properties to attain the NDR, transistor-based sources, such as CMOS, heterojunction bipolar transistor (HBT) and high-electron-mobility transistor (HEMT), use circuit level topologies to achieve the NDR, such as LC-cross coupled, Colpitts and ring [27]. Another difference is that transistor-based technologies can provide gain through power amplification, which makes them more attractive than diode-based sources. The output power of transistor-based sources can be enhanced further using power combining techniques [27]. Based on the transistor type and the fabrication material, transistor-based sources can be divided into three major categories:

- III-V-based HBT and HEMT: III-V materials such as InP and GaAs are favoured for high frequencies because of their superior electron transport characteristics compared to silicon [59]. HBT is a bipolar transistor with a larger bandgap for the emitter than the base to give high current gain, while HEMT is a type of field effect transistor (FET) that uses an undoped region to enhance speed and noise performance by reducing scattering [59]. It has been shown that these transistors can operate beyond THz frequencies (InP HBT, 1.1 THz [68]), and (HEMT, 1.5 THz [69]).
- Si CMOS: despite the inferior electron transport characteristics of silicon, the recent advances in silicon fabrication processes allow it to compete with III-V even at high frequencies [59]. Frequencies of up to 400 GHz have been demonstrated with this technology [70].
- SiGe HBT (Bi CMOS): this is a variation of silicon bipolar transistor with some Ge added to the base to reduce the bandgap to enhance speed and

noise performance. Frequencies up to 500 GHz have been achieved with this technology [71].

Fig. 2-2 compares transistor-based technologies in terms of output power versus frequency. The numbers that appear in the figure refer to the frequency harmonic number and the letter 'C' refers to the case where power combining is used.

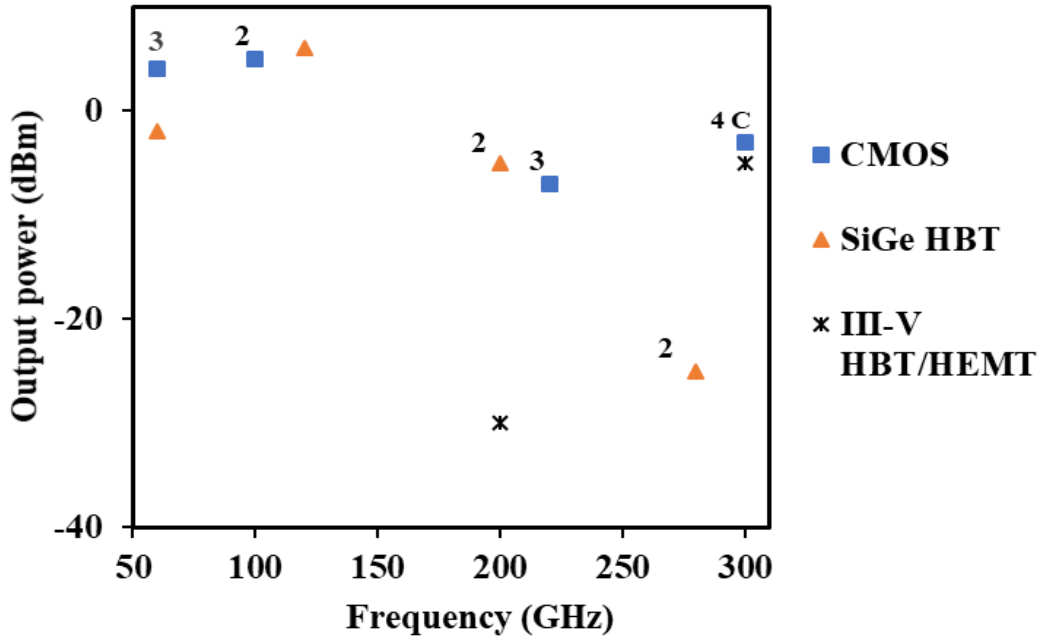

Fig. 2-2: Comparison between transistor-based technologies in terms of output power versus frequency [59] [72] [73].

It is clear from Fig. 2-2 that the power generated with this method is relatively low compared to diode-based oscillators discussed in the previous section. The challenge in generating high power signals at high frequencies in CMOS is due to operating near the unity power gain of the transistor and the high frequency loss mechanisms, such as substrate loss and skin effect [54].

2.3 MMW Generation with Photonic-based Techniques

As discussed in Chapter 1, employing photonic techniques in MMW transceivers can bring numerous advantages to communication systems compared to electronic-based technologies. These advantages can be summarized as follows:

- Using photonic techniques allows for the integration with the fibre network to benefit from the high capacity links, and the reduction in transport losses, weight and energy consumption, as shown earlier in Table 1-3.
- RoF techniques can be used to serve remote locations, and signal generation unit can be separated from antenna units, which simplifies the access network [32], as discussed in Sec. 1-5.
- Also, RoF techniques can be combined with massive MIMO to realize adaptive beamforming, as illustrated earlier in Fig. 1-2.
- Photonics can offer carrier switching, thus, making reconfigurable multi-carrier and agile links feasible, which is a unique feature that has no equivalent electronic solution [74].
- Photonic techniques are superior to electronic techniques in terms of the purity of the generated signal at high RF frequencies. Low phase noise signals can be generated independently of the frequency, and level of the phase noise is determined only by the quality of the laser source [32].
- Photonics allows for wide tuneability in the RF domain [75] by utilizing the concept of optical heterodyning, which is discussed next.
- Unlike electronics, photonics offers high modulation index [74].

The discussion above shows that photonics can offer some attractive features to MMW transmitters. However, the quality of the generated signals with photonic techniques is dependent on the quality of the laser source used. Since silicon is not yet a good light source [76] III-V materials should be used instead, and this increases the costs, as will be shown in the next section. The high cost is attributed to the expensive materials used, like InP, as well as the expensive epitaxial growth steps needed. Further, the multiple regrowth steps limit yield [77].

Several photonic techniques have been considered for MMW generation, including: photomixing (optical heterodyning), direct intensity modulation [78], optical external modulation [79], mode-locked laser diodes (MLLD) [80], nonlinear effects in waveguides and fibres such as four-wave mixing (FWM) [81], cross gain modulation (XGM) [82], cross phase modulation (XPM) [83] and Brillouin fibre laser [84]. Table 2-2 provides a summary of the advantages and disadvantages of using each method.

Table 2-2: Advantages and limitations of photonics-based MMW generation methods.

Technique	Advantage	Limitation
Two free running lasers or dual mode laser	• simple. • full modulation depth [85]. • highly tuneable [75]. • free from dispersion effects [85] .	• high phase noise [75] [86].
Mode locked lasers	• can generate high frequency combs [86]. • low noise [75].	• not tuneable [75]. • large linewidth [86].
Brillouin fibre laser	• low phase noise [87].	• limited in frequency because Brillouin shift is fixed in fibre [87].
Direct modulation	• simple.	• limited frequency [81].
Optical external modulation	• low phase noise [88]. • high conversion efficiency [89].	• require expensive high voltage drivers [88]. • affected by chromatic dispersion in fibre [88].
Nonlinear effects in waveguides	• low phase noise [86].	• require high pump power [86]. • low conversion efficiency [86].
OFCG	• high frequency [75]. • high tuneability [75]. • low noise [75].	• complex.

The heterodyning technique implies injecting two optical tones into a high-speed photodiode (such as UTC-PD) or a photoconductor, to generate an electrical signal with frequency that equals the spacing between the optical tones, as shown in Fig. 2-3.

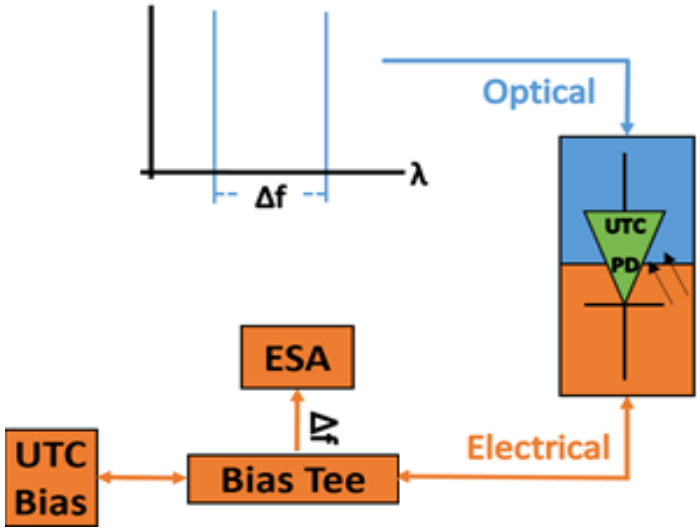

Fig. 2-3: Optical heterodyning in UTC-PD.

The mathematical description of this method is described in [32]. When an electromagnetic wave is injected into a photodiode, the photodiode generates a photocurrent, *i(t)*, that is proportional to the square of the amplitude of the electric field, *E(t)*, of the incident wave, as described by *eq. (2-1)*:

$$i(t) \propto \eta\, E^2(t) \qquad \textit{eq. (2-1)}$$

where η is the responsivity of the photodiode.

When two optical tones, with the same polarization, at frequencies f_1 and f_2 are injected into the photodiode, assuming a lossless propagation medium, their electric field, *E(t)*, can be expressed as:

$$E(t) = A_1 \cos(2\pi f_1 t) + A_2 \cos(2\pi f_2 t + \varphi) \qquad \textit{eq. (2-2)}$$

where A_1 and A_2 are the amplitude of the first signal and the second signal, respectively, and φ is the phase offset between the two signals.

Substituting *E(t)* in *eq. (2-1)*, the following expression is obtained:

$$i(t) \propto \eta \{A_1^2 + A_2^2 + A_1^2 \cos(4\pi f_1 t) + A_2^2 \cos(4\pi f_2 t + 2\varphi) + A_1 A_2 \cos(2\pi(f_1 - f_2)t - \varphi) + A_1 A_2 \cos(2\pi(f_1 + f_2)t + \varphi)\} \quad \text{eq. (2-3)}$$

The terms with frequencies $2f_1$, $2f_2$, and $(f_1 + f_2)$ are in the optical domain, and, therefore, can be ignored, and, so, can the DC term because it is not radiated by the antenna, thus, leaving only the MMW term:

$$i(t) \propto i_o \cos(2\pi f_{RF} t - \varphi) \quad \text{eq. (2-4)}$$

where f_{RF} is the frequency at the difference between f_1 and f_2, while i_o represents the product of the amplitudes and the responsivity.

The simplest way to generate the two optical tones is to use two free running lasers or a dual-mode laser [90]. The heterodyning technique with two free running lasers is attractive because of its simplicity, high tuneability, the fact that it does not require electronic LO, and its robustness against chromatic dispersion, which is important in RoF systems. However, since the two lasers are not locked to each other, the frequency offset between them changes instantly resulting in a high phase noise electrical signal, which can be an issue in communication systems especially those implementing high order modulation techniques.

2.4 Fabrication Materials

It is clear from the discussions in the previous sections that there is a competition between silicon-based and III-V-based MMW generation techniques. This section summarizes the advantages and disadvantages for using each material.

2.4.1 III-V Materials

Among all material systems, the III-V group is the most important because it has a direct bandgap which allows efficient light emission, which is necessary to achieve optical gain [91]. III-V materials such as InP and GaAs are favoured for high frequency applications due to their superior electron transport characteristics compared to silicon which allows for higher frequencies of operation [59]. Also,

III-V materials are superior to silicon in terms of breakdown voltage [74] which allows for high output power (although CMOS can overcome this with power combining techniques with antenna arrays [74] and silicon-based amplifiers, as silicon-based amplifiers are now available at high frequencies: at 200 GHz using Si CMOS, and 245 GHz using SiGe HBT [27]). Finally, III-V materials have higher resistivity than silicon substrate, and this reduces losses of passive devices on the substrate [59].

However, there are issues with using III-V materials. For example, fabrication of III-V components results in nonplanar structures that expose the active region of the device, and this degrades the long-term performance of the device [59]. Also, the thermal conductivity of III-V is lower than silicon (0.68 $WK^{-1}cm^{-1}$ for InP, and 1.45 $WK^{-1}cm^{-1}$ for Si) [92], which makes heat dissipation a problem. Moreover, the defect density is high due to the multiple regrowth steps required [77]. Finally, III-V substrates are smaller and more expensive compared to silicon [59]. For example, the cost of an InP substrate is 4.55 $/cm^2 compared to 0.2 $/cm^2 for silicon, and the size of silicon substrate is more than four times larger than that of InP [93].

2.4.2 Silicon

Silicon could be favoured for commercial applications because silicon-based technologies (Si CMOS or SiGe HBT) give high integration level, excellent reliability, mature design environment, and low cost (for high volume) [27].

However, the operation speed of silicon devices is low due to the inferior electron transport characteristics. Moreover, the intrinsic resistivity of silicon is low ($2.3x10^5$ Ω-cm at room temperature), compared to $1.4x10^8$ Ω-cm in GaAs and $8.6x10^7$ Ω-cm in InP [27]. Such low resistivity in silicon substrate leads to high

ohmic loss and thus degradation of device's performance with electromagnetic field penetrating the substrate due to the leakage currents [94].

2.5 UTC-PD as an MMW Emitter

Photomixing takes place on a photodiode or a photoconductor. Here, we compare three famous photomixing devices: p-i-n photodiode (PIN-PD), UTC-PD and low temperature grown GaAs (LTG-GaAs) photomixer.

Conventional photodiodes have p-i-n structure. In PIN-PD, photo generation takes place in the depletion region that is non-intentionally doped. Both electrons and holes drift contribute to transit time limited 3 dB bandwidth. When depletion region becomes thinner, transit time becomes shorter. However, capacitance becomes a limiting factor.

The problem with conventional PIN-PDs is that even with higher electron velocity, the bandwidth does not increase. This is because holes require longer time. PIN-PDs are bandwidth limited due to the carrier transit time, load resistance and intrinsic and parasitic capacitance [95].

In UTC-PD, absorption and carrier collection are separate processes, allowing for a higher 3-dB bandwidth (a 3-dB bandwidth of 310 GHz has been demonstrated [96]). The band diagram of the UTC-PD is shown in Fig. 2-4. It consists of narrow gap P-type light absorption layer (active layer), a depleted wide gap carrier collection layer and a wide gap P-type layer on the anode to block electron diffusion into the anode.

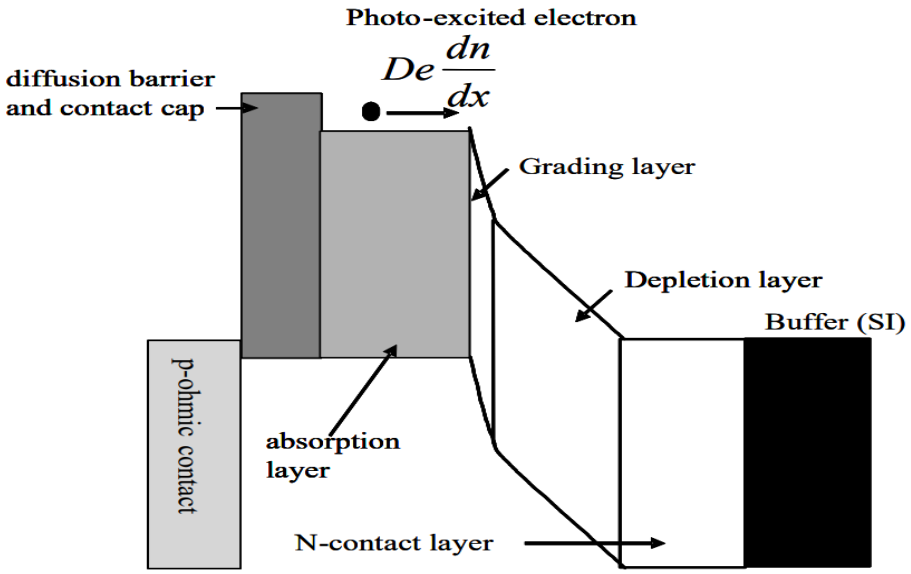

Fig. 2-4: Band diagram of the UTC-PD (Reprinted with kind permission from C. Renaud) [97].

In UTC-PD, absorption takes place in the p-doped region, where holes are the majority carriers. As a result, only electrons drift through the depletion region. This leads to the following advantages: (1) shorter transit time than PIN-PD, (2) overshoot velocity that leads to non-linearities, which can be used in opto-electronic mixing, (3) traveling wave effects, which gives better 3 dB bandwidth and better roll-off frequency response, and this leads to higher level of generated power [98]. Also, UTC-PD has better saturation performance than PIN-PD because holes are not present in the depletion region.

From the previous discussion, it is clear that the UTC-PD has superior capabilities as an MMW emitter in terms of bandwidth and power compared to PIN-PDs. The UTC-PD has higher output power compared to the PIN-PD mostly due to the high saturation current [75].

LT-GaAs photomixers do not generate as much power as the UTC-PD (see Fig. 2-5 for a comparison). Further, they are optimized to work at 800 nm, which makes them less attractive for communications since lasers and optical components are more available at 1550 nm.

Consequently, researchers have been trying to design InGaAs-based photoconductors and achieved some promising results [99]. However, they are still less efficient than the GaAs photoconductors, and their design process is very difficult due to partially conflicting requirements, such as the high absorption, high resistance, short carrier lifetime, high mobility, and large breakdown field strength [100]. For example, they require adding doping materials such as ErAs to create efficient trap sites. This improves photocarrier mobility, but it creates unwanted free carrier concentrations and lowers the absorption coefficient [99].

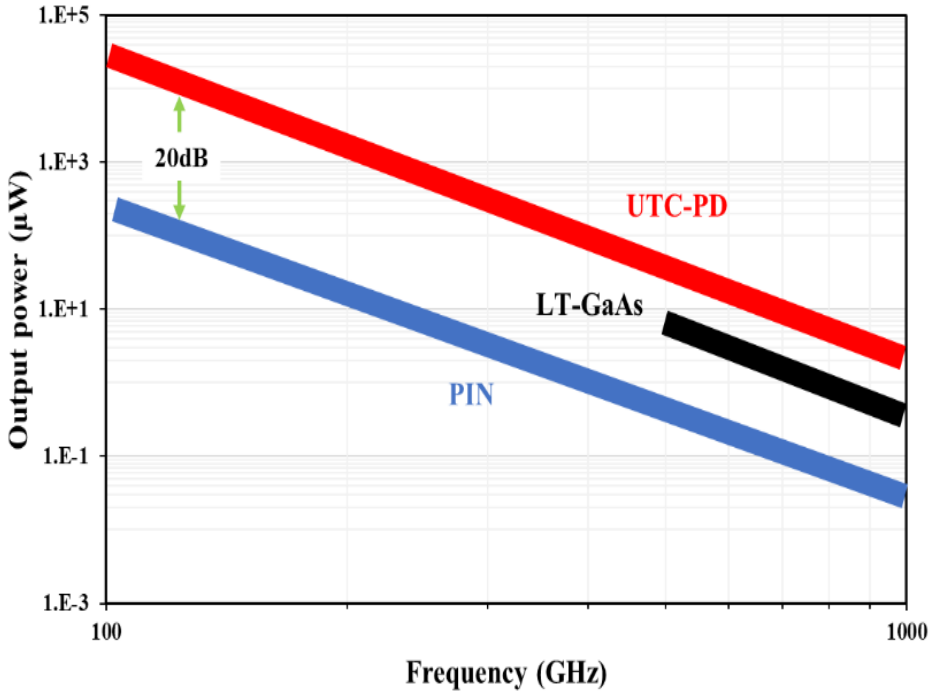

Fig. 2-5: Comparing different photomixing technologies in terms of output power [75].

The best results are obtained when a UTC is combined with a pseudo traveling wave (TW) design with quasi-matched optical and electrical velocities. With a TW design, the device length can be made longer without sacrificing bandwidth. For example, Rouvalis et al. compared three different structures in terms of their 3-dB bandwidth [95]; they show the superior bandwidth of the UTC-PD when combined with traveling wave design: TW-UTC-PD (103 GHz), TW-PIN-PD (83 GHz) and UTC-PD (74 GHz).

Here, it is worth mentioning that the UTC-PD can be monolithically integrated with other photonic components. Fig. 2-6 shows a PIC that comprises lasers, optical amplifiers, modulators and UTC-PDs. The PIC was successfully demonstrated as a 1 Gbit/s transmitter at 100 GHz [46].

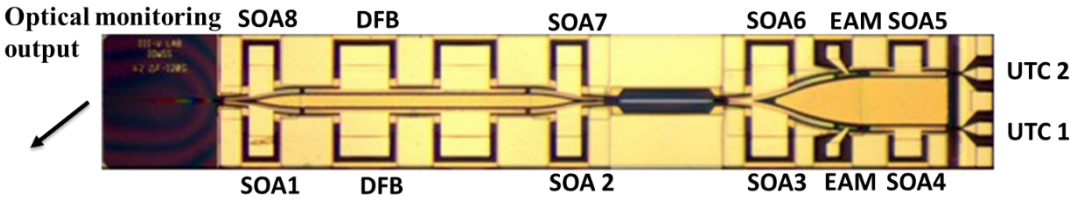

Fig. 2-6: Picture of the photonic integrated circuit [46].

To conclude this section, a comparison is provided in Fig. 2-7 between the UTC-PD and the electronic-based MMW generation technologies discussed earlier. Again, the UTC-PD shows huge potential in the millimetre range in terms of emitted power and bandwidth.

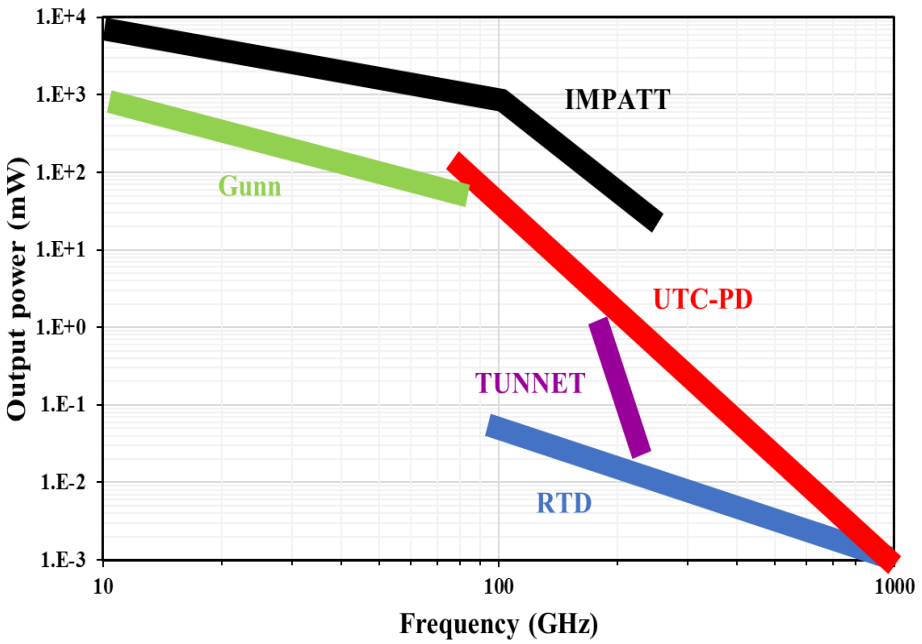

Fig. 2-7: Comparing UTC-PD with electronic-based technologies in terms of output power [29].

2.6 MMW Receivers

A millimetre wave receiver is typically composed of an antenna to detect the radiation, a low noise preamplifier to boost the signal power and increase the receiver sensitivity, and, finally, an MMW detector.

There are two common approaches for detecting modulated MMWs: direct detection (Fig. 2-8-a), and heterodyne detection (Fig. 2-8-b). Heterodyne detection implies mixing the received signal with an LO to down-convert it to a low intermediate frequency (IF).

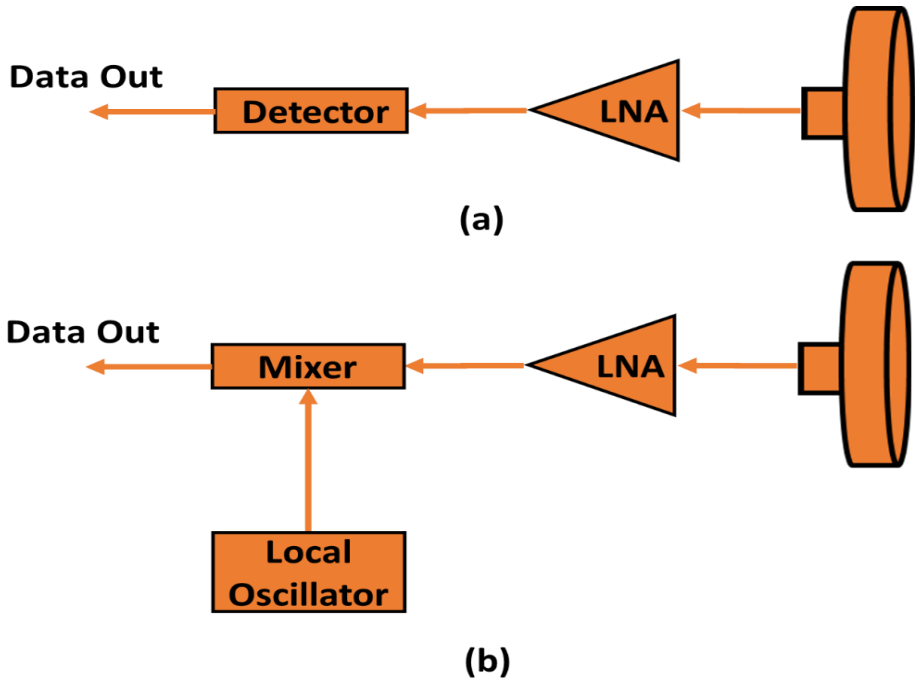

Fig. 2-8: MMWs detection approaches [101].

Mixers are nonlinear circuits that perform frequency translation of an incoming RF signal to another frequency by mixing the RF signal with another signal (LO) [102]. Ideally, the mixer performs a multiplication process of the two signals, as illustrated in Fig. 2-9, and in the following mathematical trigonometry:

$$\cos(2\pi f_{RF}t) * \cos(2\pi f_{LO}t) = 1/2\{\cos(2\pi(f_{RF}+f_{LO})t) + \cos(2\pi(f_{RF}-f_{LO})t)\} \quad \text{eq. (2-5)}$$

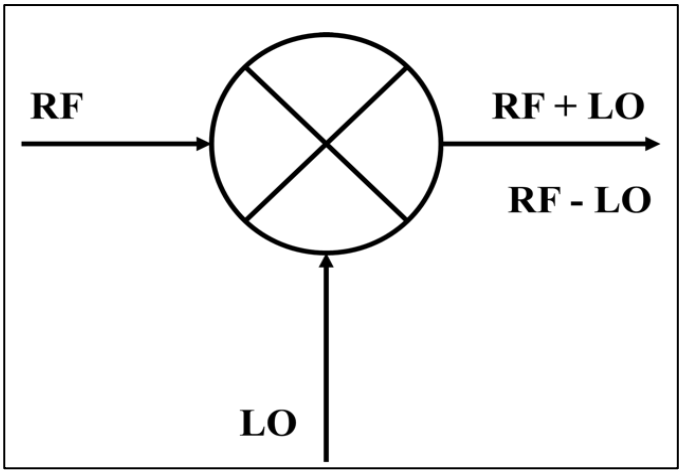

Fig. 2-9: Frequency translation in mixers.

Mixers in the MMW receivers are used to down-convert an incoming high-frequency signal into a low IF for processing. Superconductor insulator superconductor (SIS), hot electron bolometer (HEB) and Schottky barrier diode (SBD) mixers typically use this method [27]. In addition, LTG-GaAs photomixers are known for their mixing capabilities [103]. Advantages and limitations of these mixers are discussed as follows:

- SIS mixer is made of an insulator that is sandwiched between two superconducting layers, typically Nb, NbN or NbTiN, and thus, typically, requires cooling to low temperatures. It is capable of down-converting high frequency signals (up to 1.4 THz [104]) without needing high LO power (only few micro watts). It is widely used in astronomy because of its very low noise level (10K @ 100 GHz).
- HEB is made of a superconducting bridge that connects two metal pads. It has been demonstrated to work at very high frequencies (up to 5.3 THz [105]) but it typically requires cooling to low temperatures. It works by turning radiation into heat, which is translated into a change in resistance that can be detected. It can be used for direct detection or heterodyne detection if an LO is added [59].

- SBD is a metal-semiconductor diode that can be used for direct or heterodyne detection [27] of millimetre and terahertz waves, up to 4.6 THz [106]. Usually, GaAs is chosen as the semiconductor material to allow for high frequency of operation, but silicon is also used when compatibility with CMOS is desired [59] [88] [107]. SBD operates at room temperature and this makes it very attractive for commercial products, although this results in inferior noise performance compared to SIS and HEB (noise temperatures of about 1000 K has been reported with SBD at room temperature at 600 GHz [20] [108]).

Fig. 2-10 gives a comparison between the three detectors described above in terms of their noise performance. SIS and HEB mixers are very sensitive, but they are incompatible with the conventional semiconductor technologies and do not work at room temperature [27]. On the other hand, SBDs work at room temperature, but they are less sensitive than SIS and HEB mixer. Nevertheless, electronic-based technologies proved to be efficient at the receiver [74].

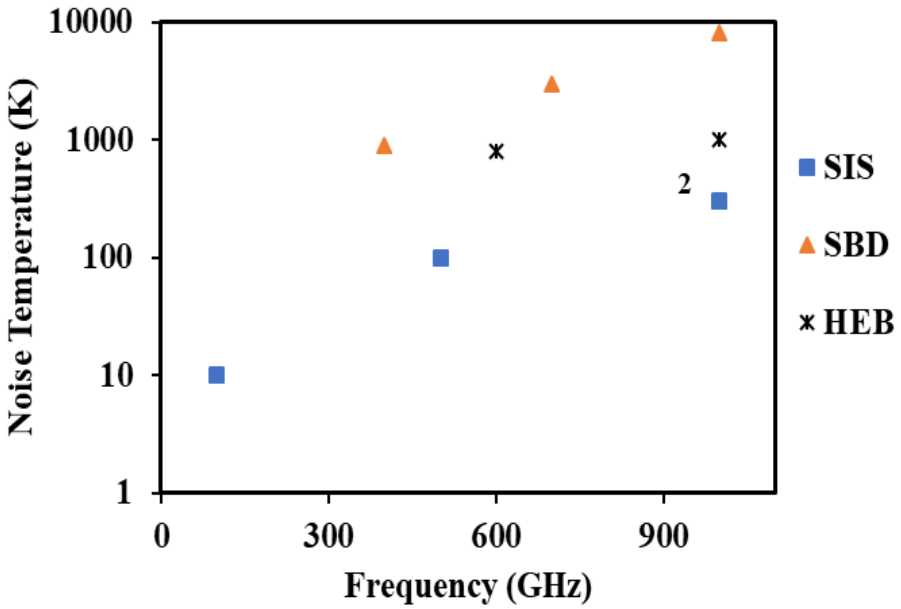

Fig. 2-10: Comparison between different diode-based mixers as detectors [59].

As for the LTG-GaAs, this mixer does not work efficiently at 1550 nm, and typically works at 850 nm or shorter wavelength [109], making it less attractive since components and technologies used in optical communications are more available at 1300 nm and 1550 nm.

Recently, the UTC-PD has been demonstrated as an optically pumped mixer. Compared to the mixers mentioned earlier, a UTC-PD mixer exhibits several attractive features that makes it an attractive alternative if successfully demonstrated in receivers. These features can be summarized as follows:

- The UTC-PD can operate at high frequencies (up to 600 GHz has been demonstrated [110]).
- It has a wide frequency tuning range (tuning from 90 GHz to 580 GHz has been demonstrated [110]). Tuning is realized simply by adjusting the spacing between the optical LO tones. Unlike electronic LOs, optical LOs offer wide tuneability in the RF domain (100's of GHz), with a phase noise that is independent of the frequency.
- The UTC-PD can be monolithically integrated with lasers and modulators on InP substrates [112].
- Contrary to SIS and HEB mixers, the UTC-PD works at room temperature.
- Contrary to Schottky diode mixers, a UTC-PD mixer does not require an electronically generated LO as it can be generated by the UTC-PD itself through the heterodyning of two optical signals [31]. This fact could be exploited in cellular communication systems by using a single optical LO generation unit to serve multiple base stations. The conventional and the proposed concepts are compared in Fig. 2-11-a and Fig. 2-11-b, respectively.

As shown in Fig. 2-11-b, the new concept would reduce installation costs and simplify the network architecture, by eliminating the need for electronic LOs at each base station, and by avoiding the electrical to optical conversion stages at each station that otherwise would be required due to the large transport losses in coaxial cables. Moreover, this would increase the data rates that can be handled per base station due to the large bandwidth of fibre cables compared to coaxial cables. Further, it offers flexibility on the frequency of operation by tuning the spacing between the optical tones. This tuning could be achieved automatically in a software defined network to optimize the network performance.

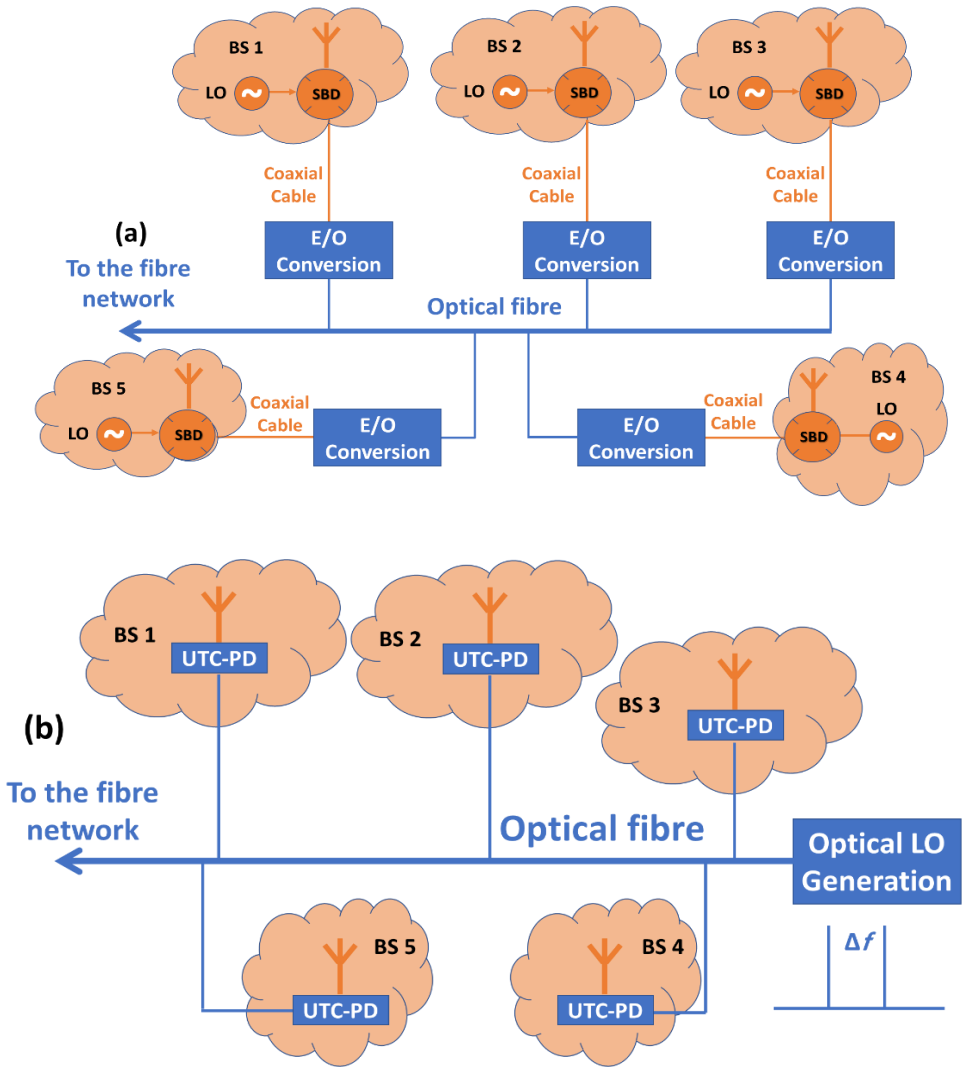

Fig. 2-11: A comparison between cellular communication systems implementing (a) SBD mixer and (b) UTC-PD mixer.

However, as will be seen in the next chapters, there is a major limitation to implementing a UTC-PD opto-electronic mixer at the receiver, which is the high conversion loss. For example, in Chapter 4, conversion losses as high as 28 dB at 60 GHz have been measured on a photonic integrated UTC-PD. This is considered very high compared to Schottky mixers (Schottky mixers with 6 dB of conversion loss between 40 GHz and 60 GHz are commercially available [113]).

From the discussions above, it is clear that each type of the mixers mentioned in this section has advantages and limitations. Table 2-3 provides a summary of these advantages and limitations.

Table 2- 3: Summary of the advantages and disadvantages of different types of mixers.

Technology	Advantages	Limitations
UTC-PD Mixer	• high operating frequency. • wide tuneability. • no electronic LO required. • monolithic integrability of photonic components. • works at room temperature.	• low conversion efficiency.
SIS Mixer	• high operating frequency. • wide tuneability. • no electronic LO required. • very sensitive.	• requires cooling down. • cannot be integrated monolithically with photonic components.
HEB Mixer	• high operating frequency. • wide tuneability. • no LO required. • very sensitive.	• requires cooling down. • cannot be integrated monolithically with photonic components.
SBD Mixer	• high operating frequency. • low conversion loss. • works at room temperature.	• electronic LO is required.
LTG-GaAs Mixer	• no electronic LO required.	• does not work efficiently at 1500 nm.

Given the superiority of the UTC-PD as a MMW emitter, and superiority of electronic receivers, it would seem reasonable to try the hybrid integration of the two technologies in MMW receivers, which is the topic of the next section.

2.7 Hybrid-Integrated MMW Receivers

Integration is essential for size, weight, cost and power consumption reduction [114]. Silicon integration of electronic components has been going on for a long time [115], and it is now a mature technology. But the high losses in silicon limit data rates and signal transport distance with this technology. On the other hand, electronics make excellent receivers.

Microwave photonics provide an excellent solution to this problem by using optical fibre for signal distribution where propagation losses are very low, and offer high capacity and wide tuneability. There have been successful demonstrations of monolithic integration of photonic components using III-V materials [46] because, unlike silicon, they can provide optical gain. However, the cost of photonic integration is high and their performance as receivers is poor.

The operation of MMW wireless receivers could be optimized by the hybrid integration of electronic and photonic components on a single chip. With this approach, electronics provides high sensitivity mixers, while photonics provide widely tuneable LO to drive the electronic part.

This hybrid approach is very appealing because it combines the advantages of electronics and photonics. But integrating the two is challenging due to the different properties of the materials used. For instance, the thermal conductivity of InP is lower than silicon, and this would result in a thermal expansion mismatch [77]. Also, the lower yield of InP will affect that of the entire package [77]. On the other hand, the expected reduction in cost [116] and power consumption [117] and the successful demonstrations of hybrid integration [118] give a big hope to this approach.

Chapter 5 investigates the feasibility of photonic-electronic hybrid integration in MMW wireless receivers by presenting a transmission experiment that implements an electronic mixer driven by a PIC.

2.8 MMW Deployment Scenarios

A few potential deployment scenarios exist for MMW technology [119], including: D2D communications [120], heterogeneous networks [121], and small-cell backhaul [122], which are discussed in the following:

- D2D: in device to device communication, nearby devices communicate with each other without the need for an intermediate hop such as an access point or a base station [123]. This increases spectral efficiency since devices share the same resources. In addition, this helps extending networks coverage by relaying [124]. Further, it helps operators offload traffic from the core network, thus, reducing energy and cost per bit [125]. The performance target for D2D communications is a data rate of 1 Gbit/s and (10 – 1000) meters of transmission distance [126]. In conventional cellular systems, D2D communications would be a very challenging task since interference from the high-power base station as well as from user entities (UEs) is a big issue. Using MMWs would overcome the interference issues thanks to the high directivity beams generated by the beamforming techniques [119].
- Heterogeneous networks: heterogeneous networks contain various types of base stations, including: high power macro cells that cover large geographical areas, and smaller pico and femto cells, which are used to assist the macro cells in capacity and coverage [127]. The main challenges in this architecture is the interference between the macro cells and the

smaller cells, as well as the handover between small cells in high mobility areas [121]. One of the proposed solutions to this problem is to use the concept of phantom cells [128] by which the control and data planes are separated such that high-power macro cells use traditional reliable low frequencies for signalling information, while smaller cells use the MMWs for data communication.

- Small-cell backhaul: The concept is to connect tens of high capacity small-cells, which are distributed in an area of few kilometres, to the core network with sub-millisecond latency [129]. This could be achieved with optical fibre, but it would be expensive to implement. Alternatively, MMWs could offer wireless backhauling to avoid the high costs of new fibres deployment.

2.9 MMW Deployment Challenges

Although MMW technology offers several advantages, there are several issues that need to be addressed before their deployment in 5G networks, including:

- Hardware implementation: it is challenging to develop low-power consumption components at such high frequencies, such as high power amplifiers, analog to digital convertors (ADC) and digital to analog convertors (DAC). For example, the power consumption for the ADC generally scales linearly with the sampling rate and exponentially with the sample resolution [130].
- Adaptive beamforming algorithms: when combined with massive MIMO to obtain more directivity, MMW becomes more sensitive to alignment. So, it is essential to develop low complexity algorithms for adaptive beamforming [124].

- High propagation losses: in MMW communications, most of the energy loss takes place in free space [130]. As shown in Fig. 2-12, MMW signal attenuation is attributed to three factors: free space path loss, gas and rain. Gaseous losses due to oxygen and water vapour absorption take place only at certain frequencies, and signal scattering due to rain is dependent on the heaviness of the rain. For instance, in the case of heavy rain (25 mm/h), the rain attenuation is about 10 dB/km at 73 GHz [119]. The solution is to reduce the cell size. For instance, rain attenuation becomes insignificant (2 dB/km at 73 GHz) in 200 meter-radius cells.

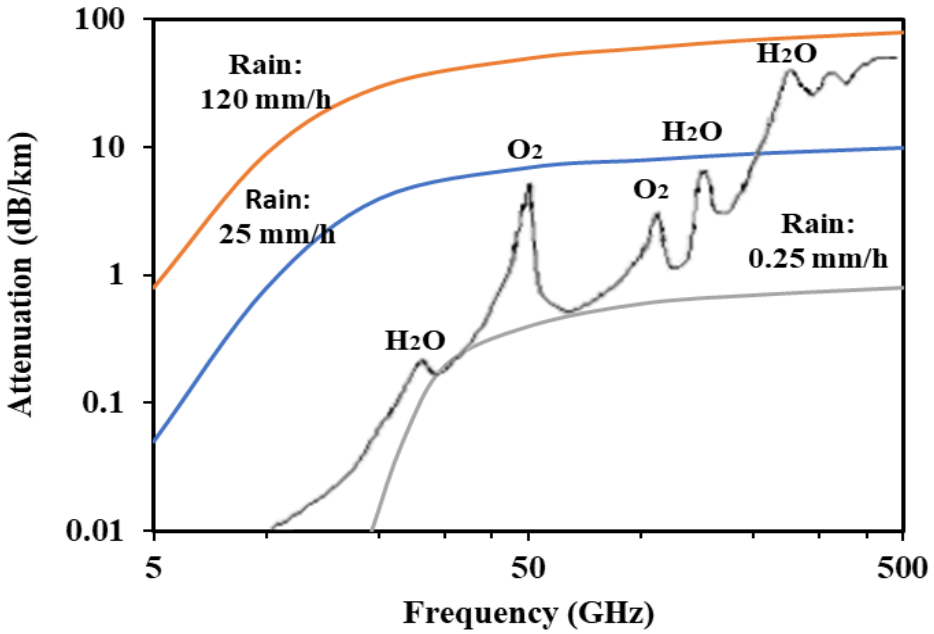

Fig. 2-12: MMW signal attenuation due atmospheric gases and rain [131].

- Blockage effect in MMWs: one of the characteristics of MMWs is that they do not penetrate most solid objects well, especially building materials, such as concrete (attenuation: 175 dB per 10 cm at 40 GHz) [132]. This has two implications: First, indoor environment cannot be served from an outdoor base station and that a different solution needs to be provided for indoor communications, like femto cells or millimetre WiFi [132]. Second, the communication link will be blocked if an object appears in the line of sight.

There are several proposed solutions to the blockage problem. One, is to switch to non-line of sight connection using adaptive beamforming with reflections, but this will attenuate the signal severely. Another solution is to establish indirect connections using relays that have a line of sight (LoS) connection with the receiver [119]. A third solution is to use distributed antenna system (DAS), where antennas are spatially distributed to cover a certain area [130].

2.10 Conclusion

This chapter reviewed three potential technologies for MMW communications: electronics, photonics, and the hybrid integration of the two, and discussed their advantages and their limitations. On the one hand, electronics offer several methods for generating MMWs, including: diode-based sources, transistor-based sources, and frequency multipliers. Also, electronics make high sensitivity MMW receivers. However, electronics cannot transport high data rates signals over long distances, and electronic oscillators are generally not tuneable. On the other hand, photonic technologies can transport high-speed signals over long distances, and can generate widely tuneable signals by using optical heterodyning on high-speed photodiodes such as the UTC-PD. However, photonics performance is less attractive at the receivers due to the high conversion loss of the UTC-PD when used as an opto-electronic mixer.

Consequently, another alternative was considered, which is the hybrid integration of electronics and photonics. This solution promises to combine the benefits of both technologies and to mitigate their limitations. However, there are issues with this approach due to the different materials and processes used in

fabrication. A summary of the advantages and limitations of these approaches is provided in Table 2-4.

Table 2-4: Summary of the advantages and limitations of different MMW integrated technologies.

Technology	Advantages	Limitations
Electronics	• cheap: silicon substrates are large and cheap. • efficient receivers: Schottky-based mixers have low conversion loss. • mature and reliable technology.	• high signal transport attenuation. • low bandwidth and capacity. • narrow tuning range.
Photonics	• easy integration with the fibre network. • supports high data rates. • low signal transport losses • low latency. • ultra-wide tuneability. • simple access network.	• expensive: InP substrates are expensive and small. • III-V processes have high defect density. • photonics performance is poor at the receiver.
Hybrid	• cheaper than monolithic III-V integration. • easy integration with the fibre networks. • supports high data rates. • wide tuneability. • make high-sensitivity receivers.	• challenging due to the different properties of the materials. • low-yield InP affects the entire package.

Also, discussed in this chapter, is the potential deployment scenarios of MMW technology in 5G networks, including: device-to-device communications, heterogenous networks, and small-cell backhaul.

Finally, the expected challenges to MMW technology implementation in 5G were presented, including: the hardware implementation, the adaptive beamforming, the high propagation losses, and the blockage effects. Also, suggestions were provided to overcome these challenges.

The aim of this research is to demonstrate UTC-PD-based MMW wireless receivers, followed by a demonstration of a photonic integrated transceiver. The

next chapter presents successful experimental demonstrations of UTC-PD-based MMW wireless receivers at different frequencies and with different modulation formats. The significance of these demonstrations is showing the feasibility of photonic integrated receivers, which paves the way for photonic integrated transceivers, as will be shown in Chapter 4. Finally, the hybrid solution is studied, as will be seen in Chapter 5.

Chapter 3: UTC-PD-based Wireless Receivers

3.1 Introduction

Mixers are needed in wireless receivers to down-convert high frequency signals to a lower IF to allow for electronic processing before final down-conversion to the baseband, as explained in the previous chapter. The previous chapter presented some commonly used mixers in MMW wireless receivers and discussed their limitations. Also, it discussed the potential advantages that a UTC-PD mixer could offer. In this chapter, the mixing mechanism in UTC-PD is explained, and its successful utilization in wireless receivers is presented.

Previously, it has been shown that a UTC-PD can be used as an optically pumped mixer (OPM) at frequencies up to 600 GHz [110], but these demonstrations were done within a 100 Hz bandwidth [31] [133] which is not enough for communication purposes. The following sections present, for the first time, several-GHz wide mixers based on the UTC-PD and their successful implementation in MMW wireless receivers.

The first demonstration is the wireless transmission of 5 Gbps OOK data at 35.1 GHz with successful data recovery in real-time. However, this comes at the expense of added complexity to the receiver, as it required locking the optical tones of the receiver UTC-PD. The second experiment is wireless transmission of 1 Gbaud QPSK data at 33.5 GHz. It utilized free-running lasers to illuminate the receiver UTC-PD, which proves that a UTC-PD-based receiver can recover complex data signals while keeping the setup simple. Finally, an experiment implementing UTC-PDs at the transmitter and the receiver was successfully conducted at 60 GHz with 1 Gbps OOK data. No high order modulations, like: 16 QAM, are reported here because of their higher sensitivity to phase noise and signal to noise ratio (SNR), as explained in the previous chapter.

These demonstrations contribute to research towards 5G as they were done at carrier frequencies of 35.1 GHz, 33.5 GHz, and 60 GHz, respectively, which belong to the frequency range of interest to 5G, as discussed in Chapter 1. Further, these demonstrations pave the way for the first photonic integrated transceiver which offers a low-cost, high data rate and energy efficient solution.

3.2 5 Gbps Wireless Link with an Optically Pumped UTC-PD Mixer at the Receiver

This section reports the first demonstration of a UTC-PD as a 5 Gbps wireless receiver. In this experiment, a 35.1 GHz carrier was electrically modulated with 5 Gbps non-return to zero on-off keying (NRZ – OOK) data and transmitted over a wireless distance of 1.3 m. At the receiver, a UTC-PD was used as an OPM to down-convert the received radio frequency (RF) signal to an IF of 11.7 GHz, before it was down-converted to the baseband using an electronic mixer. The recovered data show a clear eye diagram, and a bit error rate (BER) of less than 10^{-8} was measured. The conversion loss of the UTC-PD optoelectronic mixer has been measured at 22 dB. The frequency of the LO used for the UTC-PD is defined by the frequency spacing between the two optical tones, which can be broadly tuneable enabling the frequency agility of this photodiode-based receiver.

3.2.1 UTC-PD Optoelectronic Mixer Characterization

The UTC-PD used in this work has dimensions of 7x15 μm^2, and has coplanar waveguides (CPW) with epitaxy structure similar to that described in [135]. It was characterized in terms of its photocurrent versus the bias voltage for different levels of injected optical power (14 dBm, 16 dBm, and 18 dBm), as shown in Fig. 3-1. Also, shown in the same figure is the I-V characterization of a 2x25 μm^2 device by E. Rouvalis [31] for comparison purposes.

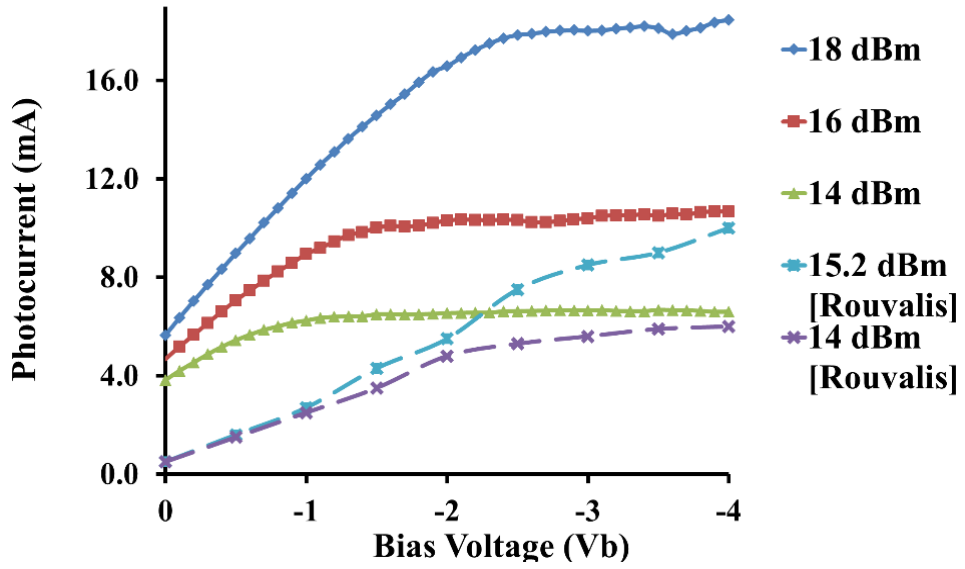

Fig. 3-1: I-V characteristic curve of the UTC-PD in this work in comparison with [31].

In both sets of measurements, the figure shows a trend of increasing photocurrent with increasing optical power and reverse bias voltage. However, the increasing behaviour and the values of the photocurrents for the two devices do not match because of their different epitaxial structures and dimensions.

The UTC-PD was illuminated by an optical signal generated from an external cavity laser (ECL), which was followed by an erbium-doped fibre amplifier (EDFA) to provide optical amplification. The signal was injected into the UTC-PD using a lensed fibre, and the maximum optical power measured at the input of the lensed fibre was 18 dBm limited by the maximum output power deliverable by the EDFA. As expected, the generated photocurrent increased with increasing optical power and bias voltage, and the maximum photocurrent (18.5 mA) was measured at the maximum bias voltage (-4 V) and at the maximum optical power (18 dBm, 63 mW), which gives a responsivity of 0.29 A/W. This is a slightly higher value of responsivity compared to devices of similar structure presented in [136], which report a value of 0.2 A/W. This is because smaller devices, 4x15 μm^2, were used in [136], compared to 7x15 μm^2 devices used in this work.

The frequency response of the UTC-PD was characterized using the heterodyne system depicted in Fig. 3-2, where two optical signals from free running lasers spaced by ΔF were injected into the UTC-PD, via the same lensed fibre, to generate the electrical heterodyne signal at ΔF as mathematically described in [32], while a bias tee was used to couple the voltage bias to a CPW probe that is connected to the waveguides of the UTC-PD.

At −4 V voltage bias and 18 dBm optical power, the frequency response measurements gave a 3-dB bandwidth of approximately 33 GHz, and the emitted power at this frequency was 3 dBm, as shown in Fig. 3-3. The 3-dB bandwidth was approximated by plotting a polynomial trend line of the sixth order.

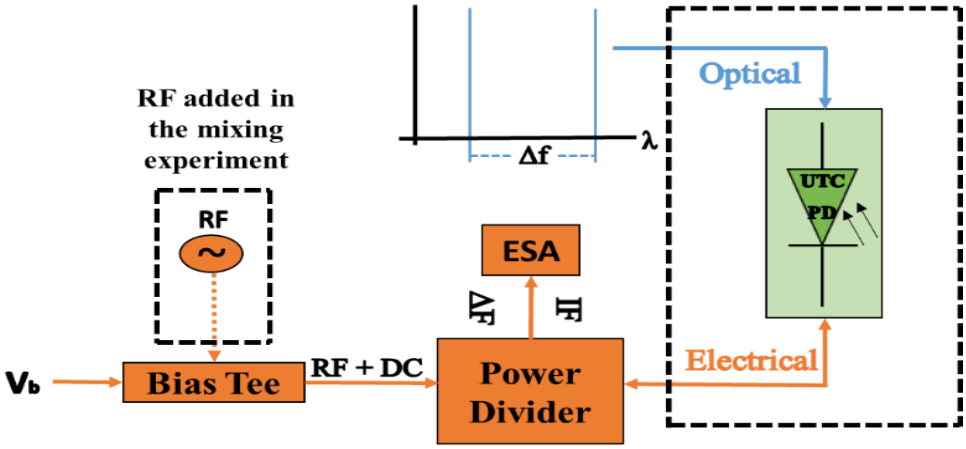

Fig. 3-2: Setup for optical heterodyning (without RF) and optoelectronic mixing (with RF) in UTC-PD.

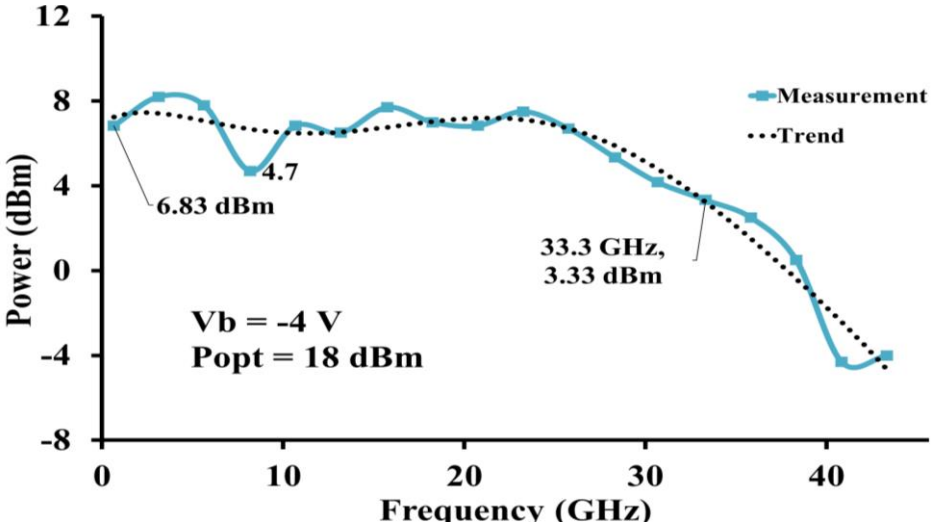

Fig. 3-3: The bandwidth measurement of the UTC-PD.

Using the same experimental system with optical tones spaced by ΔF = 9.7 GHz at −4 V bias and 18 dBm optical power, it was observed that the UTC-PD generates higher order harmonics of the heterodyne signal at ΔF. Signals at 9.7 GHz, 19.4 GHz, 29.1 GHz and 38.8 GHz are clearly observed in the spectrum in Fig. 3-4, corresponding to ΔF, 2ΔF, 3ΔF, 4ΔF, respectively. This indicates a strong enough nonlinear behaviour for mixing purposes. This nonlinear behavior could be explained by the dynamic capacitance associated with the charge storage in the absorption layer of the UTC-PD [137].

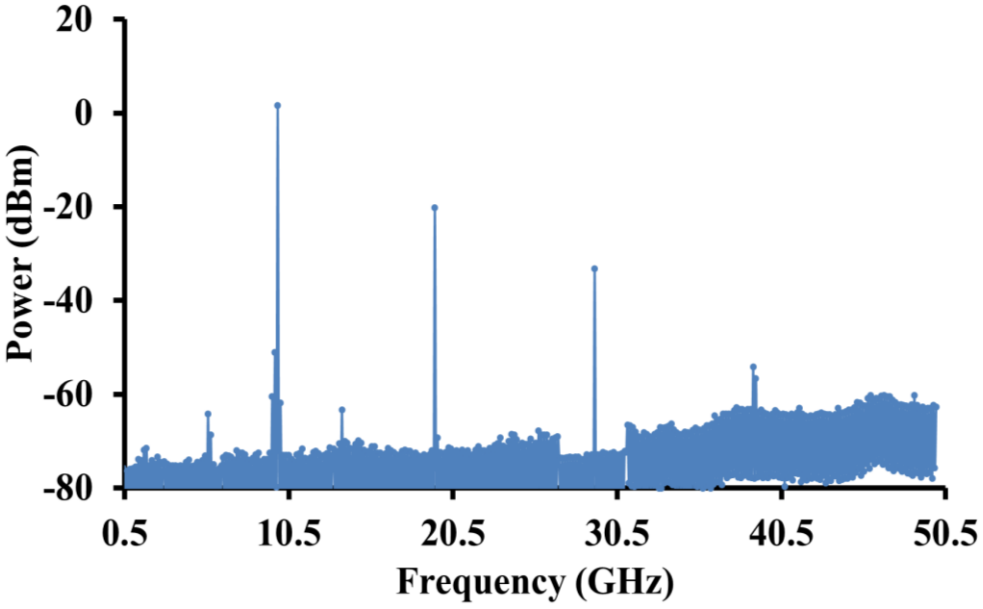

Fig. 3-4: UTC-PD's heterodyne and higher order harmonics at 18 dBm optical power and −4 V bias (RBW = 300 kHz, VBW = 30 kHz).

Mixing in UTC-PD can be exploited in receivers by down-converting an incoming RF signal to a lower IF, as illustrated in Fig. 3-2. In the following mixing experiment, an RF of 35.1 GHz and an optical LO of 23.4 GHz were applied. Consequently, a mixing product was generated at an IF of 11.7 GHz, that is equal to the difference between the incoming RF signal and the heterodyne signal at ΔF.

The mixing properties of the UTC-PD when used as an OPM depend on the bias voltage and the injected optical power [133], hence, both should be optimized.

Therefore, the conversion loss was measured as a function of bias voltage for different levels of optical power, as shown in Fig. 3-5. The figure also shows previous works by Rouvalis et al. [31] and Renaud et al. [136] for a comparison. Here, conversion loss is defined as the ratio between the power of the incoming unmodulated RF signal (measured at the input of the coplanar probe that is connected to the waveguides of the UTC-PD), and the generated IF signal power.

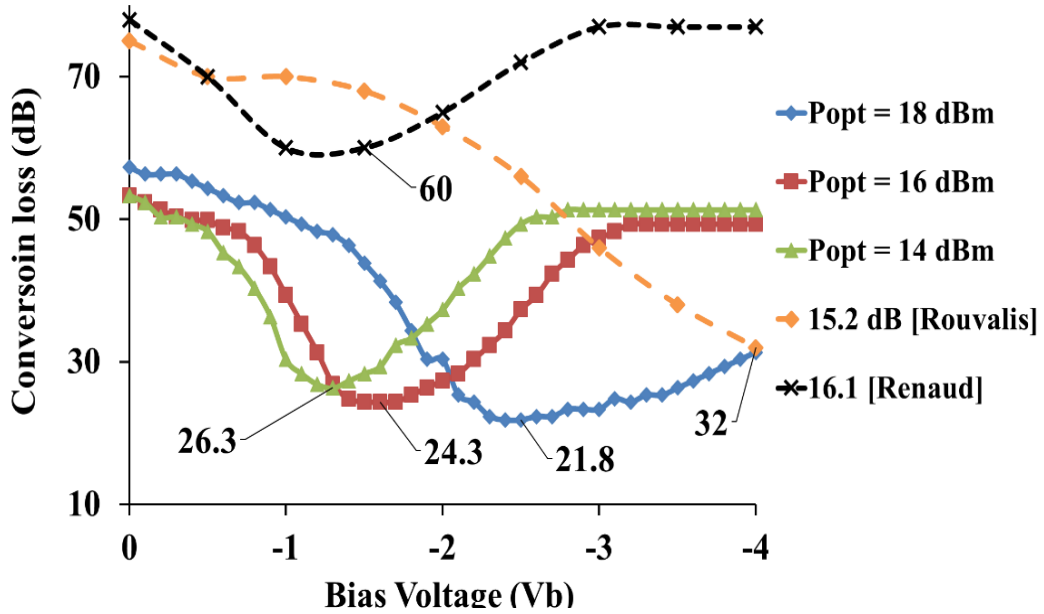

Fig. 3-5: UTC-PD's conversion loss versus bias voltage for different levels of optical power *in comparison to previous works ([31] and [136]).*

Notice in Fig. 3-5 that the minimum conversion loss for the 14 dBm, 16 dBm, and 18 dBm curves takes place at bias voltages of -1.3 V, -1.6 V, and -2.4 V, respectively. Interestingly, these bias voltages correspond to the regions of maximum nonlinearity in the I-V curves of Fig. 3-1. This agrees with the findings of [118] that best mixing occurs at maximum differential conductance.

By comparing the curves in Fig. 3-5, it can be observed that the conversion loss curves in this work behave in a similar manner to that of [Renaud], but very differently to that of [Rouvalis]. This is because the UTC-PD in this thesis has an epitaxial structure similar to that in [Renaud], while a different epitaxial structure is used in [Rouvalis]. Moreover, in [Rouvalis], minimum conversion loss takes

place at the maximum reverse bias voltage because the device epitaxial structure was designed for MMW emission rather than mixing.

Also, it is clear, from Fig. 3-5, that the UTC-PD used in this thesis exhibits much better conversion loss performance compared to the previous works (21.8 dB compared to 58 dB in [Renaud] and 32 dB in [Rouvalis]). This is attributed to several factors summarized below:

- The UTC-PD in this thesis was pumped with more optical power (18 dBm compared to 16.1 in [Renaud] and 15.2 in [Rouvalis]).
- The size of the device used here is bigger (7x15 um^2 compared to 4x15 um^2 in [Renaud] and 2x25 um^2 in [Rouvalis]).
- Here, RF frequency is lower, which means that more power can be generated by the device (35.1 GHz compared to 53 GHz in [Renaud] and 100 GHz in [Rouvalis]).
- Finally, in this work, IF frequency is higher (11.7 GHz compared to 400 MHz in [Renaud] and 50 kHz in [Rouvalis]). As will be seen in Sec. 3.4.1, conversion loss is lower at higher IF.

By comparing the three plots for the UTC-PD of this work, it is observed that lower conversion losses are achievable at higher optical powers and higher bias; minimum conversion loss of 21.8 dB was obtained at −2.5 V and 18 dBm optical power, which is the maximum optical power deliverable by the experimental setup. A plot of the conversion loss as a function of optical LO power, in Fig. 3-6, shows an inverse relation between the two; conversion loss decreases with increasing optical power. Based on this figure, one can extrapolate that the trend of decreasing conversion loss will continue at higher optical powers because the device shows no sign of saturation.

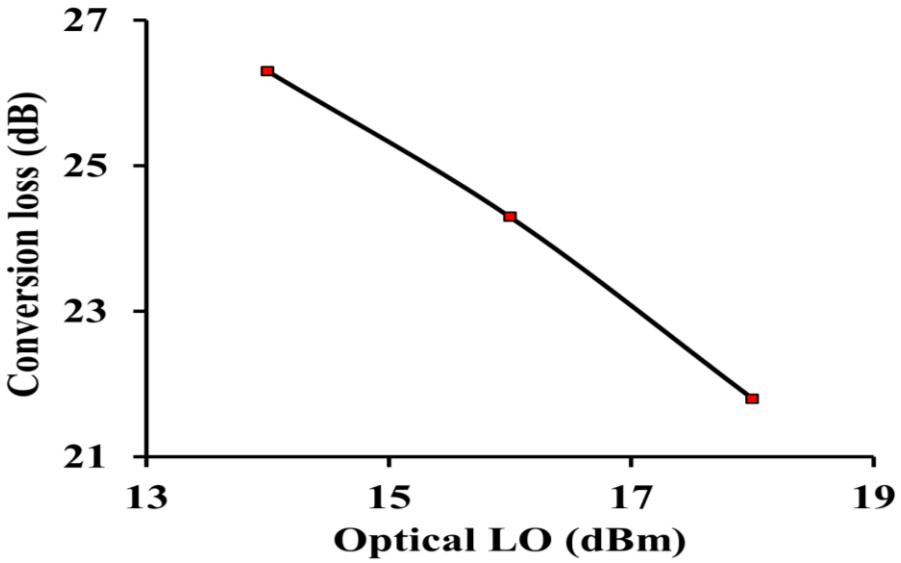

Fig. 3-6: UTC-PD's conversion loss versus optical power.

3.2.2 Designing a Wireless Communication Link at 35.1 GHz

The mixing experiment described in the previous section generated other mixing products due to the mixing of RF and 2ΔF, as seen in Fig. 3-7. Subsequently, when down-converting a modulated RF signal, one should choose ΔF and RF carefully to avoid interference between multiple versions of the down-converted RF signal.

Another constraint is the frequency of operation of components to be used in the wireless transmission experiment, such as amplifiers and antennas, which are limited to 40 GHz. Taking all that into account, RF was chosen to be 35.1 GHz while ΔF was set to 23.4 GHz resulting in 2ΔF = 46.8 GHz. This configuration resulted in two mixing products at the same frequency, IF1 and IF2 at 11.7 GHz.

Figure 3-7 shows the electrical spectrum of the RF signal, the heterodyne signals and their mixing products. The two mixing products are not perfectly matched to the same frequency. Consequently, two IF peaks are observed in the spectrum. This is due to using free running lasers to generate the heterodyne signals, which cannot guarantee a fixed heterodyne frequency, and this would be problematic in communication systems due to interference of the two IFs.

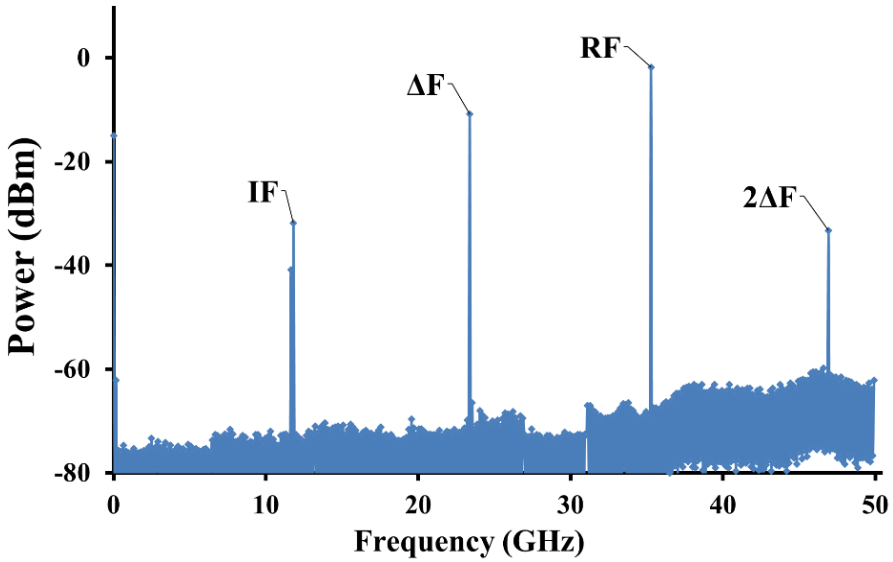

Fig. 3-7: Electrical spectrum showing RF, heterodyne, and IF signals (RBW = 300 kHz, VBW = 30 kHz).

Therefore, a stabilization mechanism is needed to fix the heterodyne frequency. For example, one could use a single laser followed by a modulator to generate coherent optical tones. This solution was successfully implemented in the experiment presented in the following section.

3.2.3 Wireless Transmission Experiment Implementing 5 Gbps UTC-PD-based Receiver

A wireless transmission experiment was conducted to demonstrate the optoelectronic mixing capabilities of the UTC-PD, and how they can be useful at the receiver, by photonically down-converting the incoming mm-wave signals into a lower IF. The experiment was conducted with 5 Gbps data at a carrier frequency of 35.1 GHz and a wireless distance of 1.3 meters. A summary of the experimental parameters is provided in Table 3-1.

Table 3-1: A list of the parameters of the wireless transmission experiment.

Parameter	Value
Carrier Frequency	35.1 GHz
Data Rate	5 Gbps
Modulation	OOK
Transmitted Power	11.8 dBm
Antennae Gain	20 dBi
Wireless Distance	1.3 m
FSPL	25.6 dB
UTC-PD Conversion Loss	22 dB
IF	11.7 GHz
BER	$6x10^{-9}$
Real-time/Offline	Real-time

A block diagram of the experimental system is shown in Fig. 3-8. A single wavelength laser at 1550 nm followed by an intensity modulator generated three optical tones that are spaced by 23.4 GHz. They were followed by a reconfigurable optical filter (WaveShaper^{TM}) to select only two adjacent optical tones (suppression ratio of more than 40 dB). These optical tones are coherent since they originate from an externally modulated laser, and they were used to generate the heterodyne signal on the UTC-PD.

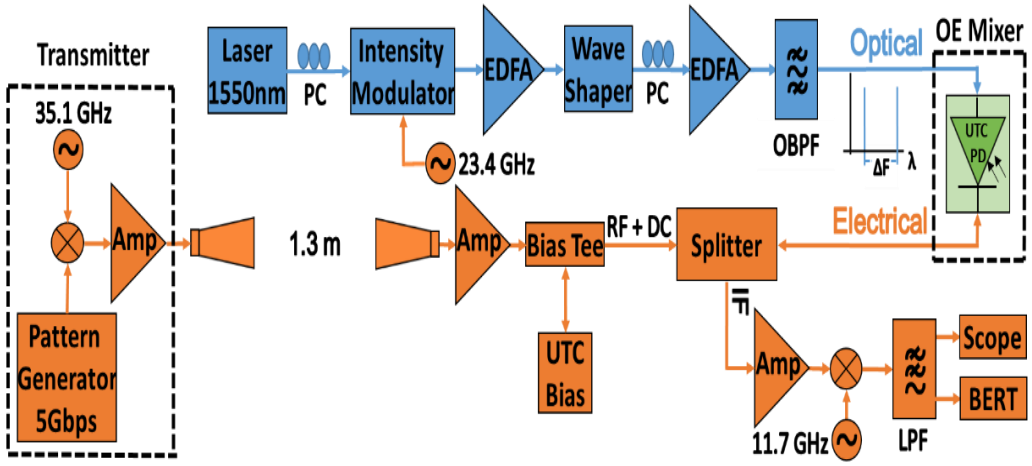

Fig. 3-8: Block diagram of the wireless transmission experiment

Two EDFAs were used to amplify the optical signal followed by a 1 nm-bandwidth optical bandpass filter (OBPF) to reduce the amplified spontaneous emission (ASE) noise. The total power of the optical signal measured at the output of the OBPF was 18 dBm, which gives the lowest conversion loss (22 dB), as shown in Fig. 3-5.

The optical LO was injected into the UTC-PD using a lensed fibre that was not fixed. This provoked measurement sensitivity to disturbances and vibrations in the environment such as air movement caused by people and the air-condition. To combat this, continuous fibre realignment was required to optimize power coupling.

Moreover, the polarization of the optical signal was sensitive to movements and temperature variations. This affected the relative powers of the optical tones at intensity modulator output as well as the polarization of the signal at the input of the UTC-PD. Therefore, continuous polarization control was needed to optimize the power levels of the signals at the modulator output and to ensure matching the polarization of the optical signal to that of the UTC-PD waveguide to maximize optical power coupling to the device.

At the transmitter, a NRZ – OOK 5 Gbps pseudo random bit sequence (PRBS) data with a length of 2^{11} – 1 was generated at the baseband, then, up-converted to 35.1 GHz using a 35.1 GHz signal generator and an electronic mixer. After that, it was amplified (gain of 25 dB, noise figure (NF) of 3 dB) and fed into a 20 dBi horn antenna. The total power of the modulated signal at the transmitter was 11.8 dBm. The signal was transmitted over a wireless distance of 1.3 meters before reaching the receiver 20 dBi horn antenna. This resulted in 25.6 dB of free-space path loss (FSPL) according to the FSPL formula [138]:

$$FSPL = 20\,log(d) + 20\,log(f) + 20\,log\left(\frac{4\pi}{c}\right) - G_t - G_r \qquad eq.\ (3\text{-}1)$$

At the receiver, the signal was amplified (gain of 35 dB, NF of 4 dB) and passed to a bias tee, where it is coupled with the DC bias of the UTC-PD, then, to a splitter, and finally, to a coplanar probe that is connected to the coplanar waveguides of the UTC-PD. The RF signal was opto-electronically mixed with the optical heterodyned LO signal at the UTC-PD resulting in an IF signal at 11.7 GHz. The splitter was used to allow for the simultaneous supply of RF and the extraction of IF signals.

The extracted IF signal was amplified (gain of 35 dB, NF of 4 dB), then, fed into an electronic mixer to down-convert it to the baseband. The locking of the transmitter and the receiver was ensured by connecting the 10 MHz REF ports of the receiver synthesizers to that of the transmitter synthesizer. The final baseband signal was filtered and displayed on the oscilloscope. An open eye diagram of the received signal was obtained, as shown in the inset of Fig. 3-9, and a BER of less than 10^{-8} was measured directly using a bit error rate tester (BERT).

Then, BER performance was evaluated as a function of the transmitted signal power and the UTC-PD's optical LO power, while keeping the same wireless distance, d = 1.3 meters. The transmitted power varied from -2.5 dBm to 11.8 dBm and BER was measured at 18 dBm of optical LO power. The same procedure was repeated for 16 dBm and 14 dBm of optical LO, and results are plotted in Fig. 3-9. As expected, BER decreased as with increasing transmitter power and with increasing optical LO power. The lowest BER ($6x10^{-9}$) was achieved at the highest optical LO power (18 dBm) and the highest transmitted power (11.8 dBm).

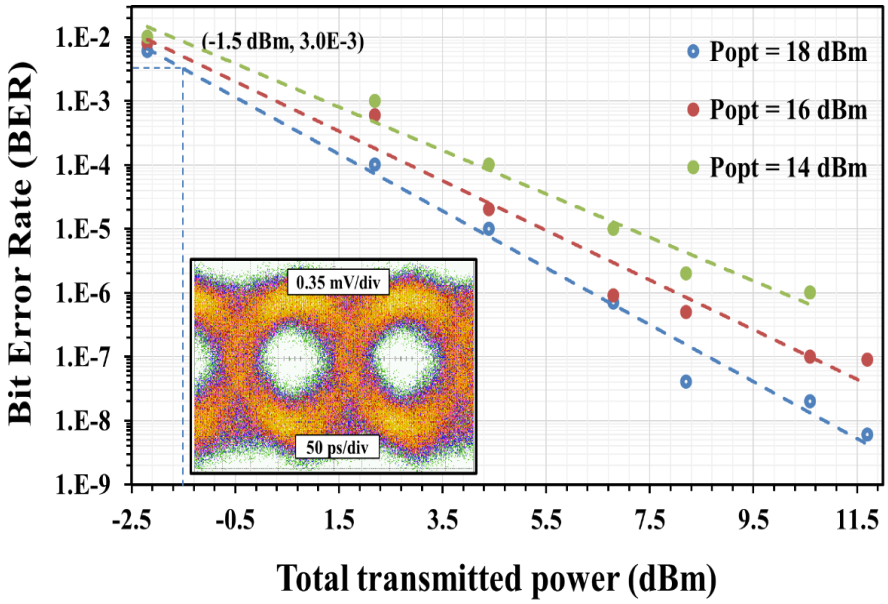

Fig. 3-9: BER performance as a function of transmitted signal power and optical LO power. The inset shows the eye diagram of the received signal after down-conversion to the baseband.

Fig. 3-9 shows that the minimum transmitted power required to satisfy the forward error correction (FEC) limit of $3.8x10^{-3}$ [139] is about -1.5 dBm. This gives more than 13 dB allowance in losses if we are to work at the FEC limit, which corresponds to more than four-fold increase in transmission distance. Combining this with high gain antennas (gain = 42 dBi) would allow for transmission distances of hundreds of meters. To the best of the author's knowledge, this is the first demonstration of a UTC-PD mixer in a receiver.

3.3 1 Gbaud QPSK Wireless Link with an Optically Pumped UTC-PD Mixer at the Receiver

This section presents the first demonstration of a UTC-PD used in a receiver of a wirelessly transmitted QPSK signal. In this demonstration, a 1 Gbaud QPSK signal centered at 33.5 GHz was transmitted over a wireless distance of 1.4 meters using 20 dBi horn antenna. At the receiver, a UTC-PD was used to down-convert the RF signal to an IF of 9.5 GHz by mixing the RF signal with a heterodyne signal at 24 GHz, which was generated by two free running lasers. The down-converted signal was captured by a real-time digital oscilloscope (RTO) for offline digital signal processing (DSP).

The error vector magnitude (EVM) of the demodulated signal was measured at 18%, which corresponds to a BER of 10^{-8} [140]. No higher order modulation transmissions, like: 16-QAM, are reported here because of the high EVM in the system. The parameters of this experiment are summarized in Table 3-2.

Table 3-2: A list of the parameters of the QPSK wireless transmission experiment.

Parameter	Value
Central Frequency	33.5 GHz
Data Rate	2 Gbps
Modulation	QPSK
Transmitted Power	-15.5 dBm
Antennae Gain	20 dBi
Wireless Distance	1.4 meters
FSPL	25.9 dB
UTC-PD Conversion Loss	25.5 dB
IF	9.5 GHz
EVM	18%
Real-time/Offline	Offline DSP

3.3.1 UTC-PD Optoelectronic Mixer Characterization

In this experiment, a UTC-PD was used as an OPM, by which an incoming RF signal at 34.5 GHz is mixed with an optically generated heterodyne signal at a ΔF = 24 GHz to down-convert it to an IF at 10.5 GHz. The minimum conversion loss was 25.5 dB at 18.2 dBm of optical power and -1.7 V voltage bias. The full characterization of the UTC-PD's conversion loss is shown in Fig. 3-10. Again, notice that lower conversion loss is achievable at higher optical powers.

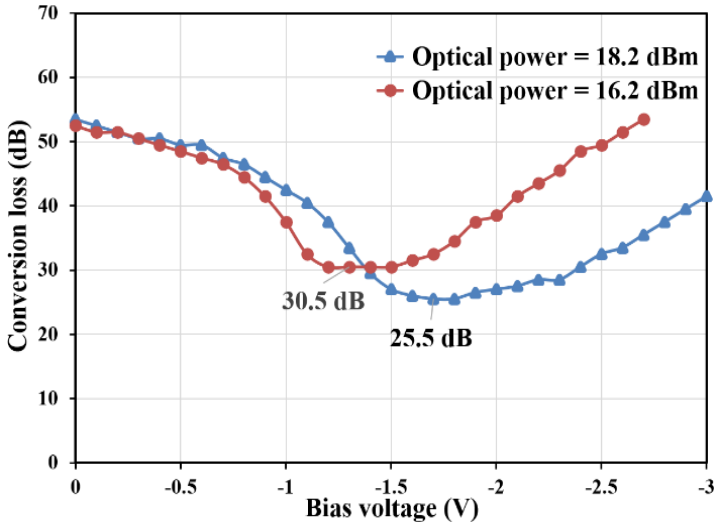

Fig. 3-10: UTC-PD's conversion loss vs. the voltage bias for two different levels of optical power.

3.3.2 Wireless Transmission Experiment Implementing a 1 Gbaud-QPSK UTC-PD-based Receiver

Fig. 3-11 is the block diagram for a 1 Gbaud QPSK wireless transmission experiment. An arbitrary waveform generator (AWG) was used to generate a 1 Gbaud QPSK signal centered at 1 GHz, and shaped with a root raised cosine (RRC) filter with a roll-off factor of 0.35, resulting in a signal bandwidth of 1.35 GHz. The QPSK signal was, then, up-converted using a double-balanced electronic mixer that is driven by a 34.5 GHz LO resulting in two sidebands at 33.5 GHz and 35.5 GHz, similar to the spectrum shown in Fig. 3-12, which shows the signal at the input of the transmitter antenna. These two sidebands are identical and carry the same information. Therefore, detecting only one sideband is enough to recover the data.

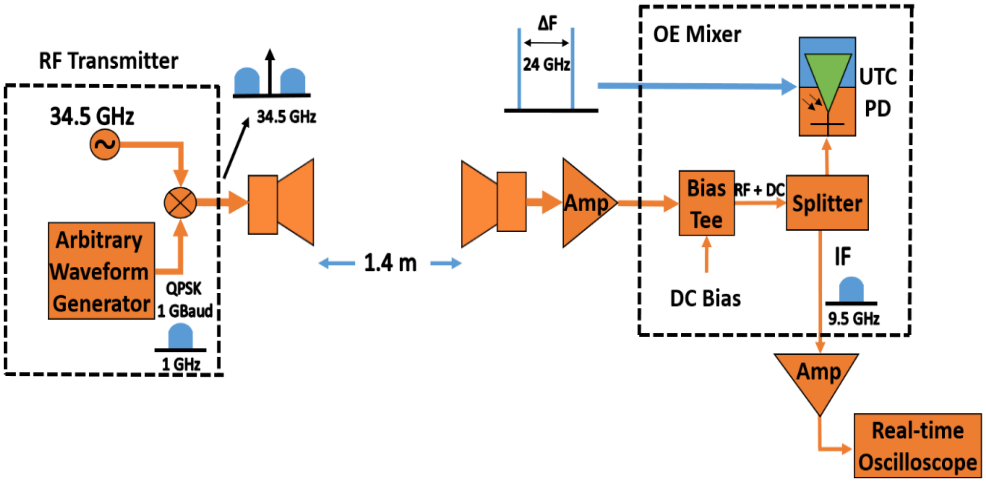

Fig. 3-11: Block diagram of the QPSK wireless transmission experiment.

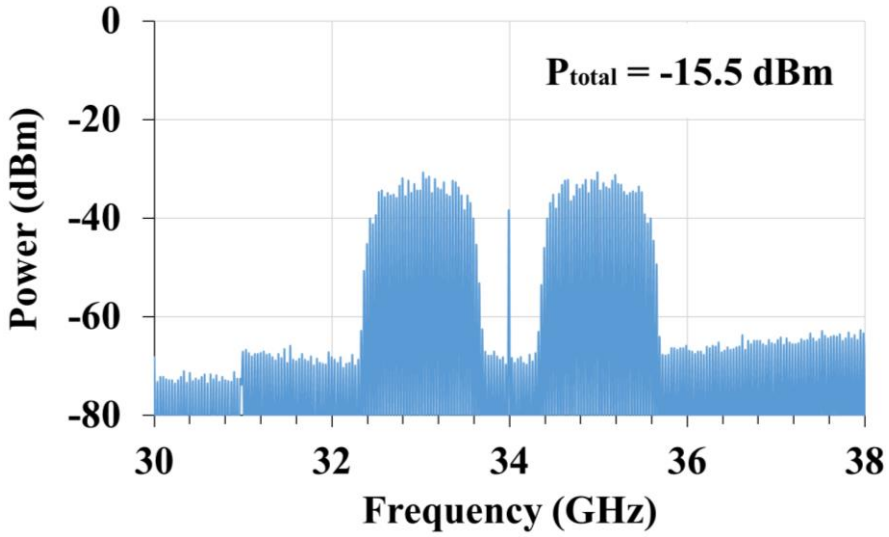

Fig. 3-12: The electrical spectrum of the transmitted signal (RBW = 100 kHz).

The signal was transmitted using a 20 dBi horn antenna over 1.4 meters and detected by an identical receiver antenna. Under these conditions, eq. (3-1) gives 25.9 dB for FSPL. The received signal was amplified by a 40 GHz RF amplifier (gain of 35 dB, NF of 4 dB) and passed through a bias tee and a splitter, onto a CPW probe that is connected to the waveguides of the UTC-PD. The UTC-PD bias was set to -1.7 V, which gives the lowest conversion loss at 18.2 dBm optical power (as measured at the output of the OBPF). The UTC-PD mixed the received signal with the optical heterodyne, and down-converted the RF signal to 10.5 GHz, resulting in the two sidebands centered at 9.5 GHz and 11.5 GHz.

The down-converted signal was amplified (gain of 35 dB, NF of 4 dB), and, captured by the RTO for offline DSP. The offline DSP steps are listed in the flow chart of Fig. 3-13. The RTO has a bandwidth of 36 GHz and a sampling rate of 80 Gsamples/second. The length of the captured time window was 5 μs, which corresponds to 10,000 bits. The captured signal was bandpass filtered, so that only the 9.5 GHz sideband was passed for further digital signal processing.

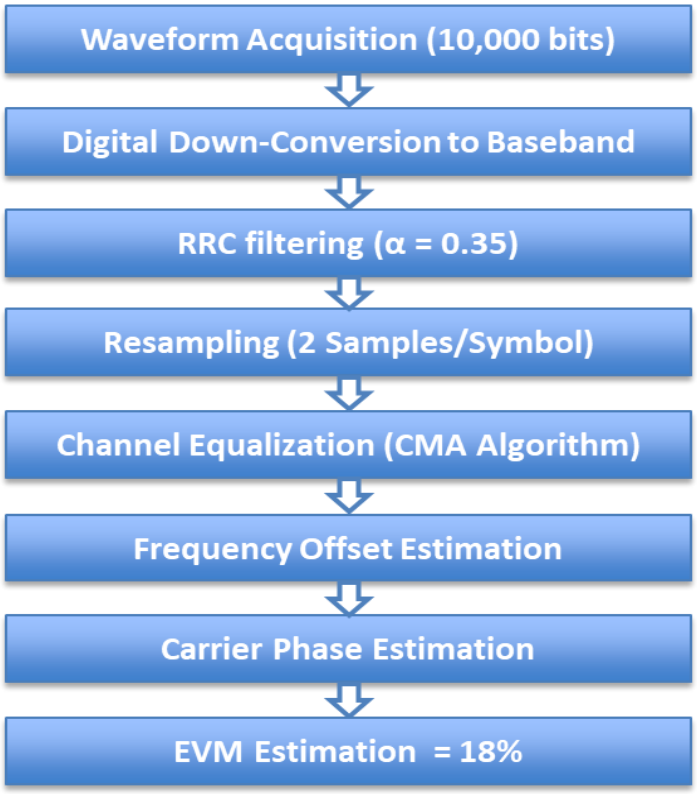

Fig. 3-13: Flow chart showing offline DSP Steps (see MATLAB implementation by Haymen Sham in the appendices A.1 & A.2).

The filtered signal was digitally down-converted to the baseband, then, digitally filtered with an RRC filter with a roll-off factor of 0.35. Fig. 3-14 shows the electrical spectrum of the signal after down-conversion to the baseband. Then, the constant modulus algorithm (CMA) was used for channel equalization. Carrier recovery and phase estimation algorithms were used to compensate for the frequency offset and phase drift produced by the two free-running lasers, since they are not locked to each other [141].

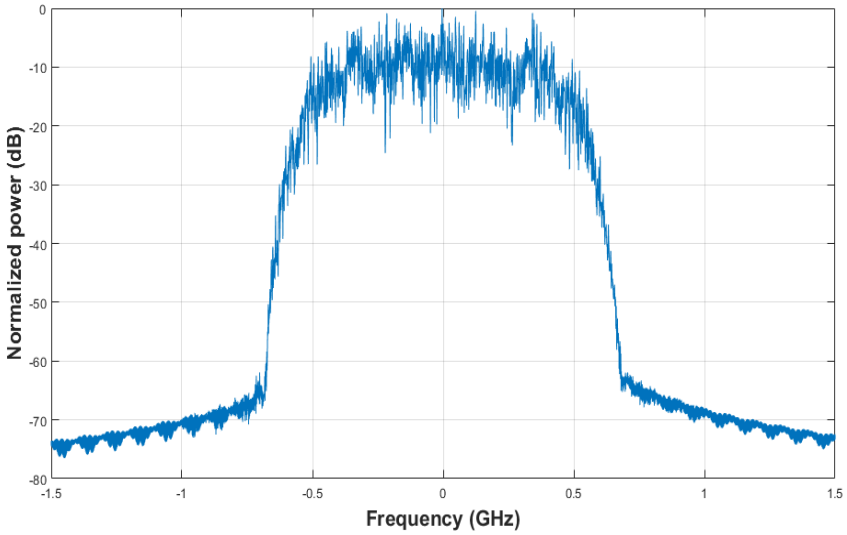

Fig. 3-14: The received QPSK signal after down-conversion to the baseband (RBW=200 kHz).

The transmitted signal was successfully recovered, and the constellation diagram was successfully reconstructed, as shown in Fig. 3-15. The measured EVM of the received signal was 18%, which corresponds to a BER of 10^{-8} [140].

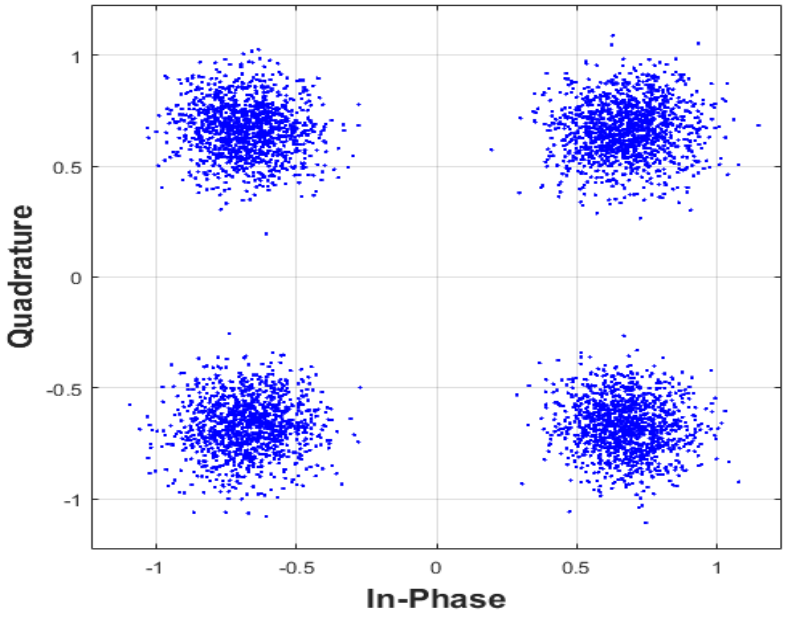

Fig. 3-15: Constellation diagram of the QPSK signal after down-conversion to the baseband.

Longer transmission distances are expected when using a power amplifier at the transmitter and high gain antennas at the transmitter and the receiver. For instance, using a 30 dB-gain power amplifier would allow for more than 30-fold increase in transmission distance.

This experiment proved that it is possible for UTC-PD-based receiver to recover complex data while keeping the receiver setup simple, by utilizing offline DSP techniques. To the best of the author's knowledge, this is the first demonstration of a UTC-PD-based wireless receiver implementing complex modulation format. No higher order modulation transmissions, like: 16 QAM, are reported here due to the large EVM (18%) measured in the QPSK transmission.

3.4 60 GHz wireless Link Implementing UTC-PDs at the Transmitter and the Receiver

This section presents the first demonstration of an MMW transmission link based on UTC-PDs in the transmitter and the receiver. A 61.3 GHz wireless transmission link is realized, which implements a UTC-PD at the transmitter for MMW signal generation, by heterodyning two modulated optical tones originating from an optical frequency comb (OFC) system. Optical signal modulation was realized using a Mach-Zehnder modulator (MZM) driven by a 1 Gbps OOK signal. The 61.3 GHz signal was transmitted wirelessly using a 25 dBi gain parabolic antenna before being detected by an identical receiver antenna.

At the receiver, a UTC-PD was pumped by optical tones from two free running lasers spaced by 55 GHz to down convert the received signal to an IF of 6.3 GHz, where it was captured for offline processing. The recovered data showed an open eye diagram, and a BER of the order of 10^{-5} was measured. To the best of the author's knowledge, this is the first demonstration a UTC-PD-based 60 GHz wireless receiver. A summary of the experimental parameters is provided in Table 3-3.

Table 3- 3: A list of the parameters of the 60 GHz wireless transmission experiment.

Parameter	Value
Carrier Frequency	61.3 GHz
Data Rate	1 Gbps
Modulation	OOK
Antennae Gain	25 dBi
Wireless Distance	0.55 m (actual) 50 m (potentially)
UTC-PD Conversion Loss	39 dB
IF	6.3 GHz
BER	10^{-5}
Real-time/Offline	Offline DSP

3.4.1 UTC-PDs Characterization

The UTC-PD-based transmission link presented in this work uses two UTC-PDs: The first UTC-PD, which has dimensions of 3x15 μm^2, uses optical heterodyning to generate the MMW at the transmitter, while the second UTC-PD, which has dimensions of 4x15 μm^2, is used as an opto-electronic mixer at the receiver. The epitaxial structure of the devices is detailed in [135].

First, both UTC-PDs were characterized in terms of their photocurrent for different values of voltage bias, while the optical power injected into the UTC-PDs was fixed at 14 dBm and 9 dBm for the transmitter UTC-PD and the receiver UTC-PD, respectively. The photocurrent versus voltage bias is plotted in Fig. 3-16. The figure gives responsivities of 0.28 A/W and 0.2 A/W at -4 V for the transmitter and receiver UTC-PDs, respectively.

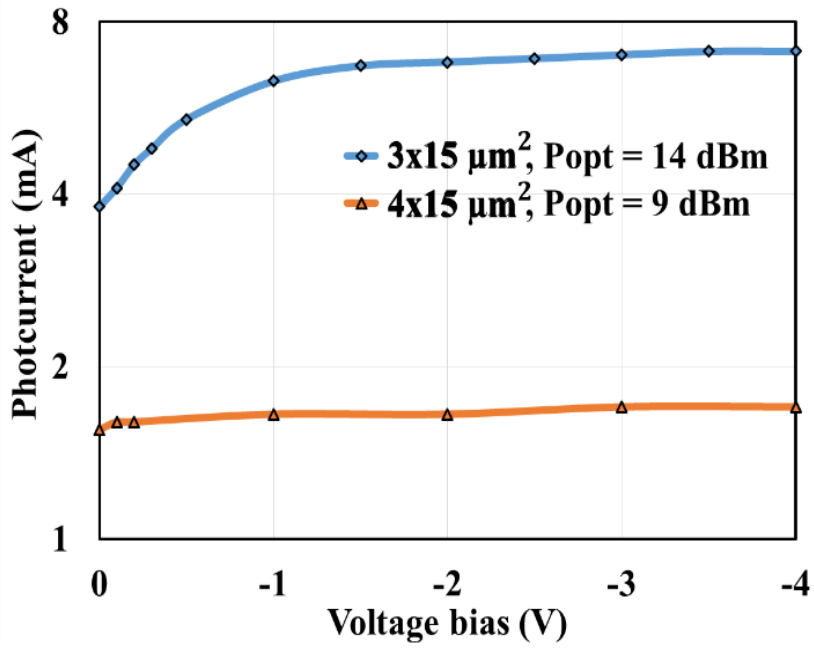

Fig. 3-16: The photocurrent versus bias voltage characteristics for the UTC-PDs at the transmitter (3x15 μm^2) and the receiver (4x15 μm^2).

Then, the frequency response of the devices was measured using the same heterodyne system shown earlier in Fig. 3-2, where optical signals from two free running lasers were coupled and injected into the UTC-PDs. The spacing between

the two optical signals was swept from zero to 67 GHz, while the generated electrical heterodyne signals were extracted by a CPW probe and measured using an electrical spectrum analyzer (ESA).

The frequency responses of the devices are plotted in Fig. 3-17 at a voltage bias of -4 V (the figure also shows the frequency response of the receiver UTC-PD at a voltage bias of -0.2 V, which gives the optimum conversion loss as will be shown next). The frequency response curves give 3 dB-bandwidths of more than 60 GHz and 35 GHz for the transmitter and receiver UTC-PDs, respectively. This difference in bandwidth is attributed to the difference in the devices' dimensions.

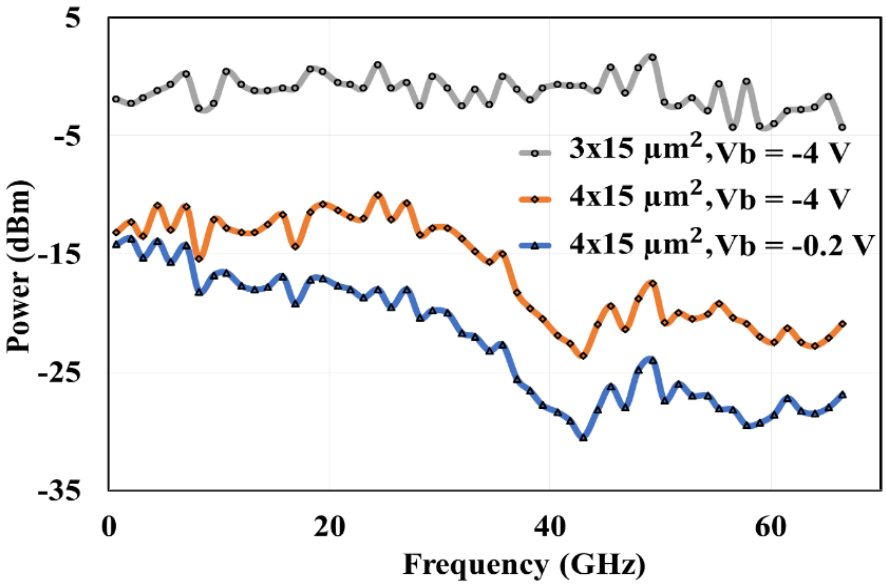

Fig. 3-17: Frequency response of the transmitter and receiver UTC-PDs.

Next, the optoelectronic mixing characteristics of the receiver UTC-PD were studied using the system shown in Fig. 3-2, by applying a 61.3 GHz signal - from a signal generator - with a power of -11 dBm as measured at the input of the UTC-PD probe. Optical tones from two free running lasers were injected into the UTC-PD, and their spacing was swept between 50.3 GHz and 61.3 GHz, and the power of the generated IF was measured (Fig. 3-18), which is a down-converted version of the RF signal at a frequency equal to the difference between the RF and

generated electrical heterodyne. Fig. 3-18 shows that mixing efficiency depends on IF, and that relativly high mixing efficiency occurs at 6.3 GHz.

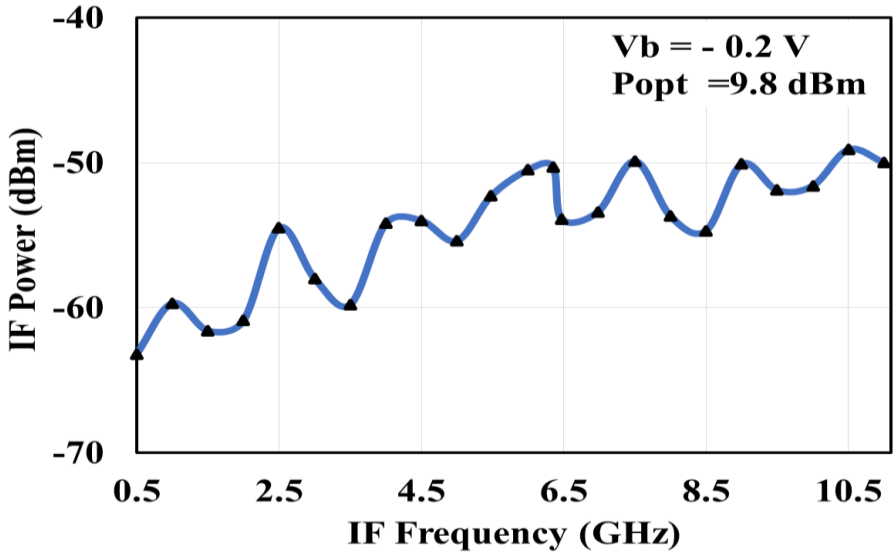

Fig. 3-18: Dependence of IF power on frequency for the receiver UTC-PD.

To find the optimum conversion loss for this mixer, the voltage bias was swept from zero to -4 V while the optical LO power was fixed at 9.8 dBm, and the power of the 61.3 GHz RF was set to -11 dBm as measured at the input of the UTC-PD probe. Results are plotted in Fig. 3-19, which shows that minimum conversion loss (39.3 dB) is obtained at -0.2 V.

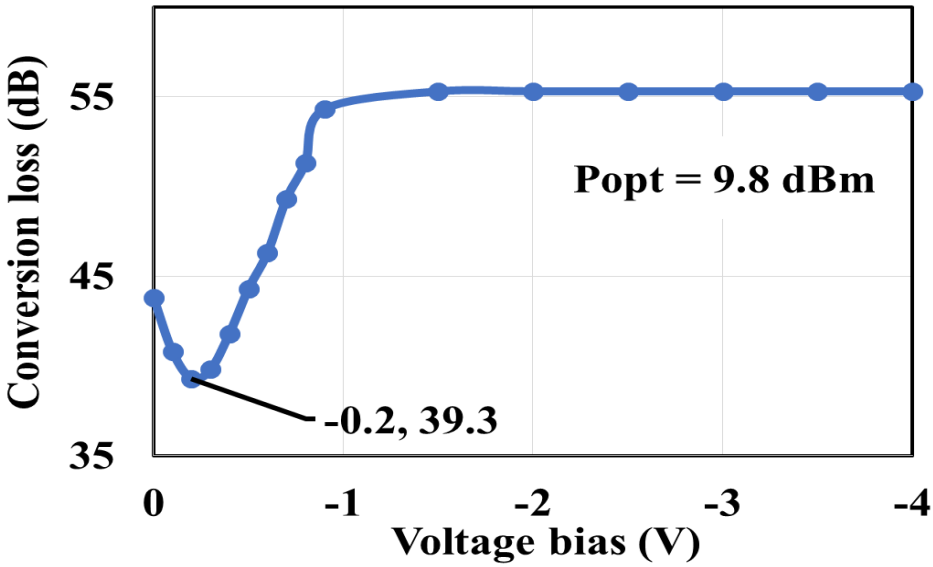

Fig. 3-19: Finding the optimum bias point for the UTC-PD mixer at 6.3 GHz IF.

Finally, the UTC-PD opto-electronic mixer was characterized in terms of its NF using the NF equation (in its logarithmic form) [142]:

$$NF = N_o - G - (-174) \qquad \text{eq. (3-2)}$$

where N_o refers to the noise power density generated by the UTC-PD measured in dBm/Hz, G refers to the gain of the UTC-PD mixer in dB, and finally the –174 dBm/Hz term is the thermal noise power spectral density at 290 K. The "Noise Meas" function in ESA was used to measure N_o at 6.3 GHz both when the optical LO was OFF and ON. An LNA (gain = 32.8 dB, NF = 1.9 dB) was added after the UTC-PD to amplify the UTC-PD generated noise to increase the measurement accuracy. The optical LO was turned off at first, and N_o was measured for the ESA noise floor and the LNA combined (N_o_OFF = -140.7 dBm/Hz). Then, the optical LO was switched on, and the new N_o was measured (N_o_ON = -137.4 dBm/Hz). Then, N_o for the UTC-PD alone was calculated by subtracting N_o_OFF and the LNA gain from N_o_ON in linear units. At the optimum bias point (-0.2 V), a NF of 40.36 dB was measured at an IF of 6.3 GHz.This high value of NF is mainly dominated by the high conversion loss of the UTC-PD. Therefore, reducing the conversion loss of the UTC-PD is essential for improving the sensitivity of the receiver. In addition, adding an LNA after the receiver antenna would reduce the NF of the receiver, as explained in the next section.

3.4.2 A 60 GHz UTC-PD-based transmission link

- **Transmitter Setup**

The block diagram of the transmitter is shown in Fig. 3-20, where a 1 Gbps NRZ OOK PRBS data signal with a length of $2^{11} - 1$ was emitted at 61.3 GHz by the 3x15 μm^2 UTC-PD by heterodyning two modulated optical tones originating from an OFC system.

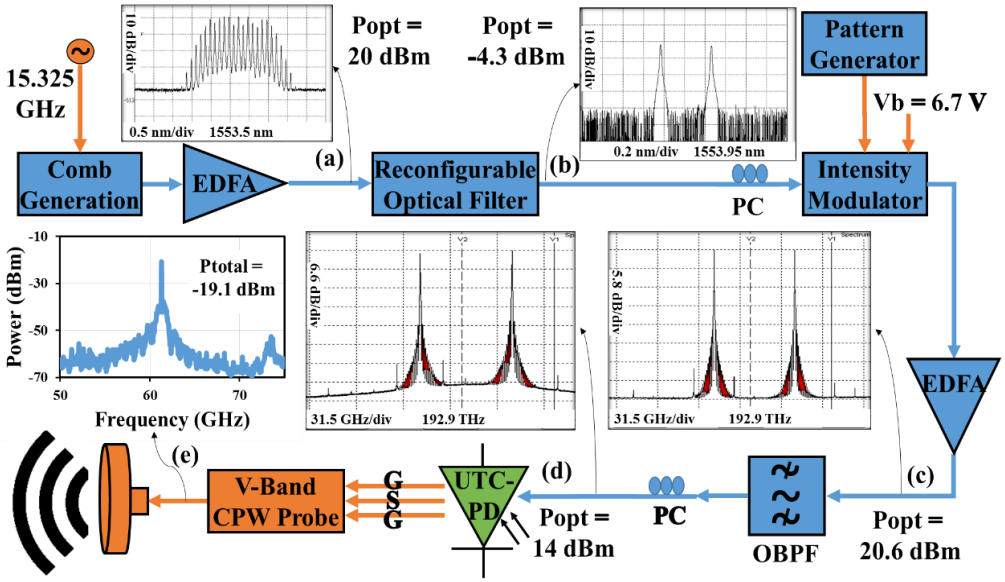

Fig. 3-20: Block diagram of the transmitter showing: (a) the optical spectrum of the OFC (RBW = 0.01 nm), (b) two selected comb lines with 61.3 GHz spacing (RBW = 0.01 nm), (c) the two comb lines after modulation and amplification (RBW = 140 MHz), (d) the optical spectrum at the input of the lensed fibre (RBW = 140 MHz), and (e) the electrical spectrum of the generated MMW signal at the input of the transmitter antenna (RBW = 300 kHz).

The OFC system generated comb of lines centered at 1553.5 nm and spaced by 15.325 GHz, as shown in Fig. 3-20-a. The comb was amplified by an EDFA with a constant output power of 20 dBm followed by a reconfigurable optical filter (Waveshaper^{TM}) to select two optical lines spaced by 61.3 GHz (4 x 15.325 GHz) while suppressing all the other lines (suppression ratio > 37 dB), as shown in Fig. 3-20-b. The total power of the two-tone optical signal at the output of the reconfigurable filter was measured at -4.3 dBm. An MZM, biased at V_b = 6.7 V, was used to modulate the two optical tones with a 1 Gbps OOK data signal generated by a pattern generator.

After that, the optical signal was amplified by an EDFA (output = 21 dBm). The optical spectrum of the modulated optical tones after amplification is shown in Fig. 3-20-c, and the total power at the output of the EDFA was measured at 20.6 dBm. The EDFA was followed by a 1 nm-wide OBPF to reduce the ASE noise. Finally, the optical signal was coupled to a lensed fibre to illuminate the UTC-PD. The total power of the optical signal at the input of the lensed fibre was measured at 14 dBm, and the optical spectrum at this stage is shown in Fig. 3-20-d.

The UTC-PD generated an electrical heterodyne signal at 61.3 GHz, which was extracted by a V-band (50 GHz – 75 GHz) CPW probe with an integrated bias tee applying a voltage bias of -4 V. A 60 GHz V–cable was used to send the extracted 61.3 GHz signal to the transmitter antenna, which is of the parabolic type with a gain of 25 dBi at 61.3 GHz. The electrical spectrum of the transmitted signal is shown in Fig. 3-20-e, and the total power of the signal at this stage was -19.1 dBm. The signal was transmitted over 0.55 m of wireless distance (limited by the physical space available) before reaching the receiver antenna, which is identical to the transmitter antenna.

- **Receiver Setup**

The block diagram of the receiver system is shown in Fig. 3-21. It implements a UTC-PD in an OPM configuration to down-convert the incoming 61.3 GHz data signal to a lower 6.3 GHz IF. The optical LO was generated from two free running ECLs spaced by 55 GHz. As shown in Fig. 3-21, the two optical tones were coupled using an optical coupler, amplified by an EDFA (output = 17 dBm), filtered by an OBPF and injected into the UTC-PD using a lensed fibre. The total power of the optical signal at the input of the lensed fibre was measured at 9.8 dBm, and the optical spectrum at this stage is shown in Fig. 3-21-a.

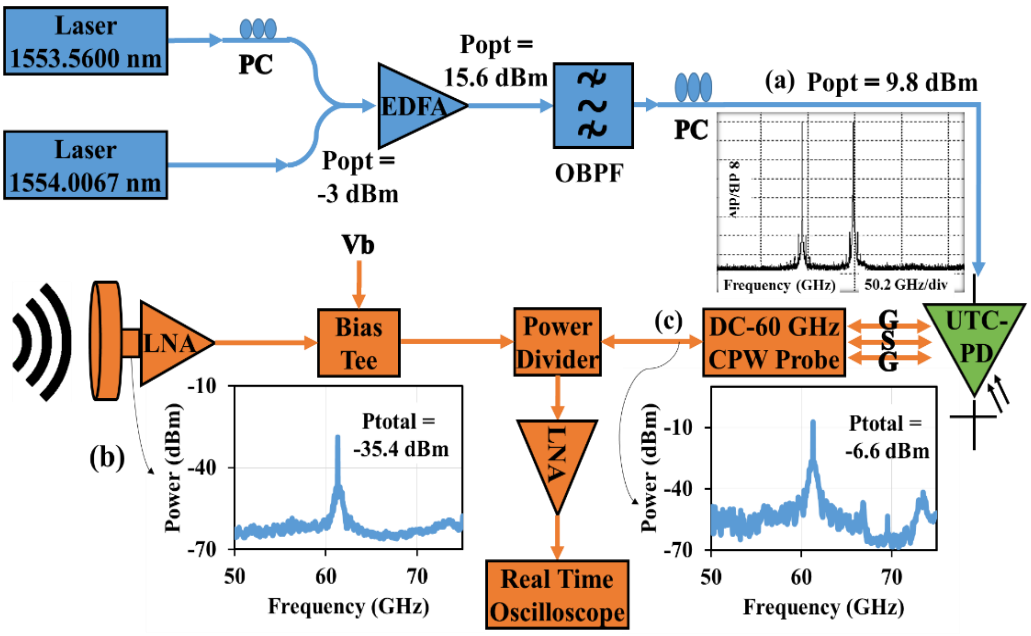

Fig. 3-21: Block diagram of the receiver showing: (a) the optical spectrum at the input of the lensed fibre (RBW = 140 MHz), (b) the electrical spectrum of the MMW signal at the output of the receiver antenna (RBW = 300 kHz), and (c) the electrical spectrum of the MMW signal at the input of the receiver UTC-PD probe (RBW = 300 kHz).

The total power of the 61.3 GHz data signal at the receiver antenna was -35.4 dBm (Fig. 3-21-b). The received signal was amplified by a low noise amplifier (LNA) (gain = 35.9 dB, NF = 2.2 dB) followed by a bias tee to provide the voltage bias (-0.2 V) to the UTC-PD. A DC to 65 GHz power divider was used to allow for the simultaneous supply of the RF signal to the UTC-PD and the extraction of the IF from the UTC-PD. The signal at the input of the receiver UTC-PD probe is shown in Fig. 3-21-c, and its total power was measured at -6.6 dBm.

The extracted IF signal from the power divider was then amplified (gain = 35.4 dB, NF = 1.9 dB) and, finally, captured by the RTO for off-line processing. The length of the captured waveform is 10 µs, which is equivalent to 10,000 bits. The electrical spectrum of the acquired waveform is shown in Fig. 3-22. In that figure, the lines that appear in the spectrum are not part of the down-converted data signal, but a combination of clock signals generated from the RTO (at multiples of 5 GHz) and signals picked up from the lab environment.

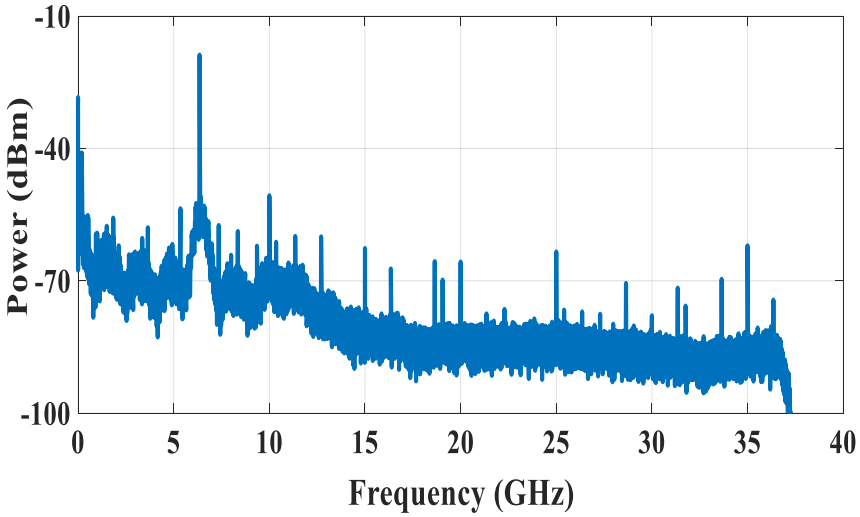

Fig. 3-22: The electrical spectrum of the amplified IF signal (RBW = 100 kHz).

The offline DSP includes the following steps: signal filtering, digital down-conversion to the baseband, channel equalization using CMA, and envelope detection [141]. The recovered data produced an open eye diagram, as shown in Fig. 3-23. The number of errors in the recovered data was counted, by comparing the received and the transmitted bits, and found to be zero in a 10,000-bit transmission. To obtain more precise results, transmission was repeated 35 times, which corresponds to 350,000 bits, and the total number of errors obtained was 3, corresponding to BER of the order of 10^{-5}, which will allow for error-free transmission when FEC is employed.

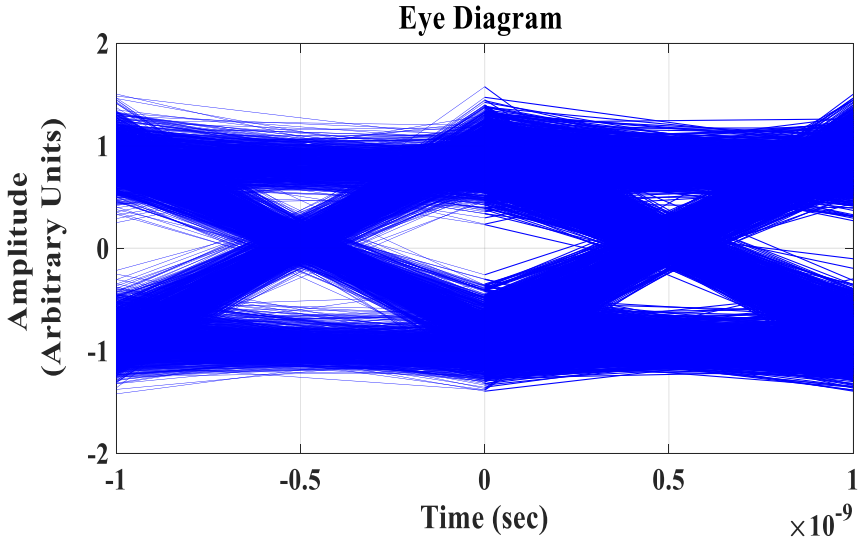

Fig. 3-23: An eye diagram representation of the recovered data after equalization.

- **Discussion of Results**

In the previous experiment the transmission distance was limited to 0.55 meters, partly due to the absence of a power amplifier at the transmitter. To achieve longer transmission distances a similar experiment was conducted using 4x15 μm^2 and 3x15 μm^2 UTC-PDs at the transmitter and the receiver, respectively, with a power amplifier installed at the transmitter (gain = 43 dB, NF = 0.9 dB). In the new setup the transmitter and the receiver antennas were intentionally misaligned to emulate a longer transmission distance. The distance between the antennas was 0.58 m, and the extra attenuation introduced by antenna misalignment was measured at 38.7 dB, which is equivalent to 86-fold increase in distance (d_{new} = 50 m). Fig. 3-24 shows the electrical spectrum of the received signal at the input of the CPW probe at the receiver UTC-PD.

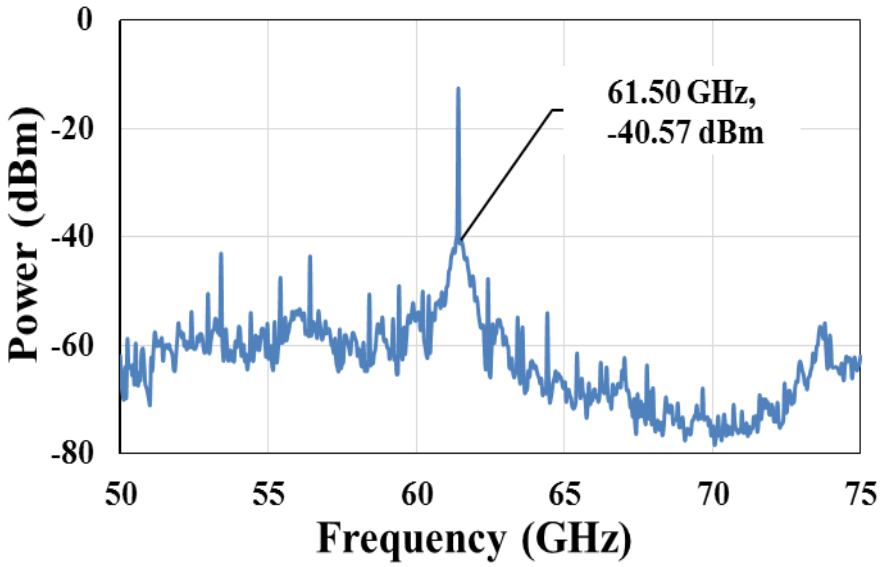

Fig. 3-24: Electrical spectrum of the signal at the receiver UTC-PD.

The UTC-PD down-converted the received signal to an IF of 6.3 GHz. Then, the same offline DSP steps described in the previous section were applied here. Fig. 3-25 shows the electrical spectrum of the received signal after digital down-conversion to the baseband. Also, Fig. 3-26 shows the eye diagram of the recovered data.

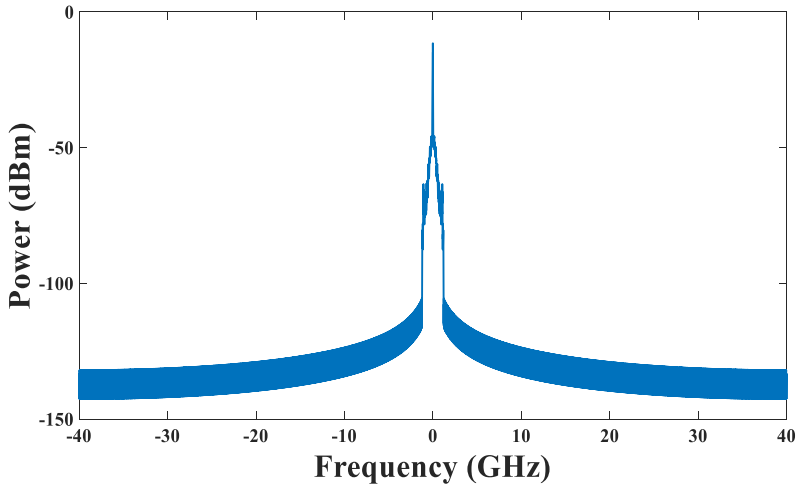

Fig. 3-25: Electrical spectrum of the received signal after digital down-conversion to the baseband.

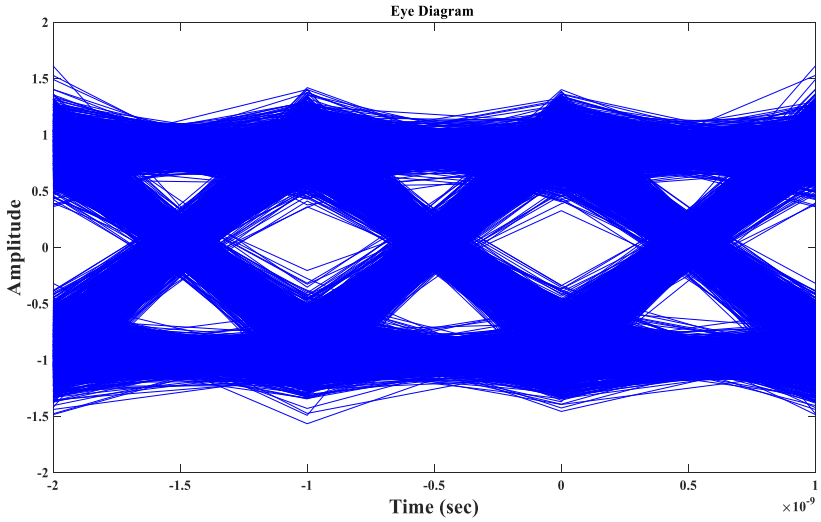

Fig. 3-26: The eye diagram of the recovered data.

The number of errors in the recovered data was calculated in 10,000-bit long transmissions. Transmission was repeated 12 times, which corresponds to 120,000 bits, and the number of errors was zero in all transmissions, which suggests a BER of less than 10^{-5}.

Finally, all the components in the receiver were characterized in terms of their gain/loss and NF. A summary of these measurements is provided in Table 3-4. Then, Friis formula [143] was used to calculate the receiver's overall NF:

$$F_{tot} = F_1 + (F_2 - 1)/G_1 + (F_3 - 1)/G_1G_2 + \ldots \qquad \text{eq. (3-3)}$$

where F_{tot} is the total NF of the receiver, F_n and G_n are the NF and the gain of the n^{th} stage, respectively. Calculations give an overall NF of 21.5 dB for the receiver.

Table 3-4: NF and gain/loss measurements for the components in the receiver.

Stage	Gain (dB)	NF (dB)
RF LNA	35.9	2.2
Passive elements in RF path (bias Tee, power divider, cable, connectors)	-16.5	0
UTC-PD mixer	-39.3	40.36
Passive elements in IF path (power divider, cable, connectors)	-12.7	0
IF LNA	35.4	1.9

The data rates demonstrated in this paper were limited to 1 Gbps. This is partly due to the high carrier to data ratio of the transmitted signal (Fig. 3-20-e) due to the weak modulation depth of the MZM, and this limited the SNR of the transmitted signal, and so, the data rate. Amplifying the data signal at input of the MZM could help increase the modulation depth and the data rates. Also, the current configuration of the receiver can be optimized to allow for longer transmission distances and higher data rates. For example, the receiver uses a DC-65 GHz power divider to allow for the simultaneous supply of RF and the extraction of IF signals. However, this introduces losses to both signals and deteriorates the SNR. Further, it limits the operating frequency to 65 GHz. These limitations can be overcome by redesigning the waveguides of the receiver UTC-PD to create separate paths for RF and IF signals. Another major limitation is the high conversion loss of the UTC-PD mixer (39.3 dB), which requires further studies on optimizing its epitaxial structure to enhance its mixing efficiency, which will increase the sensitivity of the receiver and allow for higher data rates.

As a final remark, although this setup is not optimized it demonstrates a proof of concept of mixing in UTC-PD and how it can be useful in wireless receivers. In that regards, it was verified that mixing took place in the UTC-PD, and not somewhere else, like an LNA, for instance. This is because the

optoelectronic mixing experiment described in Fig. 3-2 does not implement an LNA. Also, the frequency of the down-converted signal in Fig. 3-22 was tunable by adjusting the spacing between the two optical tones driving the receiver UTC-PD, and the power of this signal was dependent on the voltage bias on the receiver UTC-PD following the behavior shown in Fig. 3-19.

3.5 Conclusions

This chapter presented, for the first time, successful demonstrations of optically pumped UTC-PDs implemented in wireless receivers. The best conversion loss obtained was 22 dB, which, while lower than previously reported values is high relative to conventional electronic mixers. However, the advantage of using the UTC-PD as a mixer becomes more significant at higher frequencies where electronic mixers are less attractive as they require expensive electronic LO. The frequency of the LO used for the UTC-PD is defined by the frequency spacing between the two optical tones, which can be broadly tuneable offering the frequency agility of this photodiode-based receiver.

In the 5 Gbps OOK experiment, one laser source followed by a modulator were used to generate coherent optical tones. The advantage of this method is that it provides frequency stability, but at the expense of added complexity as it requires a modulator that is driven by an RF synthesizer. On the other hand, the 1-Gbaud QPSK and the 60 GHz experiments used two free running lasers to generate the heterodyne signal on the UTC-PD. This method is simpler as it does not require a modulator nor a signal generator, but it suffers from frequency offset and phase drift since the two lasers are not locked to each other. However, these impairments have been successfully overcome thanks to using carrier recovery and phase estimation algorithms.

This method offers wide tuneability of the operating frequency simply by adjusting the wavelength spacing between the two lasers. Also, it allows for higher frequencies of operation without the need for an electronic LO, which is the case in conventional electronic mixers.

This first experiment successfully demonstrated transmission over a wireless distance of 1.3 m of a 5 Gbps OOK data signal occupying a 10 GHz bandwidth centred at a carrier frequency of 35.1 GHz using the UTC-PD as an optoelectronic mixer at the receiver. The second experiment successfully demonstrated wireless transmission over 1.4 m of a 1 Gbaud QPSK data signal centred at a carrier frequency of 33.5 GHz using the UTC-PD as an optoelectronic mixer at the receiver. In both experiments, transmission distances are limited by the available antenna gain. Using high gain antennas (42 dBi) would allow transmission distances of hundreds of meters when combined with FEC.

The third experiment successfully demonstrated a 1 Gbps OOK and a potentially 50 m long wireless link at 61.3 GHz implementing UTC-PDs at the transmitter and the receiver. While the transmitter UTC-PD was driven by coherent optical tones from a frequency comb system, the receiver UTC-PD was driven by two free running lasers, featuring a simple and widely tunable receiver.

The current configuration of the receiver is partly limited by the power divider which introduces losses in the RF and the IF paths and limits the operating frequency of the receiver to 65 GHz. These limitations can be overcome by redesigning the waveguides of receiver UTC-PD such that RF supply and IF extraction are done using two different probes.

While the carrier frequency is not limited by the UTC-PD device itself as it could operate up to hundreds of GHz [110], these proof of concept experiments

were done at carrier frequencies of up to 60 GHz, where propagation losses are low enough to easily assess the performance of the transmission system.

This work could find interesting applications in future 5G or beyond networks since the frequencies at which these experiments were done are among the candidate frequencies for 5G [134].

The experiments described in this chapter were done using non-integrated components. To the best of the authors' knowledge, this is the first implementation of the UTC-PD in MMW wireless receivers. These demonstrations show the potential of the UTC-PD in wireless receivers. Based on these promising results, the possibility of photonic integrated receivers has been investigated in the next chapter as it offers important advantages such as low-cost, small size and energy efficiency.

Chapter 4: Photonic Integrated MMW Transceivers

4.1 Introduction

This chapter presents the characterization results of a photonic integrated circuit (PIC) that comprises UTC-PDs, lasers, optical amplifiers and modulators. Also presented in this chapter is the implementation of this PIC in MMW wireless transmission and reception experiments, featuring the world's first photonic integrated transceiver that offers a small-size and low-cost solution for 5G and future networks.

The PIC was characterized by optical heterodyning and optoelectronic mixing both with two lasers operating in a single-mode and with a single laser operating in a multi-mode regime. The objective of these characterizations was to assess the capabilities of the PIC as an MMW emitter and an MMW mixer for the purpose of data transmission and reception, respectively.

The two-laser case has shown wavelength spacing tuneability from 70.5 GHz to 92.4 GHz. When an RF signal at 70 GHz was supplied to the UTC-PD with the optimum voltage bias, the UTC-PD successfully down-converted the RF signal to an IF that was tuneable from 0.5 GHz to 16.4 GHz.

Successful mixing was also achieved in the multi-mode single-laser case. This regime was utilized in data transmission and reception experiments because the spacing between the modes was 52 GHz, which makes it suitable for 60 GHz wireless communication links. In the transmission mode, optical heterodyning on the UTC-PD was utilized to generate a 1 Gbps OOK data signal at 52 GHz. The data signal was transmitted over a wireless distance of 0.5 meters and detected at the receiver, which incorporated an electronic mixer. In the reception mode, a 0.5 Gbps OOK data signal was generated at 63.4 GHz by means of optical heterodyning on a PIN-PD, after which, it was transmitted wirelessly over 3 m.

The receiver utilized optically pumped mixing on the same UTC-PD to down-convert the signal to a low intermediate frequency for processing. Both transmitter and receiver modes have shown zero error bits in 10,000 bit-long transmissions.

4.2 PIC Characterization

As shown in Fig. 4-1, the monolithically integrated chip used in this work [46] incorporates two UTC-PDs, two distributed feedback (DFB) lasers to provide the optical heterodyne, several semiconductor optical amplifiers (SOAs) to amplify the optical signals, multimode interference (MMI) couplers and electro-absorption modulators (EAMs). Moreover, this chip has an optical monitoring output.

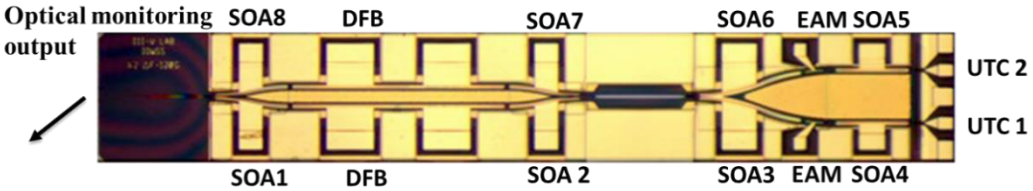

Fig. 4-1: Picture of the photonic integrated circuit *[46]*.

4.2.1 Two Single-Mode Lasers Case

In order to assess the performance of the PIC as an MMW emitter, a heterodyning experiment was conducted, as shown in Fig. 4-2, by which the lasers and SOAs were biased using a multi-contact DC probe, and the generated electrical heterodyne signal at ΔF was extracted using a coplanar probe from UTC1 shown in Fig. 4-1. Consequently, SOA5 and SOA6 were disconnected as they are in the optical path of UTC 2. Also, SOA1 and SOA8, which are used to amplify the optical signal for monitoring purposes, were disconnected to minimize reflections. The total current supplied to the other SOAs was fixed at 467 mA. A bias tee was used to apply the bias to the UTC-PD, which was fixed at -2 V.

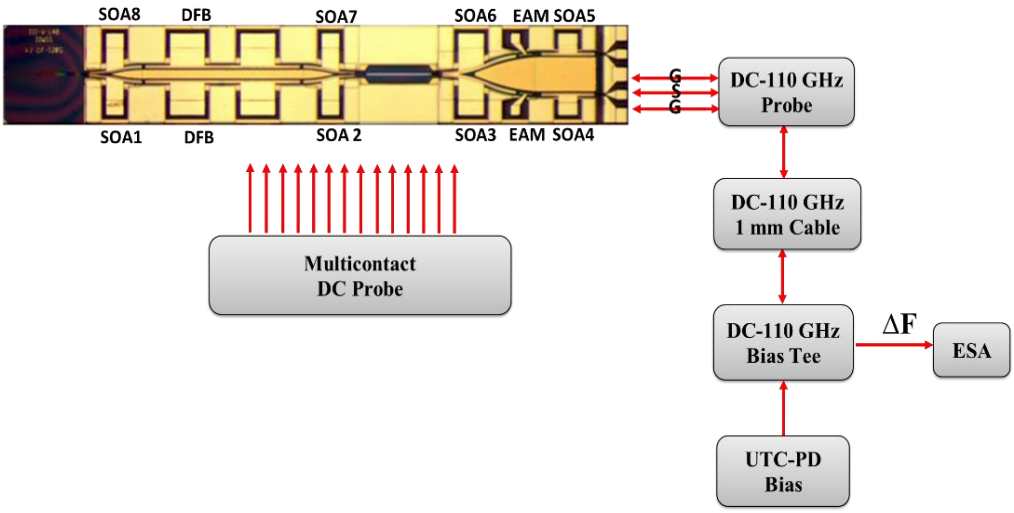

Fig. 4-2: Optical heterodyning experiment.

By monitoring the optical output of the PIC, it was observed that the DFB lasers' threshold currents were 54 mA for DFB1 and 40 mA for DFB2. The lasers bias currents were gradually increased (up to 100 mA for DFB1 and 113 mA for DFB2) causing their operating wavelengths spacing to change. The wavelength tuning was observed by monitoring both the optical spectra and the generated electrical heterodyne. Wide tuneability from 70.5 GHz to 92.4 GHz was achieved, as shown in Fig. 4-3.

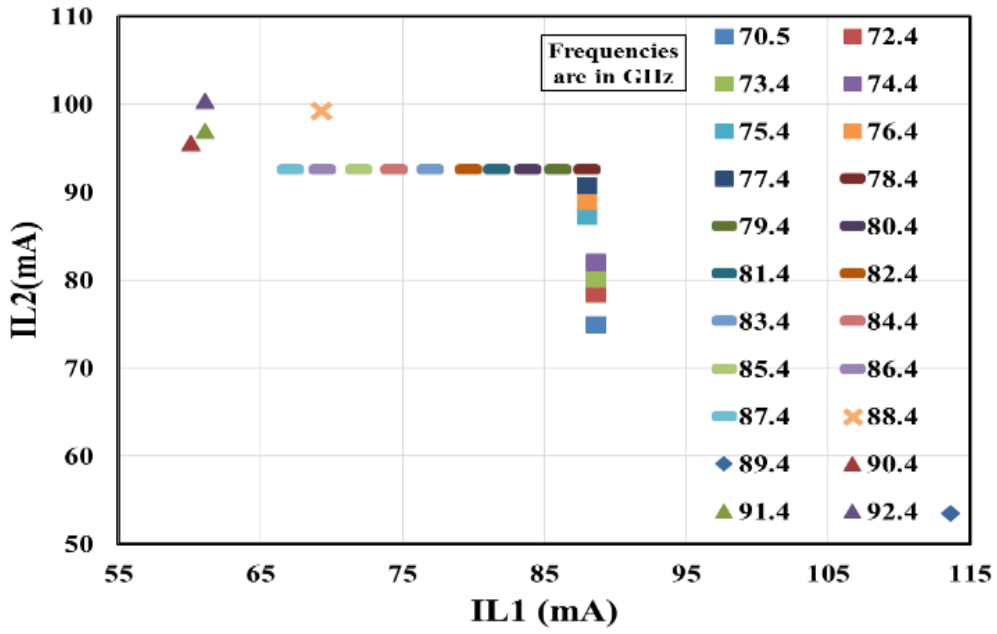

Fig. 4-3: Wide tuneability of the electrical heterodyne.

The electrical spectra of the generated electrical heterodyne signals were measured, as shown in Fig. 4-4, using an ESA which has a 75 GHz to 110 GHz mixer at its input. Further, photocurrent variation between 6.5 mA and 7.2 mA was observed. This is due to the large variation in the lasers bias currents, as shown in Fig. 4-3, which caused the power of the optical signal at the input of the photodiode to vary.

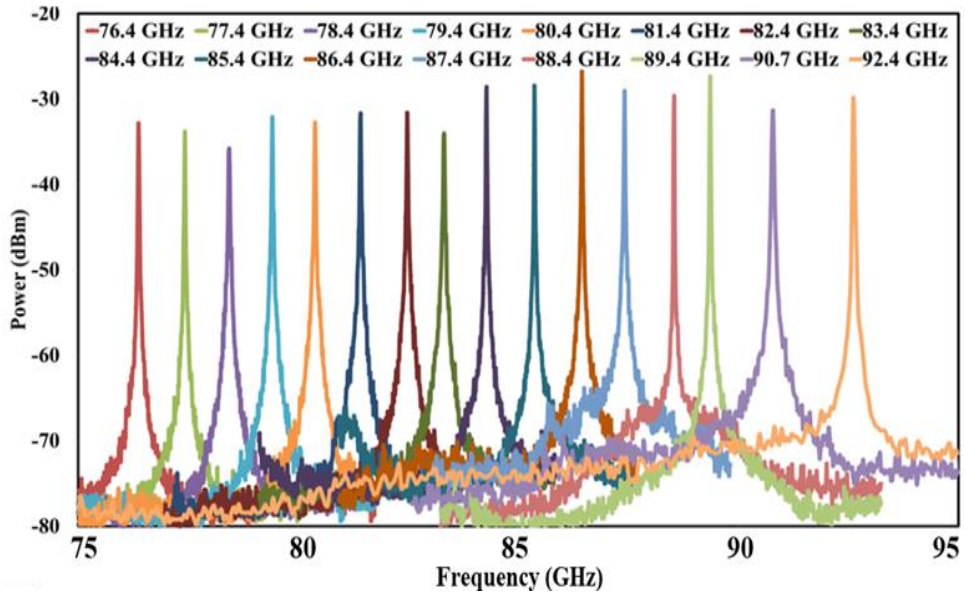

Fig. 4-4: Spectra of the electrical heterodyne (RBW = 300 kHz).

Next, the PIC's optoelectronic mixing capability was assessed. The block diagram of our OPM experiment is shown in Fig. 4-5. In OPM, the UTC-PD is injected with two optical tones to generate the electrical heterodyne signal at ΔF. When an RF signal was supplied to the UTC-PD with a voltage bias, the UTC-PD generated a replica of the RF signal at IF. The power of the generated IF is maximized as the optimum voltage is supplied.

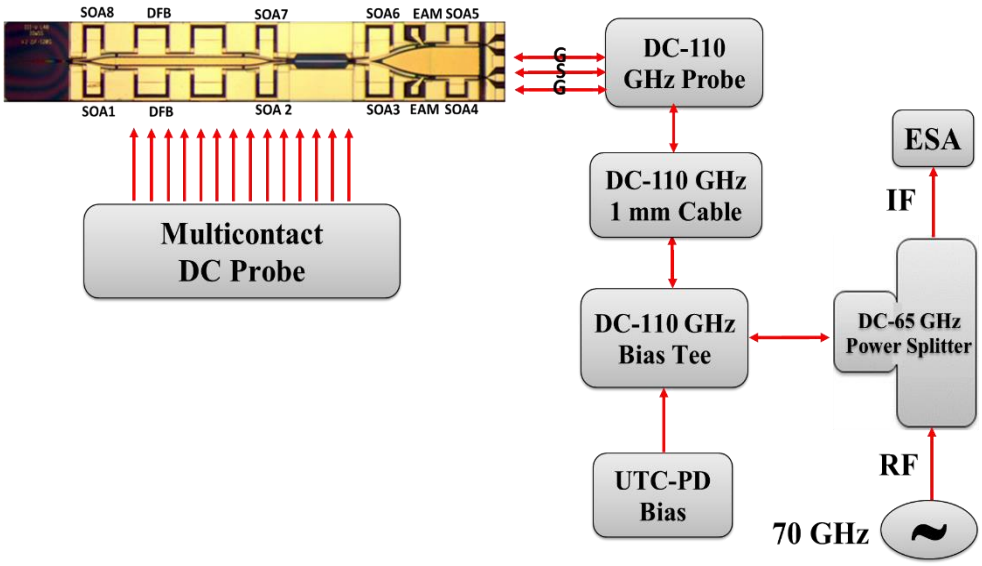

Fig. 4-5: Block diagram of the optically pumped mixing experiment.

The RF signal was generated by a signal synthesizer at 70 GHz and 13 dBm, coupled, using a bias tee, with a UTC-PD voltage bias that is optimum for mixing, and sent to the UTC-PD via a coplanar probe. The optimum biasing voltage was found by sweeping the applied voltage bias while monitoring the power of the IF signal. The optimum voltage bias varied between -1 V and -1.4 V across the IF range, while the photocurrent varied between 3.2 mA and 4.5 mA. These variations are attributed to the change in the optical signal power at the UTC-PD input as the lasers bias currents were tuned. A power splitter was used to allow for the simultaneous supply of the RF to the UTC-PD and the extraction of IF from the UTC-PD.

The RF signal received at the UTC-PD was estimated at -6 dBm. RF power estimation was done based on both measurements and typical insertion losses of the components along the RF path, as given in their datasheets. Table 4- 1 gives a list of these losses in the RF path, which add up to about 19 dB.

Table 4-1: Estimated losses in the RF path.

Component	Losses (dB)	Comments
Synthesizer, v-cable, power splitter, and a connector	13.2	Measurement
1-mm to 1.85 mm adaptor	0.3 at 65 GHz	Datasheet [144]
Bias tee	1	Datasheet [145]
24 cm-long 1 mm cable	3.8	Datasheet [146]
DC-110 GHz probe	0.75	Datasheet
Total	19.05	

Fig. 4-6 shows the electrical spectra after down-conversion in the range from 0.5 GHz to 16.4 GHz, while Fig. 4-7 shows the conversion loss (CL) performance across the IF range. Here, CL is defined as the ratio between the estimated power of the incoming RF signal to the UTC-PD, and the generated IF signal power, at a UTC-PD bias voltage that is optimum for mixing. Fig. 4-7 shows a relatively high conversion loss at 0.5 GHz due to impedance mismatching at this frequency [31]. The CL values presented here are higher than the values reported in [31] because the UTC-PDs on this PIC are optimized for MMW emission rather than mixing.

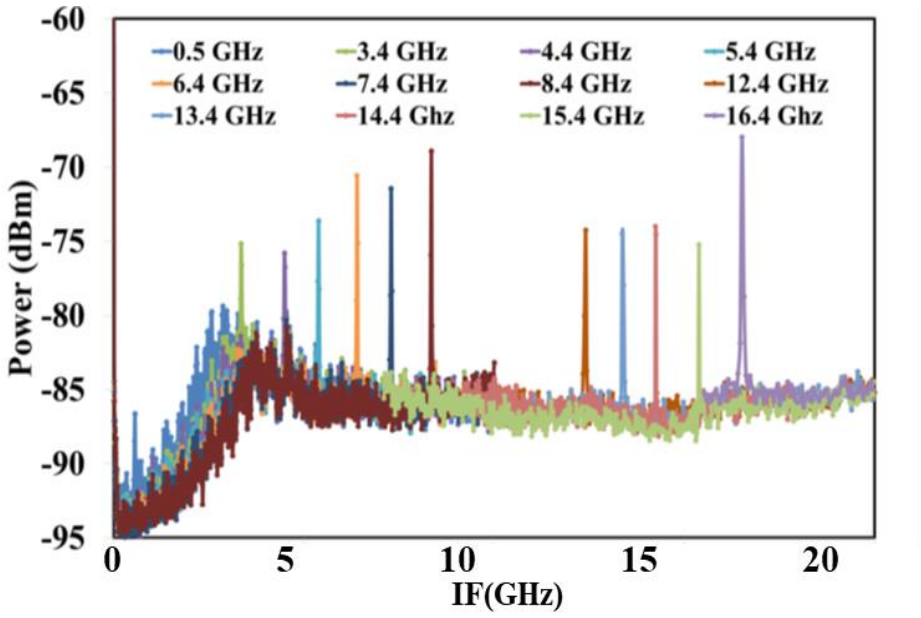

Fig. 4-6: Wide tuneability of IF (RBW = 1 MHz).

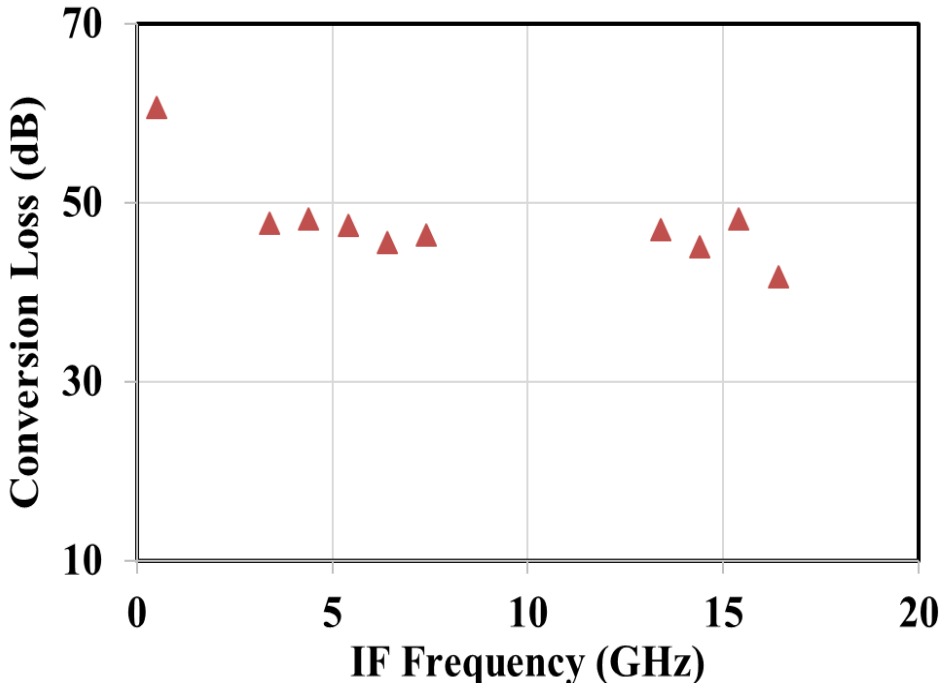

Fig. 4-7: An almost flat conversion loss across a wide IF range.

The figures above do not show results around 10 GHz due to the presence of a signal in that region that interfered with the down-converted IF. Fig. 4-8 below shows an example, where the IF was at 9.4 GHz while the interfering signal was at 10.6 GHz. This could be due to the laser relaxation oscillation at this frequency (DFB lasers can have relaxation oscillation at several GHz) [147] [148].

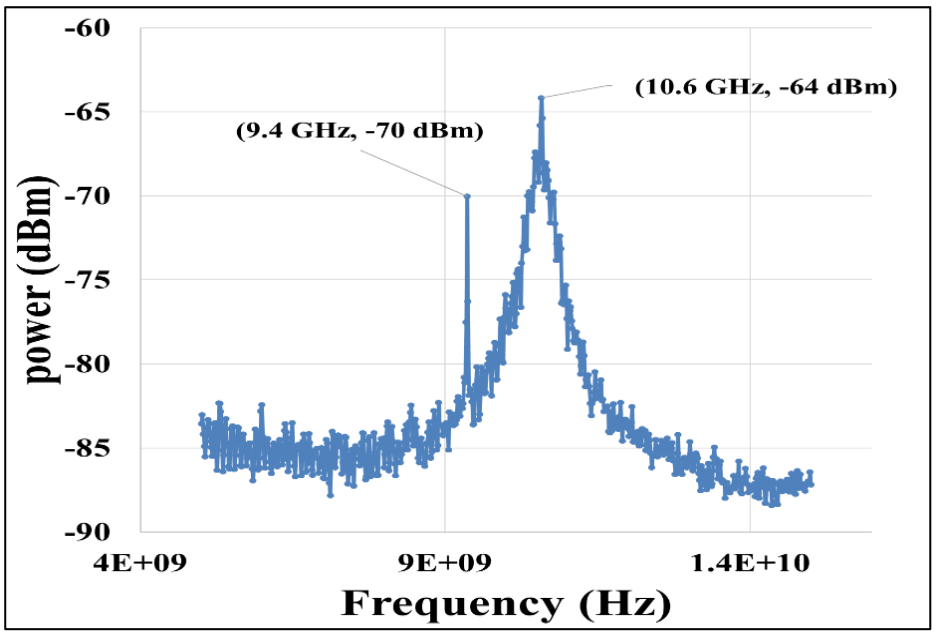

Fig. 4-8: Laser relaxation oscillation interfering with the down-converted IF.

4.2.2 Single Multi-Mode Laser Case

Here, the first laser (DFB1) output was characterized by applying a DC current bias to its gain section while monitoring the optical output of the PIC on an optical spectrum analyser (OSA).

As shown in Fig. 4-9, the applied current was increased from zero to 340 mA. It was observed that DFB1 started lasing at a bias current of 43 mA. It continued its single-mode operation with an increasing bias current up to 76 mA, where a second optical tone was observed. The laser maintained operating in a dual-mode regime up to a bias current of 300 mA. In this regime, the spacing between the two optical tones was around 80 GHz. When the bias current was increased beyond 300 mA a third optical tone was observed, and the spacing between the two main tones was about 52 GHz.

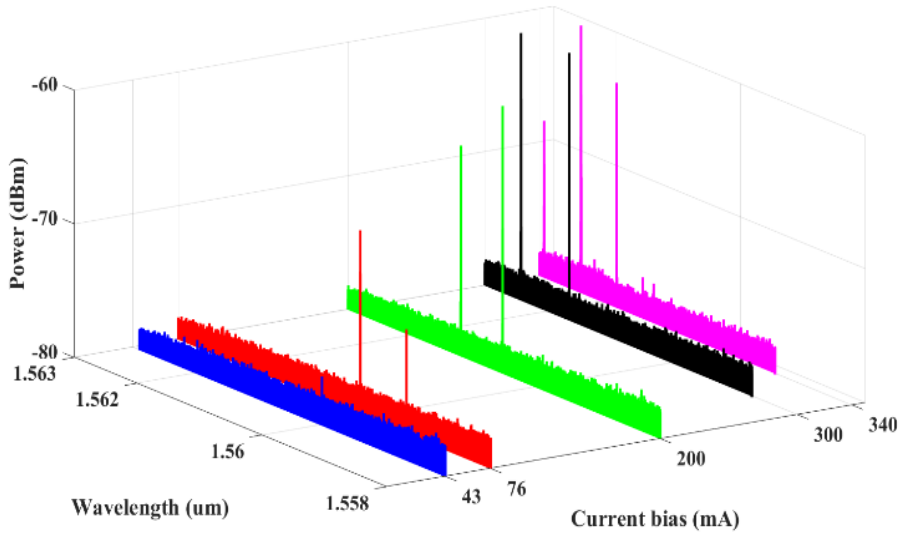

Fig. 4-9: Performance of DFB1 with different DC currents.

After that, the heterodyning experiment shown in Fig. 4-10 was conducted on the first UTC-PD (UTC1) to investigate the capability of the PIC as an MMW emitter. The optical heterodyne was generated by DFB1 in the multi-mode regime. The monitoring SOA (SOA1) was not biased to minimize reflections. The bias current values applied to the other sections are presented in the table in Fig.4-10.

The bias currents were applied through a multi-contact DC probe, while the generated electrical heterodyne signal at 51.0 GHz was extracted by a DC– 65 GHz CPW probe and measured on the ESA. The UTC-PD voltage bias was supplied via a DC-60 GHz bias-tee.

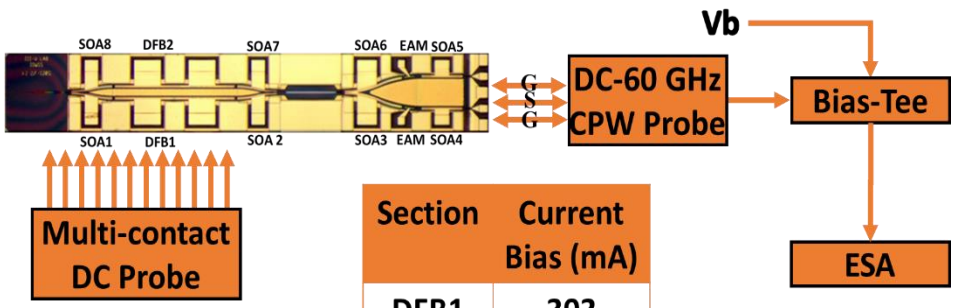

Section	Current Bias (mA)
DFB1	303
SOA2	25.1
SOA3	48.6
SOA4	39
SOA6	45

Fig. 4-10: Block diagram of the optical heterodyning setup.

As shown in Fig. 4-11, the power of the generated electrical heterodyne signal at 51 GHz increased with increasing the negative voltage bias, and the maximum peak power was -28 dBm measured at -4 V, as shown in the electrical spectrum of Fig. 4-12. The other tones seen in the same plot at 56.7 GHz and 61.3 GHz are heterodyning products since the laser was operating in the multimode regime. Small tuneability (of about 1 GHz) of the generated electrical heterodyne signals was observed by applying different set of current bias values to the different sections of the PIC. For instance, in the next experiment the electrical heterodyne signal was at 52 GHz.

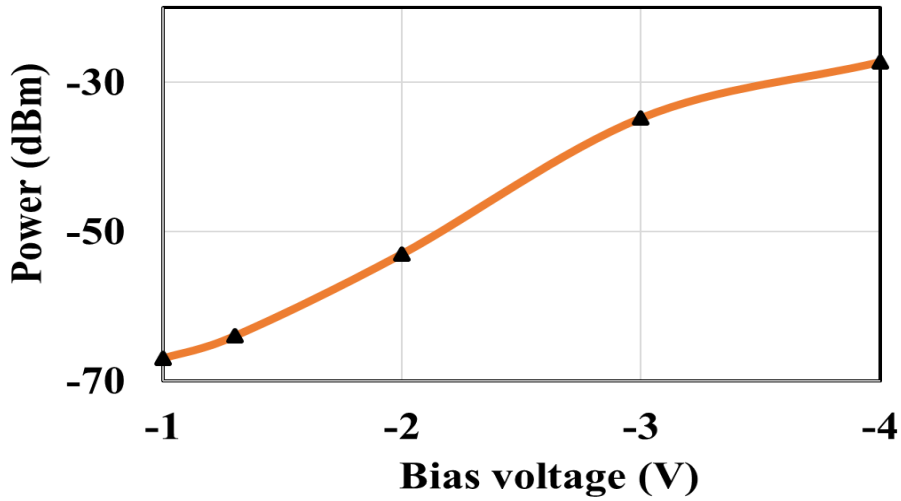

Fig. 4-11: The peak power of the electrical heterodyne as a function of the applied bias voltage.

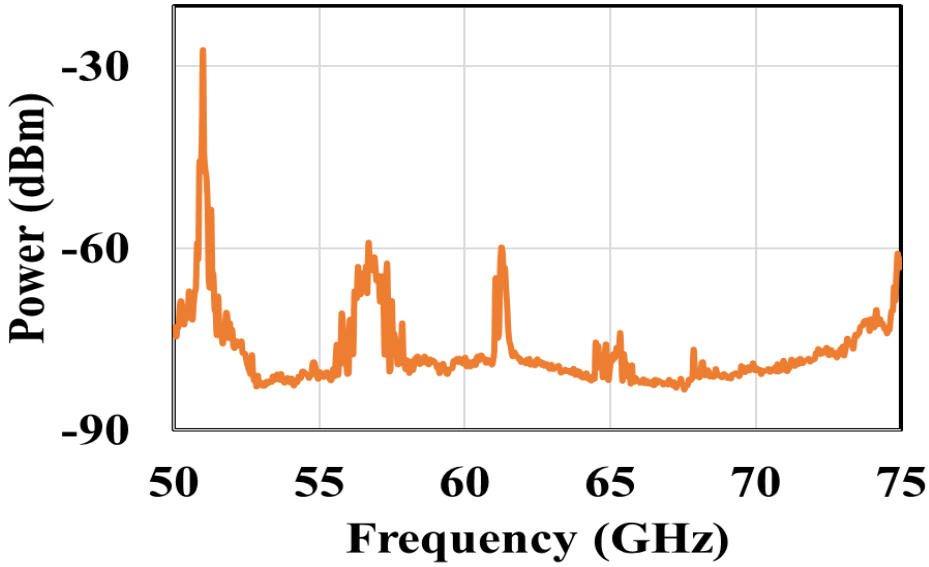

Fig. 4-12: The spectrum of the electrical heterodyne signal at V b= -4 V (RBW = 1 MHz).

The PIC performance in the receiver mode was assessed by conducting an OPM experiment on the same UTC-PD (UTC1), as illustrated in Fig. 4-13. The purpose of this experiment was to measure the efficiency of the UTC-PD in down-converting an incoming high frequency RF signal into a low frequency IF signal.

The table in Fig. 4-13 summarizes the current bias values applied to the different sections on the PIC. In this experiment, the high frequency RF signal was supplied by a signal generator at 64.5 GHz and applied to the UTC-PD through a power divider, a bias-tee, and a CPW probe. The RF power at the input of the probe was measured at -10 dBm. The power divider was used to allow for the

simultaneous supply of the RF signal to the UTC-PD and the extraction of the down-converted IF signal from the UTC-PD.

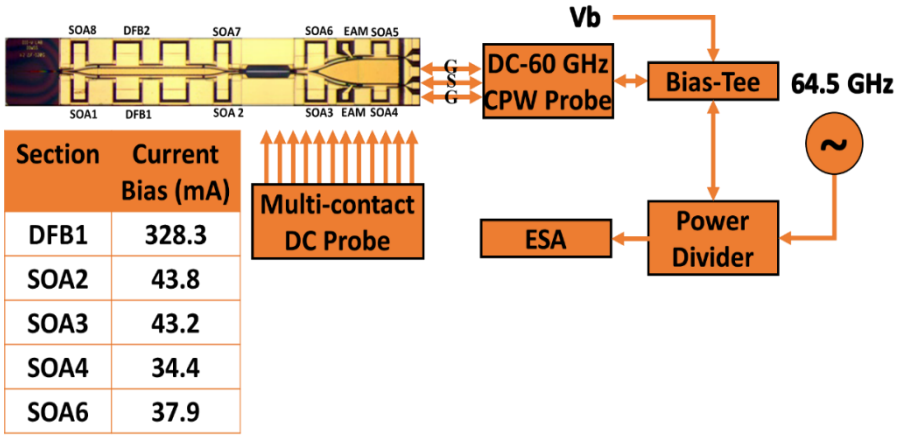

Section	Current Bias (mA)
DFB1	328.3
SOA2	43.8
SOA3	43.2
SOA4	34.4
SOA6	37.9

Fig. 4-13: Block diagram of the opto-electronic mixing experiment.

The conversion loss of the UTC-PD mixer is defined as the ratio between the power of the RF signal and the IF signal both measured at the input of the probe. Previous OPM experiments [31] [149] [150] [151] have shown that conversion loss of the UTC-PD mixer is dependent on the bias voltage applied to it.

Therefore, the conversion loss was measured as a function of the applied bias voltage between zero and -2 V, as shown in Fig. 4-14. The figure also shows previous conversion loss measurements by Rouvalis et al. [31] as a reference. By comparing the two sets of measurements it is evident that lower conversion loss is achieved in this work (28.45 dB) compared to 32 dB in [31]. Further, this is a significant improvement in conversion efficiency compared to the previous mixing experiment on the same PIC, which gives values around 47 dB (Fig. 4-7). This could be attributed to the high optical power that pumped the UTC-PD in this experiment due to the high bias current applied to the laser (around 328 mA) compared to 115 mA in the previous experiment.

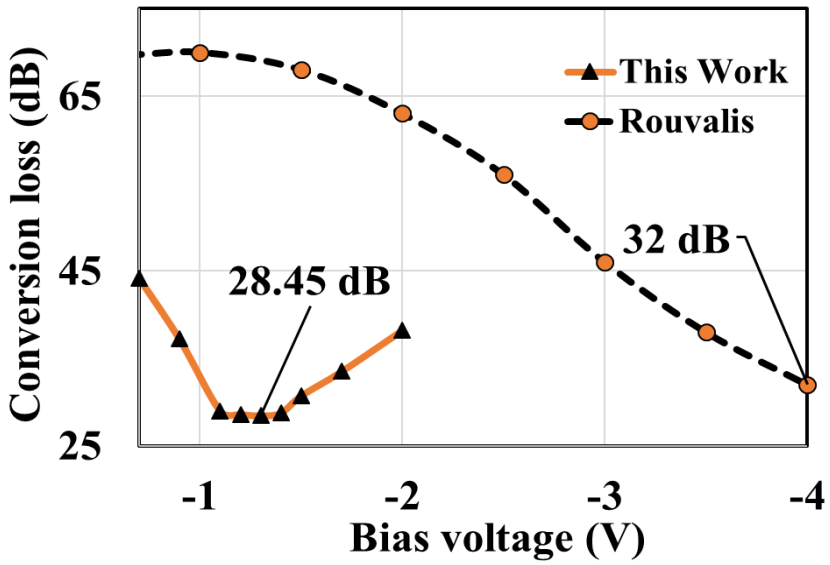

Fig. 4-14: Characterization of the PIC UTC-PD conversion loss in comparison [31].

The electrical spectrum of the down-converted signal at -1.3 V is plotted in Fig. 4-15. The three tones observed in the figure can be explained as follows: The signal at 12.6 GHz is the mixing product of the heterodyne at 51.9 GHz and the RF signal at 64.5 GHz, while the signal at 8.8 GHz is the mixing product of the signal at 55.7 GHz and the RF signal at 64.5 GHz. Finally, the signal at 21.5 GHz is the mixing product of the signals at 8.8 GHz and 12.6 GHz.

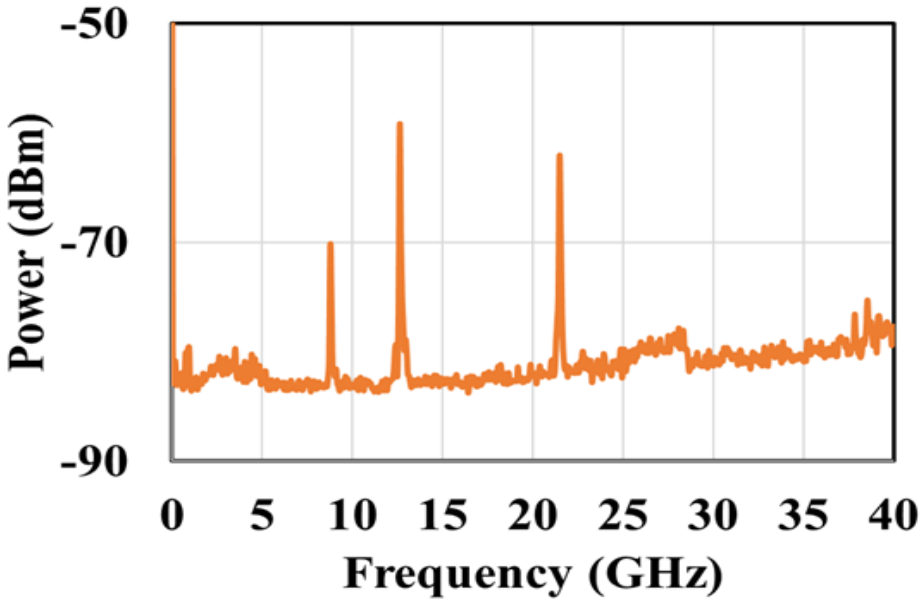

Fig. 4-15: The electrical spectrum of the down-converted signal (RBW = 500 kHz).

4.3 A Photonic Integrated Transceiver

This section presents the results of data transmission and reception experiments using a single UTC-PD that is optically pumped by single laser operating in a multi-mode regime.

4.3.1 Transmitter Mode

The block diagram of the transmission experiment implementing the PIC in the transmitter mode is shown in Fig. 4-16. In this mode, a 1 Gbps OOK data signal at 52.0 GHz was generated by modulating the optical tones from DFB1 using EAM1 and heterodyning them on UTC1. A pattern generator provided the 1 Gbps OOK data signal with 2^{-11} long PRBS. A DC-6 GHz bias-tee was used to couple 1.05 V DC voltage bias to the data signal, after which, both were applied to EAM1 using a DC-60 GHz CPW probe. A multi-contact DC probe was used to apply the current bias to the different sections of the PIC, as shown in the table in Fig. 4-16, and the voltage bias to the UTC-PD (-4 V) was applied using a DC-60 GHz bias-tee.

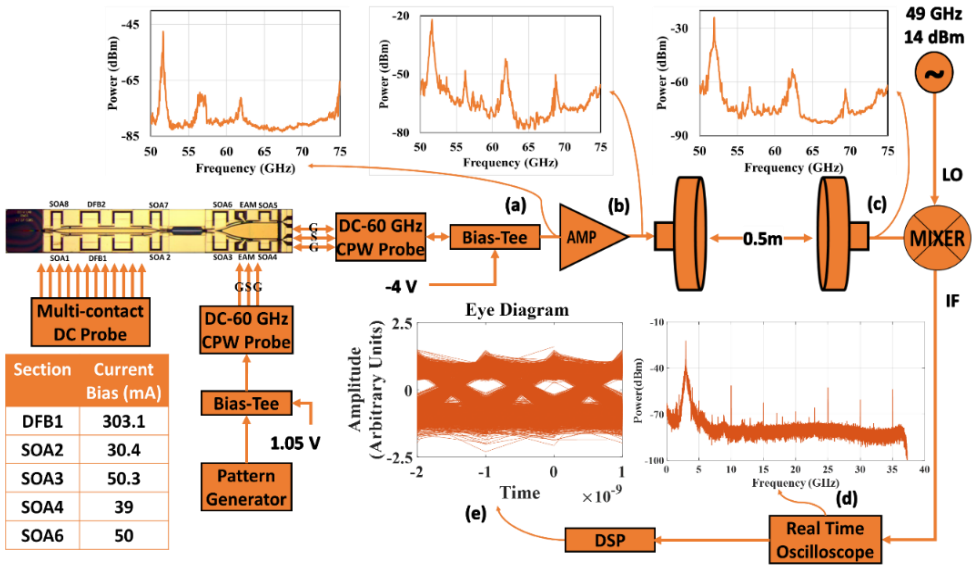

Fig. 4-16: Block diagram of the transmission experiment with a photonic integrated transmitter showing: (a) the spectrum of the generated heterodyne signal (RBW = 1 MHz), (b) the spectrum of the transmitted signal (RBW = 1 MHz), (c) the spectrum of the signal at the receiver antenna (RBW = 1 MHz), (d) the spectrum of the signal after down-conversion to an IF of 3 GHz (RBW = 100 kHz), and (e) the eye-diagram of the recovered data (showing 10,000 bits).

The generated data signal was extracted using a DC – 65 GHz CPW probe and measured on ESA via a 1-m long 60 GHz, as shown in Fig. 4-16-a, giving a peak power of -47.5 dBm. Taking the loss in the cable into account (6 dB) gives -41.5 dBm peak power at the input of the amplifier in Fig. 4-16. The amplifier, which has a gain of 25.5 dB and a NF of 5.7 dB, amplified the signal to the level shown in Fig. 4-16-b. Again, calibrating for the same measurement cable losses gives a signal peak power of -16 dBm at the input of the transmitter antenna, which is of Cassegrain type with 34-dBi gain. The other heterodyne signals at 55.7 GHz and 61.3 GHz are amplified and transmitted because they exist within the frequency range of the amplifier and the antennas. This is clearly observed in the spectra of Fig. 4-16-b and Fig. 4-16-c. The signal was transmitted over a wireless distance of 0.5 m before being detected by identical antenna at the receiver, as shown in Fig. 4-16-c. Taking measurement cables losses into account gives a peak power of -20 dBm at the receiver antenna. This gives 4 dB of FSPL, which is same value obtained by the FSPL equation (eq. (3-1)).

A 65 GHz electronic mixer was used to down-convert the received signal by applying a 49 GHz signal to its LO port. The down-converted signal was captured by the RTO for processing, and the length of the captured waveform was 10 us, which is equivalent to 10,000 bits. The electrical spectrum of the acquired waveform is shown in Fig. 4-16-d, which shows a peak power of -22.5 dBm at 3 GHz. The lines seen in the spectrum are the RTO clock signals and signals picked up from the lab environment.

The same offline DSP steps described in the previous experiments were applied here. The recovered data produced an open eye diagram, as shown in Fig.

4-16-e. The erroneous bits were counted by comparing the transmitted and the received bits and was found to be zero in 10,000-bit long transmissions.

In later experiments, the length of the acquired waveforms was increased to up to 5 ms, which corresponds to 5 million bits. Results showed zero errors in some transmissions, but others were not error free. For instance, 1317 errors were detected in a 5-million-bit long transmission experiment, which corresponds to a BER of 2.6×10^{-4}. This problem of varying BER is discussed in detail in Sec. 4.3.3; it is likely to be due to interfering signals in the lab environment that got picked up by the PIC.

Here, the transmission distance was limited to 0.5 m due to the unavailability of amplifiers in this frequency band. Longer transmission distances are expected when using an amplifier at the receiver.

4.3.2 Receiver Mode

The block diagram of the transmission experiment implementing the PIC in the receiver mode is shown in Fig. 4-17. As shown in the figure, two optical tones were generated by free-running ECLs. The lasers' optical tones were spaced by 0.51 nm, which corresponds to 63.4 GHz. An intensity modulator, biased near the quadrature point (Vb = 6.7 V), was used to modulate one of the optical tones with 500 Mbps data with 2^{-11} bit-long PRBS from a pattern generator. Then, the two tones were coupled using a 3-dB coupler and amplified by an EDFA. The EDFA was followed by an OBPF to reduce the ASE noise. The total power of the optical signal at this stage was 6.3 dBm, and the optical spectrum of the signal is shown in Fig. 4-17-a.

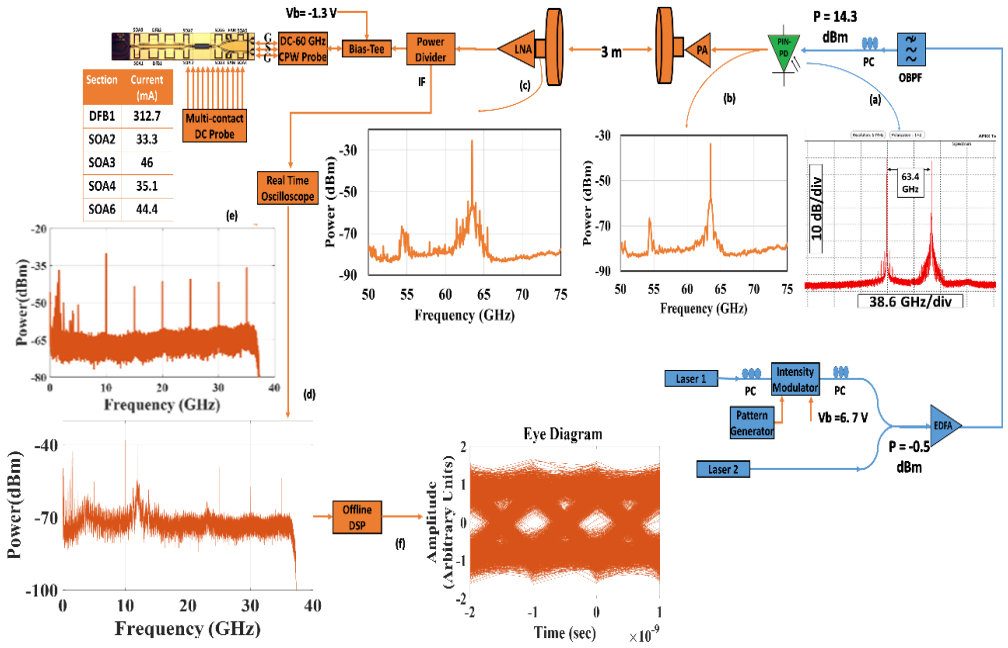

Fig. 4-17: Block diagram of the transmission experiment with a photonic integrated receiver showing: (a) the spectrum of the optical heterodyne signal at transmitter (RBW = 5 MHz), (b) the electrical spectrum of the generated electrical heterodyne signal at the transmitter (RBW = 500 kHz), (c) the electrical spectrum of the signal at the receiver antenna (RBW = 500 kHz), (d) the spectrum of the signal after down-conversion to an IF of 12 GHz (RBW = 100 kHz), (e) the spectrum of the RTO only, without connecting any signal at its input, and (f) the eye-diagram of the recovered data (showing 10,000 bits).

The polarization controllers (PCs) shown in the figure were used to match the polarization states of the two lasers. The optical signal was, then, coupled to a PIN-PD, which generated an electrical heterodyne signal at 63.4 GHz with a peak power of -33.7 dBm, as shown in Fig. 4-17-b. After that, the signal was amplified using a power amplifier, that has a gain of 37 dB and NF of 3 dB, and transmitted wirelessly using a 24 dBi-gain parabolic antenna over a wireless distance of 3 meters before it was detected by an identical antenna at the receiver, as shown in Fig. 4-17-c. As shown in the figure, the peak power of the signal was -25.4 dBm. Considering the measurement cable losses (7 dB) gives -18.4 dBm actual peak power at the input of the amplifier shown in the same figure.

The received signal was amplified by an LNA with gain of 35 dB and NF of 5.7 dB, and fed to the PIC through a DC-60 GHz power divider, a DC-60 GHz

bias-tee and a DC-60 GHz CPW probe. The bias-tee was used to couple the UTC-PD voltage bias to the incoming RF signal.

The current biases to the different sections of the PIC are shown in the table in Fig. 4-17. When the optimum bias voltage was supplied to the UTC-PD (Vb = -1.3 V), it successfully down-converted the data signal into an IF of 12.0 GHz. The down-converted signal, was captured by the RTO for processing, as shown in Fig. 4-17-d. The length of the captured sequence was 20 µs, which corresponds to 10,000 bits. The signals that appear at multiples of 5 GHz are the RTO's clock signals and are not part of the down-converted signal. This is clear in Fig. 4-17-e, which shows the spectrum of the RTO only without any signal at its input.

The same DSP steps described earlier were applied to recover the data signal in this experiment. The number of error bits was zero in a 10,000-bit transmission. The number of erroneous bits was measured by comparing the recovered bit stream to the transmitted bit stream. A relatively open eye diagram of the recovered data was obtained, as shown in Fig. 4-17-f. The eye diagram is not smooth because the CMA code produces only one sample per bit. The transmission experiment was repeated 15 times to improve the accuracy of the BER measurement. In these 15 transmissions, the number of transmitted bits was 150,000 bits, and the total number of detected errors was 58, which corresponds to a BER of 3.8×10^{-4}. Details of these measurements are as follows: zero errors were detected in 11 transmissions, 2 errors were detected in one transmission, 14 errors were detected in 2 transmissions, and finally, 28 errors were detected in one transmission. This variation in error count is likely to be due to interfering signals in the lab environment that got picked up by the PIC. More discussion of this issue is provided in the following section.

4.3.3 Discussion of Results

As discussed in the previous subsections, transmission experiments of the photonic integrated transceiver have achieved BERs of 2.6×10^{-4} and 3.8×10^{-4} for the transmitter mode and the receiver mode, respectively, which is enough for error-free transmission with FEC.

However, when analyzing the results of the previous subsections, it was observed that the measured BER varied, although the received waveforms were acquired consecutively over a short period of time and under the same experimental conditions.

The cause of this behavior was investigated by studying the waveforms of the acquired signals. Fig. 4-18 shows a 5 ms-long waveform of 1 Gbit/s data (5 million-bits) transmitted by the PIC and down-converted to 3 GHz by the electronic mixer at the receiver, and down-converted digitally to the baseband.

By carefully examining the waveform, one can notice an interfering signal added to the data signal. This is clear from spikes that appear at the different parts of the waveform, especially at the center.

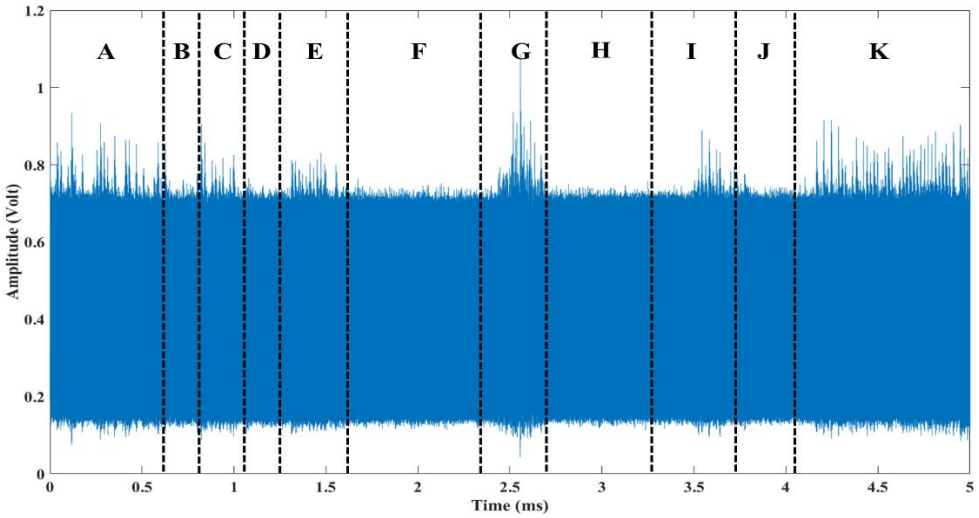

Fig. 4-18: Errors detected in different parts of the received waveform.

To confirm if this is an interference or just a random variation in the signal amplitude, the waveform was divided into smaller chunks and BER was calculated at each of them. BER results are summarized in Table 4-2, where the high BER (BER > 10^{-4}) sections are highlighted in red.

Table 4-2: BER calculations at different sections of the received waveform.

Section	Length (bits)	Errors	BER
A	600,000	142	2.3×10^{-4}
B	160,000	3	1.9×10^{-5}
C	280,000	71	2.5×10^{-4}
D	180,000	zero	zero
E	420,000	37	8.8×10^{-5}
F	710,000	zero	zero
G	300,000	487	1.6×10^{-3}
H	610,000	7	1.1×10^{-5}
I	490,000	27	5.5×10^{-5}
J	270,000	zero	zero
K	980,000	201	2.0×10^{-4}

Notice, from Table 4-2, that the sections with high BER correspond to the areas of high-amplitude spikes in Fig. 4-18. This confirms that errors occurred in bursts and that they are not randomly distributed across the waveform. For instance, the section G at the center of the waveform in Fig. 4-18 above is only 0.3 ms wide, yet, it contains about 487 errors, while section J is 0.28 ms wide and contains zero errors. Fig. 4-19 shows the eye diagrams for section G and section J as an illustration.

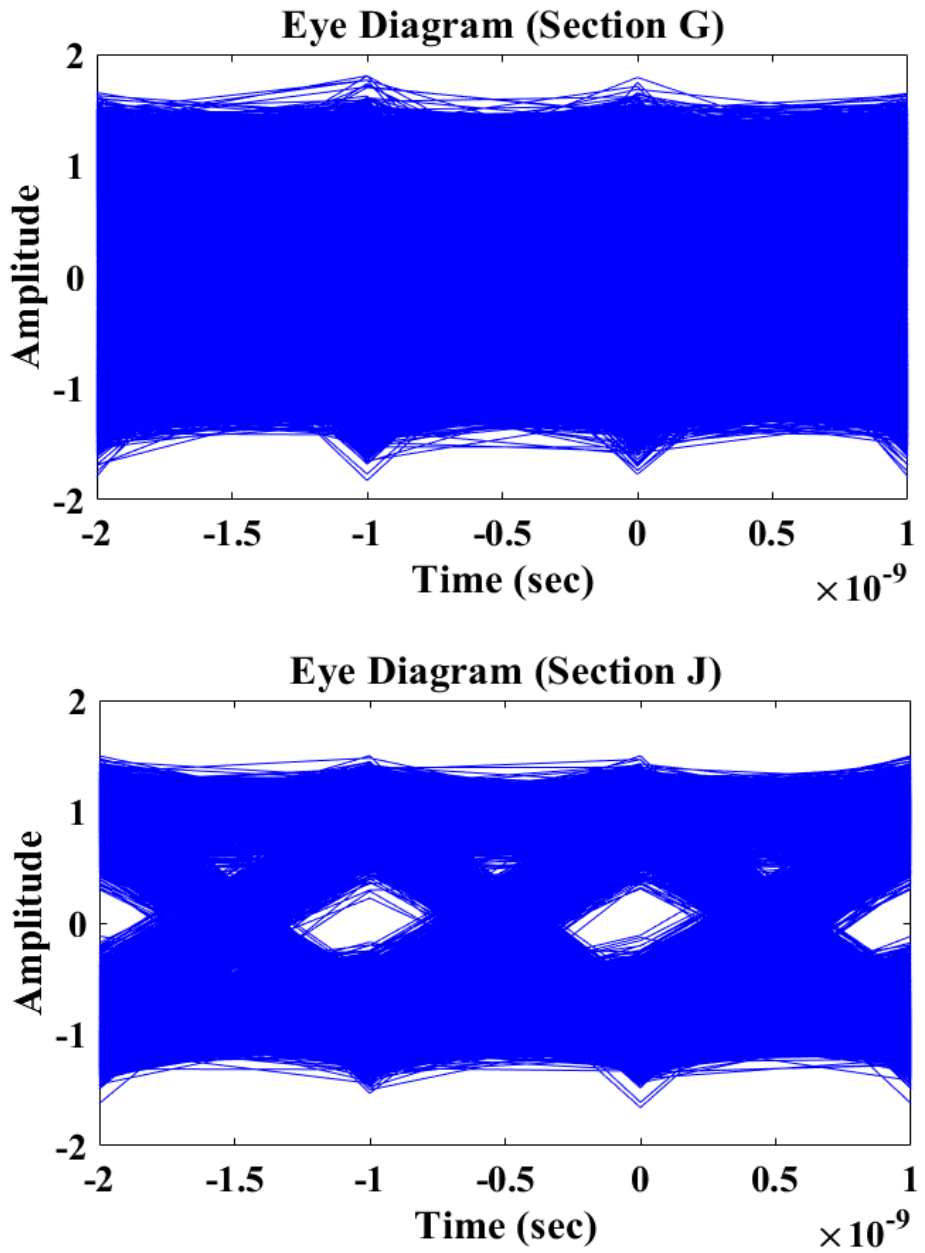

Fig. 4-19: Comparing the eye diagrams in the high and the low interference sections in the acquired waveform.

This led to the suspicion that there might be an interfering signal of bursty nature in the lab environment that gets coupled into the PIC. To verify this claim, a wire (acting like an antenna) was connected to an oscilloscope, and the waveform was saved, and, indeed, a pattern was observed, as shown in Fig. 4-20. The pattern is periodic with a period of 20 μs. and the electrical spectrum of the acquired waveform is plotted in Fig. 4-21.

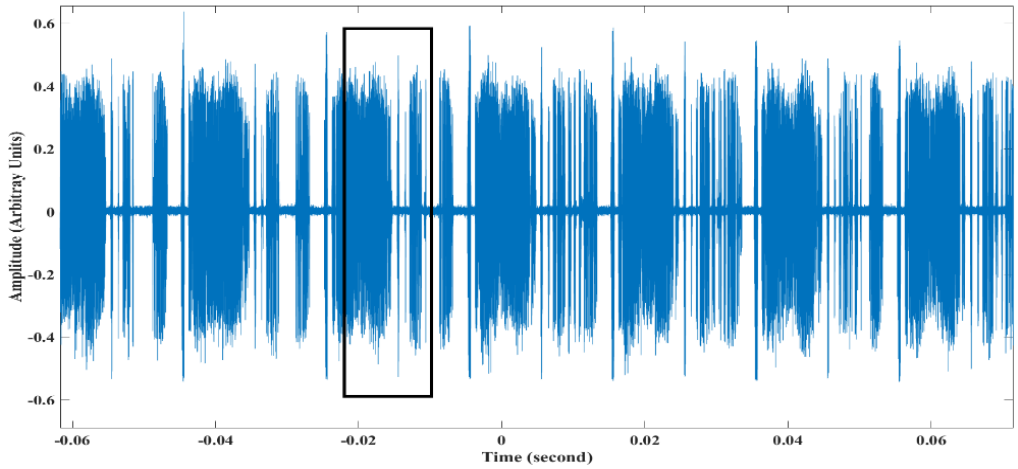

Fig. 4-20: Acquired waveform from the lab environment.

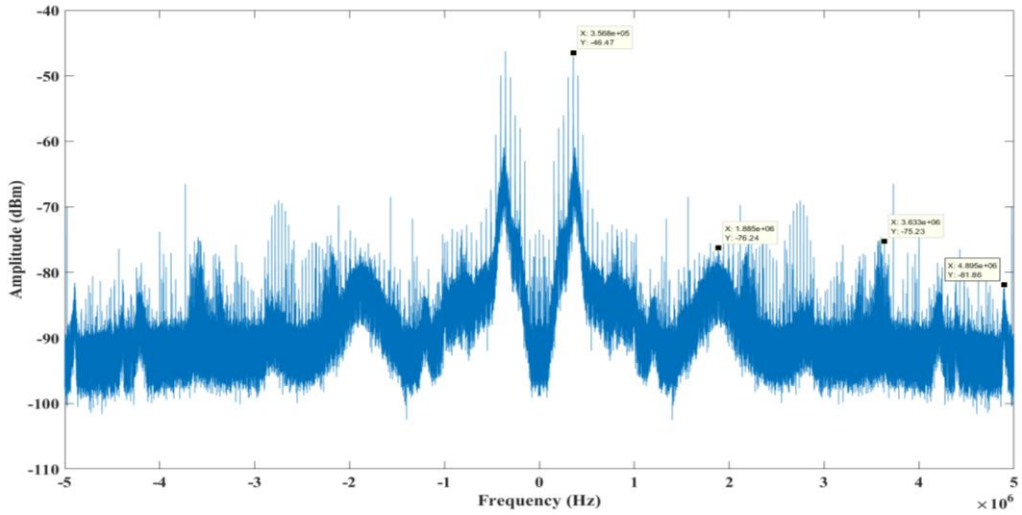

Fig. 4-21: Electrical spectrum of the aacquired waveform from the lab environment.

The electrical spectrum of the acquired waveform shows different signals from DC up to 5 MHz. This frequency range is dedicated to different radio services in the UK, including: aeronautical mobile, maritime mobile, and land mobile [152]. Therefore, it is likely that there is an interference from these services. For example, there is a strong signal at 356 kHz, which falls in the aeronautical radio-navigation band in the UK [152].

So far, it is confirmed that there is an unwanted signal in the lab environment. This interfering signal was studied in detail to better understand its impact on the measured BER. A zoomed-up version of the rectangular area in Fig. 4-20 is shown in Fig. 4-22.

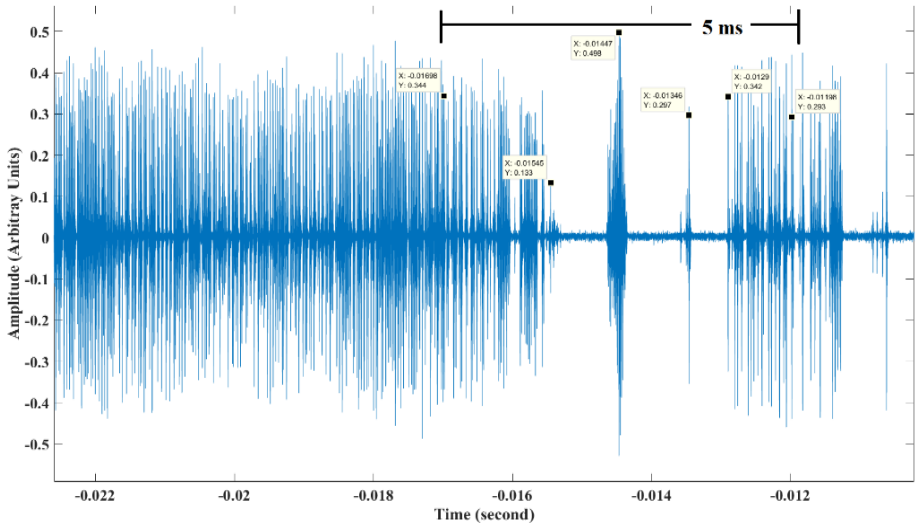

Fig. 4-22: Zoomed-up version of the interference pattern.

It is clear from Fig. 4-20 and Fig. 4-22 above that the interfering signal amplitude varies between null periods and spikes of high amplitude. This might explain the variation in the BERs measured at different time windows. That is, the low BER measurements could correspond to the null periods of the interfering signal, while the high BER measurements could have been taken at the periods of high amplitude in the interfering pattern.

It seems that the interfering signal was coupled into the PIC by a single-pin probe, which was used for grounding the PIC. To verify this, the following experiment was conducted: one of the lasers was biased by the multi-contact DC probe, while the single-pin probe probed the SOA next the laser (In this arrangement, the SOA acted as a photodiode). The output of the single-pin probe was connected to the oscilloscope, which showed the same pattern of Fig. 4-20. This problem was overcome by connecting a low pass filter (LPF) across the ports of the probe. When a capacitor (220 µF) was connected across the ports of the probe, the pattern disappeared. However, the transmission experiment could not be repeated because by the time the interference issue was solved, the laser in the PIC was dead.

Nevertheless, from Table 4-2, one can still evaluate the performance of the PIC in the transmitter mode in the absence of interference, by considering the low interference sections (B, D, E, F, H, I, J) only in BER calculations. In these time periods, the total number of transmitted bits is 2.84 Mbits, while the number of errors is 74. This corresponds to a BER of 2.6×10^{-5}, which below the 3.8×10^{-3} [139] FEC limit for error free transmission.

4.4 Conclusions

This chapter presented a successful demonstration of a photonic integrated MMW transceiver using a UTC-PD that is monolithically integrated with lasers, semiconductor amplifiers, and electro-absorption modulator. In the transmitter mode, the PIC generated 1 Gbps OOK data signal at 52 GHz by utilizing optical heterodyning on a UTC-PD. The generated signal was transmitted over a wireless distance of 0.5 meter and was recovered at the receiver, which implemented an electronic mixer. In the receiver mode, a 63.4 GHz RF signal carrying 0.5 Gbps OOK data was generated by a PIN-PD and transmitted over 3 meters of wireless distance before being detected by the receiver antenna. The receiver utilized optoelectronic mixing on the UTC-PD to down-convert the received signal into a lower IF for processing. The signals in the transmitter and the receiver modes have been successfully recovered and shown zero error bits in 10,000-bit long transmissions.

The transmission experiments were repeated several times to increase BER precision. Results have shown variation in the measured BERs. The cause of these variations was found to be due to an interfering signal in the lab environment, which was coupled into the PIC through a grounding probe. The issue was resolved by connecting a low-pass filter at the input of that probe.

In the transmission mode, the wireless distance was limited to 0.5 m due to the unavailability of amplifiers in this frequency band at the receiver. Longer transmission distances (10s of meters) would be possible when using an LNA at the receiver.

The conversion loss of the UTC-PD optoelectronic mixer reported here was 28.4 dB, which is an improvement compared to previously reported values at 60 GHz [151]. However, it is still high compared to electronic mixers [30], and needs to be improved further to be able to compete with electronic-based receivers.

To the best of the author's knowledge, this is the first demonstration of a photonic integrated transceiver. It offers a small-size and low-cost solution that is integratable with the high-speed fibre networks. Such a transceiver is suitable for short distance communications. Also, it could find interesting applications in 5G and future networks, including HD video streaming, file transfer, and wireless backhaul.

Chapter 5: Hybrid Receivers

5.1 Introduction

Despite the various advantages offered by the UTC-PDs and their successful utilization in wireless receivers, as explained in the previous chapters, the high conversion loss of UTC-PD optoelectronic mixers is still a big limitation to transmitted data rates and the transmission distances.

On the other hand, electronic mixers offer an important advantage, which is the low conversion loss; a conversion loss of about 5 dB has been reported at 180 GHz using a Schottky electronic mixer [30]. However, their need for an electronic LO makes them less attractive.

In conclusion, both electronic and photonic receivers have advantages and limitations. Therefore, it is likely for future networks to have both technologies integrated on single chips to benefit from the advantages offered by each technology.

This chapter reports the results of a study on the feasibility of hybrid integration of electronics and photonics in MMW receivers as an alternative to purely photonic or purely electronic receivers.

In this study, a wireless link was realized, which, implemented a UTC-PD at the transmitter and a photonically-driven electronic mixer at the receiver. A 64.5 GHz signal carrying 1 Gbps OOK data was generated by heterodyning two optical tones into the transmitter UTC-PD. The signal was transmitted using a 24 dBi gain parabolic antenna over a wireless distance of three meters before reaching an identical receiver antenna.

At the receiver, an electronic mixer was used to down-convert the received signal into an intermediate frequency of 12.5 GHz. The LO to the electronic mixer was provided by heterodyne mixing of two optical tones generated using a UTC-PD that is monolithically integrated with semiconductor lasers. The down-

converted signal was acquired by an RTO for offline processing, which showed zero error bits in a 10^5 bit-long transmission.

5.2 Receiver Characterization

This section presents the characterization procedure of the receiver. First, the MMW generation capability of the PIC was investigated to ensure that it can generate an electrical LO signal with enough power at the required frequency. Then, the specifications of the electronic mixer are presented. Finally, the PIC-mixer subsystem was characterized in terms of its conversion loss.

5.2.1 PIC Characterization

In order to assess the performance of the PIC as an LO generator, a heterodyning experiment was conducted on UTC1, as shown in Fig. 5-1. The optical heterodyne was generated by L1 in the multi-mode operation regime. The monitoring SOA (SOA1) was not biased to minimize reflections.

The bias current values applied to the other sections are presented in the table in Fig. 5-1. The bias currents were applied by a multi-contact DC probe, while the generated electrical heterodyne signal was extracted by a DC– 65 GHz CPW probe. A bias-tee was used to couple a DC bias of -2.1 V to the UTC-PD. A 1 m-long DC – 60 GHz cable was used to connect the probe to the ESA.

As shown in the inset of Fig. 5-1, the generated electrical heterodyne signal has a peak power of -21 dBm at 51.9 GHz. Taking the cable and the bias-tee losses into account gives a peak heterodyne power of -10.7 dBm at the input of the probe. The other tones seen in the same plot are heterodyne products of other optical tones generated by the same laser.

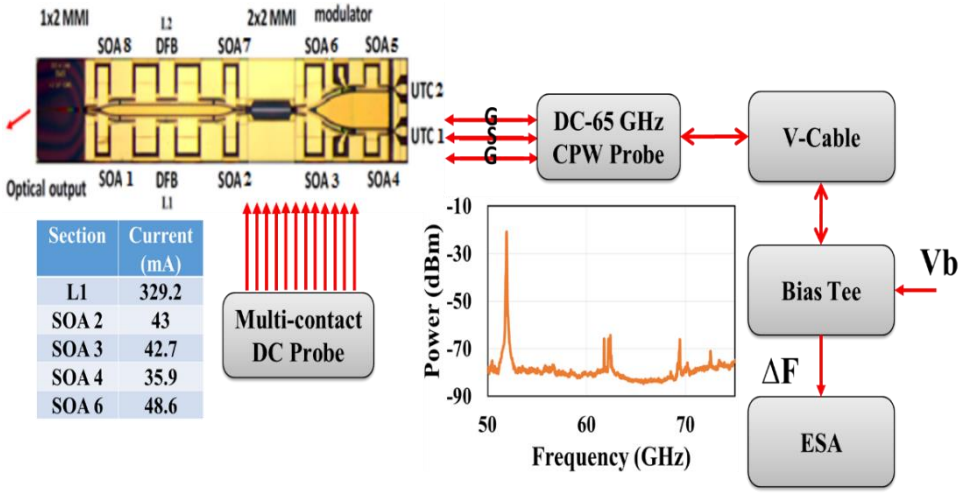

Fig. 5-1: Block diagram of the optical heterodyning setup.

5.2.2 Electronic Mixer Specifications

The mixer used in this experiment is a double balanced electronic mixer from Marki Microwave™ (part no. MM1-2567LS) [153], which operates from 25 GHz to 67 GHz at the LO/RF ports, and from DC to 25 GHz at the IF port.

5.2.3 PIC-Mixer Characterization

Fig. 5-2 shows the block diagram of a mixing experiment that was conducted to characterize the PIC-mixer combination in terms of its conversion loss. The conversion loss is defined as the difference in dB between the power of the RF signal at the input port of the mixer and the power of the IF signal at the IF port of the mixer.

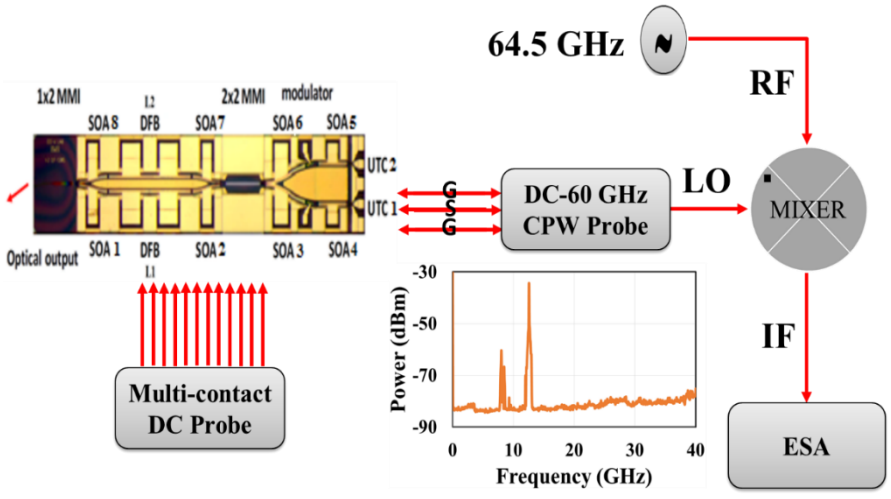

Fig. 5-2: Block diagram of the mixing experiment using the PIC-mixer combination.

A 10 dBm RF signal was generated at 64.5 GHz by a signal generator and applied to the RF port of the mixer via a 1 m-long V-cable, while the electrical heterodyne signal from the PIC, generated at 52 GHz, was applied to the LO port of the mixer. The generated IF signal was, then, measured on the ESA, as shown in the inset of Fig. 5-2. The measured IF signal at 12.5 GHz has a peak power of -34.3 dBm. Taking the measured losses in the RF and IF paths (16 dB and 5.3 dB, respectively), gives a conversion loss of 23 dB for the PIC-driven electronic mixer.

This is slightly lower value than that of the photonically integrated UTC-PD presented in Chapter 4, where 28.5 dB conversion loss was reported. However, it is still high compared to the specifications of the electronic mixer, which give a value of 5 dB when driven by the nominal LO power [153]. The possible cause of this relatively high conversion loss is discussed in Sec. 5.3.3.

5.3 A 60 GHz Hybrid Receiver

Having characterized the PIC-mixer subsystem, this section shows how it can be utilized in a wireless link by implementing it in the receiver of a 64.5 GHz wireless link. A summary of the link parameters is provided in Table 5-1.

Table 5-1: A summary of the experimental parameters in the hybrid receiver experiment.

Parameter	Value
Carrier Frequency	64.5 GHz
Data Rate	1 Gbps
Modulation	OOK
Antennae Gain	24 dBi
Wireless Distance	3 m 4 m (potentially)
FSPL	30 dB
Hybrid Mixer Conversion Loss	23 dB
IF	12.5 GHz
BER	$<10^{-4}$
Real-time/Offline	Offline

5.3.1 Transmitter Setup

At the transmitter, a 1 Gbps OOK data signal was generated at 64.5 GHz by heterodyning two optical tones originating from two ECLs into a 3x10 μm^2 UTC-PD with an epitaxial structure like the one described in [135].

As illustrated in the block diagram of Fig. 5-3, the two optical tones were generated by free-running lasers with 0.52 nm spacing (corresponding to a 64.5 GHz). An MZM, biased at the quadrature point (V_b = 7 V), was used to modulate one of the optical signals with a 1 Gbps data signal from a pattern generator. Then, the two optical tones were coupled using a 3-dB optical coupler and amplified by an EDFA. The EDFA was followed by a 1 nm-wide OBPF to reduce the ASE noise.

The PCs in Fig. 5-3 were used to match the polarization of two optical tones to that of the UTC-PD waveguide to maximize light coupling from the lensed fibre to the UTC-PD. The total power of the optical signal at the input of the lensed fibre was measured by a power meter at 14.3 dBm, while the optical spectrum of the signals at this stage was measured using an OSA, as shown in Fig. 5-3-a.

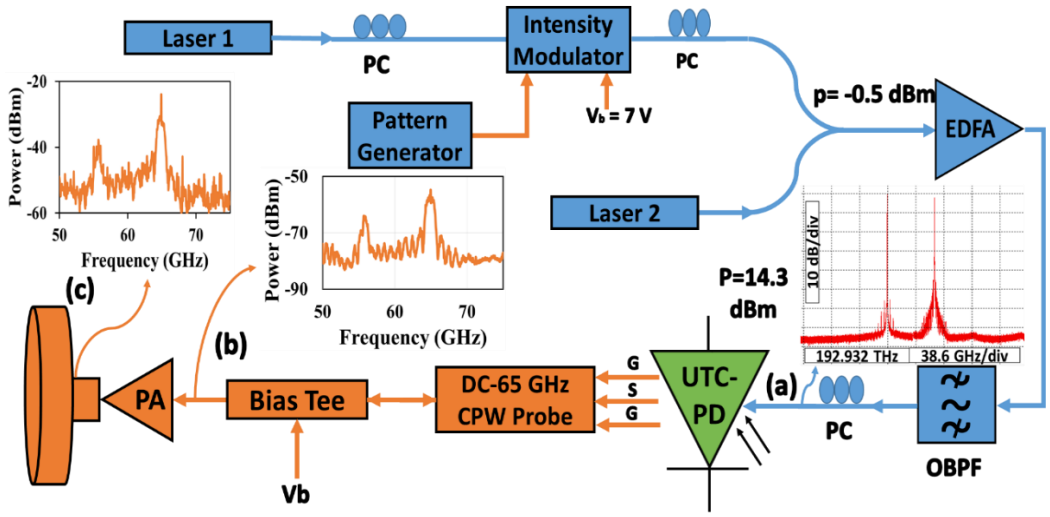

Fig. 5-3: Block diagram of the optical transmitter.

The UTC-PD voltage bias was supplied from a Keithley source/meter at -2.1 V using a bias-tee, while the generated photocurrent was measured at -3.5 mA. A DC-65 GHz CPW probe was used to extract the generated electrical heterodyne signal from the waveguides of the UTC-PD. The extracted electrical heterodyne signal, shown in Fig. 5-3-b, was then amplified with a power amplifier (PA) with gain = 37.9 dB and NF = 4 dB (Fig. 5-3-c). A WR-15 (50 GHz - 75 GHz) variable waveguide attenuator was placed after the PA to control the transmitted signal power. The signal was transmitted using a 24 dBi gain parabolic antenna over a wireless distance of 3 m before reaching an identical antenna at the receiver. The attenuator was set to attenuate the signal by 3 dB, which corresponds to 1.4-fold increase in distance (d_{new} = 4 m). Under these conditions, the FSPL in the link was 30 dB, calculated using eq. (3-1).

5.3.2 Receiver Setup

The block diagram of the receiver is illustrated in Fig. 5-4. It shows the 64.5 GHz 1 Gbps data signal after detection by a 24 dBi gain parabolic antenna (Fig. 5-4-a), after which, it was amplified by an LNA (gain = 31.3 dB, NF = 5.8 dB) as shown in Fig. 5-4-b. An LO at 52 GHz was supplied to the mixer from the PIC, as shown in Fig. 5-4-c.

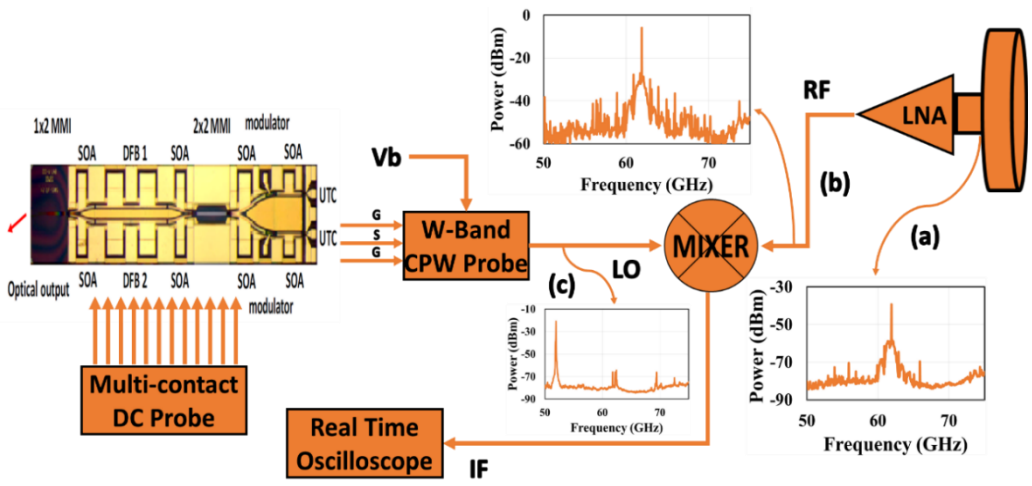

Fig. 5-4: Block diagram of the receiver, which implements a PIC and an electronic mixer.

The PIC-mixer subsystem successfully down-converted the carrier frequency of the received signal into an IF of 12.5 GHz, as shown in Fig. 5-5, after which, it has been captured by an RTO for offline DSP.

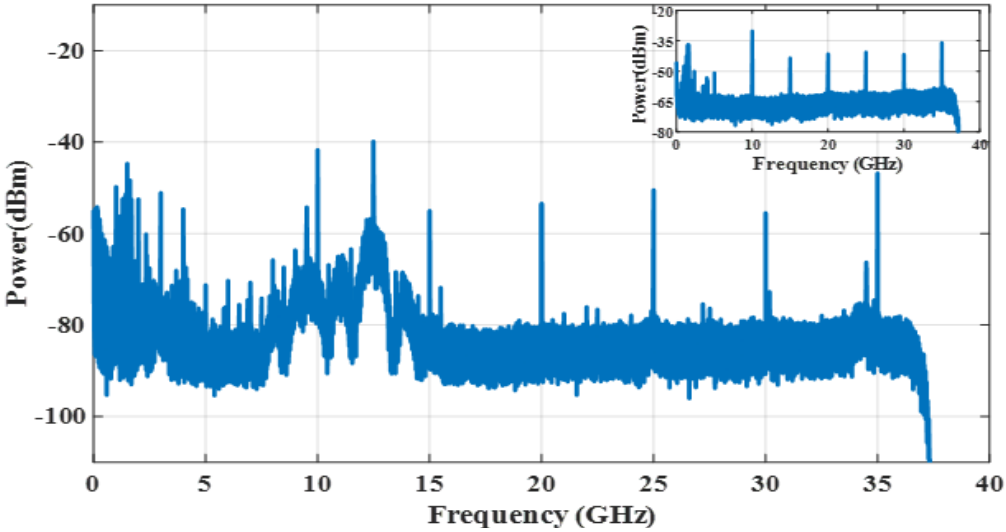

Fig. 5-5: Electrical spectrum of the down-converted IF signal. The inset shows the spectrum of the RTO only, without connecting any signal at its input.

5.3.3 Results and Discussions

The length of the acquired waveform was 100 μs, which corresponds to 10^5 bits. The FFT of the acquired waveform is shown in Fig. 5-5. The lines that appear in the spectrum at multiples of 5 GHz are not part of the down-converted spectrum but are due to the clock signals generated from the RTO. Further, the signals below 5 GHz are also not part of the down-converted spectrum but are signals picked up from the lab environment because they were present even when no input was attached to the RTO channel, as shown in the inset of the same figure, and they were filtered out digitally.

A low-power data signal is observed at 9.5 GHz in the spectrum of Fig. 5-5. This is attributed to another mixing product from a second heterodyne signal since the laser was operating in a three-mode regime. This mixing product did not affect data recovery at 12.5 GHz as it was filtered out digitally.

The same offline DSP steps detailed in the previous chapters were applied here. The number of errors in the received bit stream was calculated by comparing

the transmitted and the received bits, and was found to be zero in 10^5 transmitted bits. Also, the recovered data show a relatively open eye diagram as shown in Fig. 5-6. The eye diagram is not smooth because the CMA equalization algorithm produces only one sample per symbol.

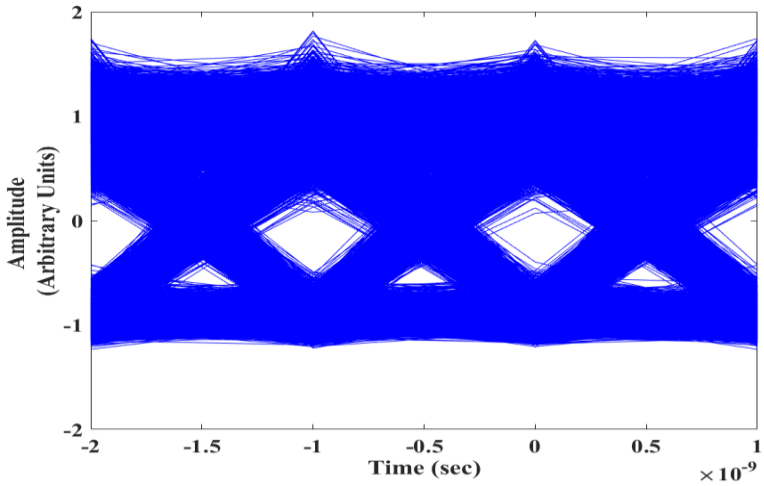

Fig. 5-6: Eye diagram of the recovered signal (showing 10^5 bits).

The specifications of the mixer used in this experiment suggest that it should be driven by about 12 dBm LO for it to work properly and to give a low conversion loss (5 dB) [153]. However, the maximum LO power from the PIC was about -11 dBm, and this caused the conversion loss of the PIC-mixer subsystem to be as high as 23 dB. This was a major limitation to the transmission distance and the data rate. This low LO power from the PIC could be because the PIC laser was operating in a multi-mode regime, which caused the emitted power to be distributed to several frequency tones. Typically, the UTC-PD can provide enough LO power at high frequencies. For instance, output powers of up to 10 dBm from the UTC-PD has been demonstrated at 110 GHz [154] [155]. Therefore, this limitation should be easily overcome in the future demonstrations.

5.4 Conclusions

This chapter demonstrated a 1 Gbps OOK transmission link at 64.5 GHz with a wireless distance of three meters implementing photonic-based system at the transmitter and the photonically driven electronic mixer at the receiver. The UTC-PD at the receiver is monolithically integrated with two DFB lasers and SOAs on a single PIC and was used to provide an electrical LO to drive an electronic mixer. To the best of the author's knowledge, this is the first demonstration of a hybrid receiver of this type.

Transmission distance can be increased to 4 m by removing the 3-dB attenuation at transmitter. The attenuator was introduced due to the laboratory size confinement.

This work shows the viability of hybrid integration of electronics and photonics as an alternative solution to purely electronic or photonic integration, as it combines the advantages of the low conversion losses of electronic mixers, and the wide tuneability and integrability of the photonic components with the high-speed fibre networks.

Chapter 6: Summary and Future Work

6.1 Summary

The UTC-PD is famous for its MMW generation capabilities owing to its high output power and large 3-dB bandwidth. Another important feature of the UTC-PD is its monolithic integrability with other optical components on single photonic chips, which enables photonically integrated MMW transmitters [46]. However, the UTC-PD has not been used in wireless receivers, prior to this PhD work, due to its low efficiency as an optoelectronic mixer, which is an essential component in MMW wireless receivers. Nevertheless, there are scenarios where it would still be advantageous to use the UTC-PD at the receiver, as discussed in Chapter 1 and Chapter 2.

The objective of this PhD project was to investigate the possibility of utilizing the UTC-PD in wireless receivers, as this would enable photonic integrated receivers, and, eventually, photonic integrated transceivers, which would offer the advantages of monolithic integration of photonic components such as the reduction of size and cost as well as the integration with the high-speed optical fibre networks.

The foundation for this PhD work was the concept of optoelectronic mixing in the UTC-PD, demonstrated in [31] and [110]. These demonstrations have shown that the UTC-PD can be used to down-convert a high frequency signal into a lower intermediate frequency, which is crucial for wireless receivers. However, these demonstrations were done within a 100 Hz of detection bandwidth which is not enough for data communications purposes. Further, the down-conversion efficiency reported in these previous works were high. For instance, a conversion loss of 32 dB has been demonstrated at 100 GHz [31].

In the beginning of this research, a UTC-PD was characterized in terms of its conversion loss at 35 GHz. The minimum conversion loss achieved at this

frequency was 22.5 dB, which is a significant improvement compared to previously reported values in [31] although at a lower frequency. The choice of this frequency was due to its significance as a candidate frequency for 5G in many countries [134].

With this encouraging conversion loss value, the UTC-PD mixer was implemented in the receiver of a 5 Gbit/s OOK data transmission link of 1.3 meters wireless distance [149]. At the receiver, data were successfully recovered in real-time and shown an open eye diagram. This was the first demonstration of a UTC-PD-based wireless receiver. However, the UTC-PD required coherent optical signals, which is an added complexity to the receiver design.

Another experiment was designed to prove that the UTC-PD can receive complex data signals while maintaining a simple receiver design [150]. In this experiment, 1 Gbaud QPSK data signal at a carrier frequency of 33.5 GHz was transmitted wirelessly over a distance of 1.4 meters. The receiver implemented a UTC-PD that was pumped by non-coherent optical tones from two free-running lasers, thus, simplifying the receiver design requirements. Here, data were successfully recovered after offline processing.

Later, this work was extended to a carrier frequency of 60 GHz due to the significance of this frequency band to 5G as it contains 7 GHz of unlicensed spectrum. This new experiment implemented UTC-PDs both at the transmitter and the receiver and successfully demonstrated 1 Gbit/s wireless link of potentially 50-meter-long wireless distance [151].

After these successful demonstrations, which used single UTC-PDs and non-integrated optical components, the goal was to move towards integration as it brings reductions in size and cost. A photonic integrated circuit with lasers, optical

amplifiers, modulators and UTC-PDs was used for this purpose. The PIC was successfully implemented in the receiver of a 3 meter-distance 0.5 Gbit/s wireless link in the 60 GHz band. Moreover, the same UTC-PD on the PIC was successfully used as a transmitter of 1 Gbit/s OOK data and, potentially, 10s of meters of wireless distance, thus, demonstrating a photonic integrated transceiver. To the best of the author's knowledge, this is the first photonic integrated transceiver. It could find interesting applications in 5G and future networks.

Finally, the feasibility of electronic-photonic hybrid integration in wireless receivers was examined [156]. In this investigation, a wireless transmission experiment was designed implementing a photonic integrated UTC-PD and an electronic mixer at the receiver. The PIC was used to provide the LO to the mixer. The purpose is to benefit from the advantages offered by both technologies and to overcome their limitations. That is, to eliminate the need for the costly electronic LO while benefiting from the low conversion losses of electronic mixers. This photonic-electronic combination successfully recovered a 1 Gbit/s OOK data signal at a 60 GHz carrier after 3 meters distance of wireless transmission proving that hybrid integration is a viable alternative to photonic only or electronic only integration.

The following table, Table 6.1, highlights some of the achievements of this thesis on utilizing the UTC-PD in wireless receivers and provides a performance comparison with some of the available recently published works on electronic transceivers. Comparison is made between technologies in their receiver mode in the 60 GHz band.

Table 6-1: Performance comparison of different transceiver technologies.

Type	Electronic [157]	Electronic [158]	Photonic (this work)	Photonic (this work)	Hybrid (this work)
Technology	130 nm SiGe	65 nm CMOS	Non-integrated UTC-PD	Integrated UTC-PD	UTC-PD + Schottky
Data rate (Gbit/s)	4.6	3.1	1.0	0.5	1.0
Distance (m)	5.9	1.5	0.5	3	3

It is clear from the table above that electronic transceivers exhibit better performance compared to the photonic and the hybrid alternatives presented in this thesis. Nevertheless, the solutions presented in this work still offer important advantages that are not possible for electronics only solutions to offer, such as: the wide tuneability (70.5 GHz to 92.4 GHz tuning range was reported in Chapter 4), the integrability with the fibre networks in phased array massive MIMO systems for beamforming (Fig. 1-2), the simplification of the network architecture in multicast systems (Fig. 1-3), and the elimination of the need for costly LOs and electrical to optical conversion stages in cellular communication systems (Fig. 2-11). Also, there is a large room for optimization to the work presented in the thesis, as will be shown in the next section, and, therefore, there is large potential for it compete with electronics only solutions in the future.

6.2 Future Work

One of the major limitations to the performance of the systems presented in this thesis is the high conversion loss of the UTC-PD optoelectronic mixer in the receiver. Although the conversion loss values reported here are less than the previously reported values, they are still considered high compared to those of electronic mixers. This could be because these UTC-PDs were originally designed for MMW emission rather than mixing. Therefore, as a future work, it is very important to redesign the epitaxial structure of the UTC-PD to optimize it for optoelectronic mixing purposes, and this would improve the sensitivity of the receiver dramatically allowing for longer transmission distances and higher data rates.

Another major limitation to the systems presented here is the use of a power divider to allow for the simultaneous supply of the RF signal to the UTC-PD and the extraction of the IF signal from the UTC-PD. The problem with this component is that it introduces large losses to both RF and IF signals, and therefore, deteriorates the SNR. Further, it limits the frequency of operation of the receiver since commercially available power dividers operate from DC to only up to 65 GHz. To overcome these limitations, I am planning to redesign the waveguides of the UTC-PD to create separate waveguides for RF supply and IF extraction, thus, eliminating the need for the power divider. This would remove the limitation on the frequency of operation of the receiver, guarantee a complete isolation between the RF and IF paths, and reduce reflections.

My previous experiments have shown a promising trend of decreasing conversion loss of the UTC-PD with increasing optical LO power. The maximum LO power I used in my characterization experiments was 18 dBm limited by the output power of the EDFAs available. That trend of decreasing conversion loss is

expected to continue should higher LO powers be available. Therefore, in my future experiments, I will try to push the optical LO power higher by using more powerful EDFAs in order to achieve lower conversion losses.

Also, I am planning to package some UTC-PDs for my future experiments since this would simplify the experiments and make them more stable and repeatable by eliminating the need for the continuous lensed fibre alignment.

The photonic integrated transceiver presented in Chapter 4 could either send or receive data at a time (half-duplex), but could not perform both functions simultaneously because it utilized a single UTC-PD. Since that PIC comprises two UTC-PDs, I am planning to use one of the UTC-PDs as a transmitter and the other one as a receiver, thus, demonstrating a full-duplex transceiver.

In my previous experiments with PICs, the presence of interference signals in the lab environment affected the BER performance of the communication links. After investigating the origins of the problem, I concluded that it could be due to the incomplete isolation of the PIC (the unwanted signals were coupled to the PIC through the grounding probe). Therefore, to avoid this problem in the future, I am planning to use RF filters for all probes and current sources, and potentially, package the PIC.

In terms of system demonstrations, it is planned to incorporate this PIC in a dual-band wireless link at 300 GHz and 60 GHz, with the PIC being the 60 GHz receiver, thus, emulating a heterogenous network. In this demonstration, and all future demonstrations, I am planning to use more spectral efficient data modulation formats at the transmitter and to optimize the DSP algorithm at the receiver to support higher transmission data rates.

Finally, I am planning to extend this work to the E-band (60 GHz – 90 GHz) because of its huge potential in mobile backhaul as it contains 10 GHz of lightly licensed spectrum [159].

References

[1] K. Balakier et al., "Demonstration of photonic integrated RAU for millimetre-wave gigabit wireless transmission," 2016 IEEE International Topical Meeting on Microwave Photonics (MWP), Long Beach, CA, 2016, pp. 344-347.

[2] The Fiber Optic Assosication, "Guidelines on what loss to expect when testing fiber optic cables," [Online]. Available: http://www.thefoa.org/tech/loss-est.htm. [Accessed: 14-May-2019].

[3] V. Tiwari, “New speed record set under real-world conditions,” SCIENCE XPRESS, 01-Mar-2019. [Online]. Available: https://sciencexpress.org.in/new-speed-record-set-under-real-world-conditions/. [Accessed: 14-May-2019].

[4] K. Miller, “Calculating Optical Fiber Latency,” M2 Optics. [Online]. Available: http://www.m2optics.com/blog/bid/70587/Calculating-Optical-Fiber-Latency. [Accessed: 14-May-2019].

[5] Cisco, "Cisco visual networking index: global mobile data traffic forecast update, 2016–2021 White Paper, " [Online]. Available: http://www.cisco.com/c/en/us/solutions/collateral/service-provider/visual-networking-index-vni/mobile-white-pap.[Accessed: 29-March-2017].

[6] P. Schulz et al., "Latency Critical IoT Applications in 5G: Perspective on the Design of Radio Interface and Network Architecture," in IEEE Communications Magazine, vol. 55, no. 2, pp. 70-78, February 2017.

[7] ITU, "Emerging Trends in 5G/IMT2020, ". [Online]. Available: https://www.itu.int/en/membership/Documents/missions/GVA-mission-briefing-5G-28Sept2016.pdf. [Accessed: 29-March-2017].

[8] ITU-R, "[40] Draft new Report ITU-R M. [IMT-2020.TECH PERF REQ] - Minimum requirements related to technical performance for IMT-2020 radio interface(s)". [Online]. Available: https://www.itu.int/md/R15-SG05-C-0040/en. [Accessed: 23-Feb-2017].

[9] M. Agiwal, A. Roy and N. Saxena, "Next Generation 5G Wireless Networks: A Comprehensive Survey," in IEEE Communications Surveys & Tutorials, vol. 18, no. 3, pp. 1617-1655, 2016.

[10] M. A. Zheng, Z. Q. Zhang, Z. G. Ding, P. Z. Fan, H. C. Li, "Key techniques for 5G wireless communications: Network architecture physical layer and MAC layer perspectives", Sci. China Inf. Sci., vol. 58, no. 4, pp. 1-20, Apr. 2015.

[11] S. M. R. Islam, N. Avazov, O. A. Dobre and K. Kwak, "Power-Domain Non-Orthogonal Multiple Access (NOMA) in 5G Systems: Potentials and Challenges," in IEEE Communications Surveys & Tutorials, vol. 19, no. 2, pp. 721-742, 2017.

[12] E. G. Larsson, L. van der Perr, "Massive MIMO for 5G", IEEE 5G Tech Focus, Vo. 1, no. 1, Mar. 2017.

[13] P.T. Compta, F.H.P. Fitzek, "Network coding is the 5G Key Enabling Technology: effects and strategies to manage heterogeneous packet lengths", Trans. Emerging Tel. Tech. 2015, vol. 26, pp. 46-55.

[14] N. H. Mahmood, M. G. Sarret, G. Berardinelli and P. Mogensen, "Full duplex communications in 5G small cells," 2017 13th International Wireless Communications and Mobile Computing Conference (IWCMC), Valencia, 2017, pp. 1665-1670.

[15] M. N. Tehrani, M. Uysal and H. Yanikomeroglu, "Device-to-device communication in 5G cellular networks: challenges, solutions, and future directions," in IEEE Communications Magazine, vol. 52, no. 5, pp. 86-92, May 2014.

[16] Y. Niu, Y. Li, D. Jin, L. Su, A. V. Vasilakos, "A survey of millimeter wave communications (mmWave) for 5G: Opportunities and challenges", Wireless Netw., vol. 21, no. 8, pp. 1-20, Feb. 2015.

[17] I. F. Akyildiz, P. Wang, S.-C. Lin, "Softair: A software defined networking architecture for 5g wireless systems", Comput. Netw., vol. 85, pp. 1-18, Jul. 2015.

[18] S. Sasipriya and R. Vigneshram, "An overview of cognitive radio in 5G wireless communications," 2016 IEEE International Conference on Computational Intelligence and Computing Research (ICCIC), Chennai, 2016, pp. 1-5.

[19] M. M. Mowla, I. Ahmad, D. Habibi and Q. V. Phung, "A Green Communication Model for 5G Systems," in IEEE Transactions on Green Communications and Networking, vol. 1, no. 3, pp. 264-280, Sept. 2017.

[20] D. Choudhury, "5G wireless and millimetre wave technology evolution: An overview", IEEE MTT-S Int. Microw. Symp. Dig., pp. 1-4, May 2015.

[21] A.-T. Hassanain, S. Preubler, S. Bruckner, J. Schoebel, T. Schneider, "Generation of highly stable millimeterwaves with low phase noise and narrow linewidth", J. IEEE Photon. Technol. Lett., vol. 27, no. 15, pp. 1613-1616, May 2015.

[22] A. L. Swindlehurst, E. Ayanoglu, P. Heydari and F. Capolino, "Millimeter-wave massive MIMO: the next wireless revolution?," in IEEE Communications Magazine, vol. 52, no. 9, pp. 56-62, September 2014.

[23] T. S. Rappaport, F. Gutierrez, E. Ben-Dor, J. N. Murdock, Y. Qiao, J. I. Tamir, "Broadband millimetre-wave propagation measurements and models using adaptive-beam antennas for outdoor urban cellular communications", IEEE Trans. Antennas Propag., vol. 61, no. 4, pp. 1850-1859, April 2013.

[24] A. Riaz, "ITU Structure and preparation on WRC-19 Agenda Items", Pacific Radiocommunication Workshop 2018 (PRW-18). . [Online]. Available: https://www.itu.int/en/ITU-D/Regional-Presence/AsiaPacific/Documents/Events/2018/PRW-18/Presentations/Day%202%20-%20.

[25] B. Bhatia, "WRC-19 Agenda 1.13 Spectrum for 5G–IMT 2020", [Online]. Available: http://www.itu-apt.org/wrc2019/bhatia-5G.pdf. [Accessed: 14-May-2019].

[26] Huawei, "5G Spectrum Public Policy Position", [Online]. Available: http://www-file.huawei.com/-/media/CORPORATE/PDF/public-policy/public_policy_position_5g_spectrum.pdf. [Accessed: 14-May-2019].

[27] J.-S. Rieh, D. Yoon, and J. Yun, “An overview of solid-state electronic sources and detectors for Terahertz imaging,” 12th IEEE International Conference on Solid-State and Integrated Circuit Technology (ICSICT), pp. 1-4, Oct. 2014.

[28] P. Huggard, B. Ellison, P. Shen, N. Gomes, P. Davies, W. Shillue, A. Vaccari, and J. Payne, “Efficient generation of guided millimeter-wave power by photomixing,” IEEE Photonics Technology Letters, vol. 14, no. 2, pp. 197–199, 2002.

[29] M. Tonouchi, "Cutting-edge terahertz technology", Nat. Photon., vol. 1, pp. 97-105, 2007.

[30] S. Khanal, T. Kiuru, M. Hoefle, J. Montero, O. Cojocari, J. Mallat, P. Piironen, A. Räisänen, "Characterization of low-barrier Schottky diodes for millimeter wave mixer applications", 2016 Global Symp. On Millimeter Waves Dig., pp. 1-4, Jun. 2016.

[31] E. Rouvalis, M. J. Fice, C. C. Renaud, A. J. Seeds, "Millimeter-wave optoelectronic mixers based on uni-traveling carrier photodiodes", IEEE Trans. Microw. Theory Tech., vol. 60, no. 3, pp. 686-691, Mar. 2012.

[32] J. A. Nanzer, P. T. Callahan, M. L. Dennis, and T. R. Clark, Jr., “Photonic signal generation for millimetre-wave communications,” Johns Hopkins APL Technical Dig., vol. 30, no. 4, pp. 299-308, Jan. 2012.

[33] A. Papazafeiropoulos, B. Clerckx and T. Ratnarajah, "Mitigation of phase noise in massive MIMO systems: A rate-splitting approach," 2017 IEEE International Conference on Communications (ICC), Paris, 2017, pp. 1-7.

[34] Abdul Ashik Abdul Waheed, "Mitigation of Phase Noise at Millimeter-Wave Frequencies for Wireless Personal Area Network Applications", Master thesis 1911, University of Massachusetts Amherst, Feb 2014.

[35] T. Ninomiya, T. Saito, Y. Ohashi and H. Yatsuka, "60-GHz transceiver for high-speed wireless LAN system," 1996 IEEE MTT-S International Microwave Symposium Digest, San Francisco, CA, USA, 1996, pp. 1171-1174 vol. 2.

[36] B. Bosco, S. Franson, R. Emrick, S. Rockwell and J. Holmes, "A 60 GHz transceiver with multi-gigabit data rate capability," Proceedings. 2004 IEEE Radio and Wireless Conference (IEEE Cat. No.04TH8746), Atlanta, GA, 2004, pp. 135-138.

[37] B. A. Floyd, S. K. Reynolds, U. R. Pfeiffer, T. Zwick, T. Beukema and B. Gaucher, "SiGe bipolar transceiver circuits operating at 60 GHz," in IEEE Journal of Solid-State Circuits, vol. 40, no. 1, pp. 156-167, Jan. 2005.

[38] C. Marcu et al., "A 90 nm CMOS Low-Power 60 GHz Transceiver With Integrated Baseband Circuitry," in IEEE Journal of Solid-State Circuits, vol. 44, no. 12, pp. 3434-3447, Dec. 2009.

[39] K. Okada et al., "A 60-GHz 16QAM/8PSK/QPSK/BPSK Direct-Conversion Transceiver for IEEE802.15.3c," in IEEE Journal of Solid-State Circuits, vol. 46, no. 12, pp. 2988-3004, Dec. 2011.

[40] A. Tomkins et al., "A 60 GHz, 802.11ad/WiGig-Compliant Transceiver for Infrastructure and Mobile Applications in 130 nm SiGe BiCMOS," in IEEE Journal of Solid-State Circuits, vol. 50, no. 10, pp. 2239-2255, Oct. 2015.

[41] R. Wu et al., "Ultra-high-data-rate 60-GHz CMOS transceiver for future radio access network," 2017 IEEE 12th International Conference on ASIC (ASICON), Guiyang, 2017, pp. 1025-1028.

[42] R. -. Braun, G. Grosskopf, D. Rohde and F. Schmidt, "Low-phase-noise millimeter-wave generation at 64 GHz and data transmission using optical sideband injection locking," in IEEE Photonics Technology Letters, vol. 10, no. 5, pp. 728-730, May 1998.

[43] M. Weiß, M. Huchard, A. Stohr, B. Charbonnier, S. Fedderwitz and D. S. Jager, "60-GHz Photonic Millimeter-Wave Link for Short- to Medium-Range Wireless Transmission Up to 12.5 Gb/s," in Journal of Lightwave Technology, vol. 26, no. 15, pp. 2424-2429, Aug.1, 2008.

[44] Z. Jia et al., "Multiband Signal Generation and Dispersion-Tolerant Transmission Based on Photonic Frequency Tripling Technology for 60-GHz Radio-Over-Fiber Systems," in IEEE Photonics Technology Letters, vol. 20, no. 17, pp. 1470-1472, Sept.1, 2008.

[45] M. Weiss, A. Stohr, F. Lecoche and B. Charbonnier, "27 Gbit/s photonic wireless 60 GHz transmission system using 16-QAM OFDM," 2009 International Topical Meeting on Microwave Photonics, Valencia, 2009, pp. 1-3.

[46] F. van Dijk et al., "Wireless data transmission and frequency stabilization with a millimeter-wave photonic integrated circuit," 2015 International Topical Meeting on Microwave Photonics (MWP), Paphos, 2015, pp. 1-4.

[47] J. Capmany, D. Novak, "Microwave photonics combines two worlds", Nat. Photon., vol. 1, no. 6, pp. 319-330, Jun. 2007.

[48] A. Stohr, "Photonic millimetre-wave generation and its applications in high data rate wireless access", Proc. IEEE Top. Meeting Microw. Photon., pp. 7-10, Dec. 2010.

[49] Copper vs. Fiber - Which to Choose?," Multicom. [Online]. Available: https://www.multicominc.com/training/technical-resources/copper-vs-fiber-which-to-choose/. [Accessed: 14-May-2019].

[50] A. Hilt, T. Berceti, I. Frigyes, E. Udvary, T. Marozsák, "Fiber· Dispersion Compensation Techniques in Optical/Wireless Systems", Proc. of MIKON'2002 Conference, vol. 1, pp. 25-36, 20–22 May 2002.

[51] D. Jorgesen and D. Jorgesen, "Marki Microwave Multipliers," Marki Microwave RF & Microwave, 24-Jul-2015. [Online]. Available: https://www.markimicrowave.com/blog/marki-microwave-multipliers/. [Accessed: 14-May-2019].

[52] J. R. Demers, T. M. Goyette, K. B. Ferrio, H. O. Everitt, B. D. Guenther and F. C. De Lucia, "Spectral purity and sources of noise in femtosecond-demodulation terahertz sources driven by Ti:sapphire mode-locked lasers," in IEEE Journal of Quantum Electronics, vol. 37, no. 4, pp. 595-605, April 2001.

[53] G. Liu, J. Jayamon, J. Buckwalter and P. Asbeck, "Frequency doublers with 10.2/5.2 dBm peak power at 100/202 GHz in 45nm SOI CMOS," 2015 IEEE Radio Frequency Integrated Circuits Symposium (RFIC), Phoenix, AZ, pp. 271-274, 2015.

[54] A. Nikpaik, A. H. Masnadi Shirazi, A. Nabavi, S. Mirabbasi and S. Shekhar, "A 219-to-231 GHz Frequency-Multiplier-Based VCO With ~3% Peak DC-to-RF Efficiency in 65-nm CMOS," in IEEE Journal of Solid-State Circuits, vol. 53, no. 2, pp. 389-403, Feb. 2018.

[55] A. Nakamura, J. Nikaido, Y. Aoki, Y. Shirakata and S. Takase, "High-efficiency low-phase-noise 79-GHz Gunn oscillator module," 2015 European Microwave Conference (EuMC), Paris, pp. 403-406, 2015.

[56] T. Maekawa, H. Kanaya, S. Suzuki, M. Asada, "Oscillation up to 1.92 THz in resonant tunneling diode by reduced conduction loss", Appl. Phys. Exp., vol. 9, no. 2, Jan. 2016.

[57] H. Eisele, "Selective etching technology for 94-GHz GaAs IMPATT diodes on diamond heat sinks", Solid State Electron., vol. 32, pp. 253-257, 1989.

[58] H. Eisele, "355 GHz oscillator with GaAs TUNNETT diode," in Electronics Letters, vol. 41, no. 6, pp. 329-331, 17 March 2005.

[59] j. -S. Rieh, D. Yoon, J. Yun, "compact solid state electronics terahertz devices and circuits", in Terahertz Biomedical Science and Technology, CRC/Taylor & Francis Group, 2014, ch. 5, pp. 67 - 92.

[60] T. Maekawa, H. Kanaya, S. Suzuki, M. Asada, "Frequency increase in terahertz oscillation of resonant tunnelling diode up to 1.55 THz by reduced slot-antenna length", Electron. Lett., vol. 50, no. 17, pp. 1214-1216, Aug. 2014.

[61] J. Wang, K. Alharbi, A. Ofiare, "High performance resonant tunnelling diode oscillators for THz applications," IEEE Compound Semi. Integrated Circuit Symp. (CSICS), pp. 1-4, Oct. 2015.

[62] Insight-product co., "Voltage controlled GUNN oscillators" [Online]. Available: www.insight-product.com/vcgunn3.htm. [Accessed: 14-May-2019].

[63] Insight-product co., "60 GHz CW IMPATT DIODES". [Online]. Available: www.insight-product.com/60_ghz.html. [Accessed: 14-May-2019].

[64] A. Nakamura, J.-I. Nikaido, Y. Aoki, Y. Shirakata, and S. Takase, “High-efficiency low-phase-noise 79-GHz Gunn oscillator module,” 2015 European Microwave Conference (EuMC), 2015.

[65] J. Wang, C. Li, E. Wasige, L. Wang, and B. Romeira, “28 GHz MMIC resonant tunnelling diode oscillator of around 1mW output power,” Electronics Letters, vol. 49, no. 13, pp. 816–818, 2013.

[66] W. Zhang, E. Kasper and J. Schulze, "An 82-GHz 14.6-mW Output Power Silicon Impact Ionization Avalanche Transit Time Transmitter With Monolithically Integrated Coplanar Waveguide Patch Antenna," in IEEE Transactions on Microwave Theory and Techniques, vol. 67, no. 1, pp. 308-317, Jan. 2019.

[67] P. Plotka, “Tunnett diode oscillators for mm-wave wideband communication and for terahertz electronics,” Proceedings of the International Conference Mixed Design of Integrated Circuits and System, 2006. MIXDES 2006.

[68] M. Urteaga, R. Pierson, P. Rowell, “130nm InP DHBTs with ft > 0.52 THz and fmax > 1.1 THz,” in Proc. 69th Annu. Device Res. Conf. (DRC), pp. 281–282. Jun. 2011.

[69] W. Yoshida, W. R. Deal, X. B. Mei, M. Lange, Z. Zhou, J. Lee, P. H. Liu, K. Leong, “A Terahertz Capable 25 nm InP HEMT MMIC Process,” CS ManTech Conference, pp. 53 - 56, May 2016.

[70] J. Plouchart, "Applications of SOI technologies to communication", IEEE Compound Semiconduct. Integr. Circuit Symp., pp. 1-4, 2011.

[71] B. Heinemann et al., "SiGe HBT technology with fT/fmaxof 300GHz/500GHz and 2.0 ps CML gate delay," 2010 International Electron Devices Meeting, San Francisco, CA, pp. 30.5.1-30.5.4, 2010.

[72] J. Lee, W. Choi and H. Rücker, "60-GHz voltage-controlled oscillator and frequency divider in 0.25-µm SiGe BiCMOS technology," 2012 International SoC Design Conference (ISOCC), Jeju Island, pp. 65-67, 2012.

[73] Z. Zong, M. Babaie and R. B. Staszewski, "A 60 GHz Frequency Generator Based on a 20 GHz Oscillator and an Implicit Multiplier," in IEEE Journal of Solid-State Circuits, vol. 51, no. 5, pp. 1261-1273, May 2016.

[74] T. Nagatsuma, G. Ducournau, C. C. Renaud, "Advances in terahertz communications accelerated by photonics", Nature Photon., vol. 10, pp. 371-379, May 2016.

[75] T. Nagatsuma, “Photonic Generation of Millimetre Waves and its Applications,” Proc. Opt. Fiber Commun. Conf., pp. OM2B.7, Mar. 2012.

[76] L. Dalton, "Photonic integration improves on current technologies," SPIE Newsroom, 2007, [Online]. Available: http://spie.org/news/0866-photonic-integration-improves-on-current-technologies?%20highlight=x2414&SSO=1. [Accessed: 14-May-2019].

[77] J. E. Bowers and A. Y. Liu, "A comparison of four approaches to photonic integration," 2017 Optical Fiber Communications Conference and Exhibition (OFC), Los Angeles, CA, pp. 1-3, 2017.

[78] K. E. Razavi, P. A. Davies, "Millimetre wave generation by filtering the FM-IM spectra of a directly modulated DFB laser", Proc. IEEE MTT-S Int. Microw. Symp. Dig., vol. 3, pp. 1707-1708, Jun. 1997.

[79] J. Yu, Z. Jia, L. Xu, L. Chen, T. Wang, G. K. Chang, "DWDM optical millimeter-wave generation for radio-over-fiber using an optical phase modulator and an optical interleaver", IEEE Photon. Technol. Lett., vol. 18, no. 13, pp. 1418-1420, Jul. 2006.

[80] T. Kuri, K. Kitayama, "Long-term stabilized millimeter-wave generation using a high-power mode-locked laser diode module", IEEE Trans. Microw Technol., vol. 47, no. 5, pp. 570-574, May 1999.

[81] T. Wang, M. Chen, H. Chen, S. Xie, "Millimeter-wave signal generation using four-wave mixing effect in SOA", in Proceedings of the OFC, Mar. 2007.

[82] J. H. Seo, Y. K. Seo, W. Y. Choi, "Nonlinear characteristics of an SOA photonic frequency up-converter", Proc. Int. Top. Meeting Microw. Photon., pp. 109-112, Sep. 2003.

[83] H.-J. Song, J.-S. Lee, J.-I. Song, "Signal up-conversion by using a cross-phase-modulation in all-optical SOA-MZI wavelength converter", IEEE Photon. Technol. Lett., vol. 16, no. 2, pp. 593-595, Feb. 2004.

[84] R. Mohamad, S.M. Idrus, A.S. Supaat, S. Yaakob, A.K. Zamzuri, S.N.A. Sukito, “Millimeter wave carrier generation based on Brillouin fiber laser with improved tuning capability”, Optik, vol. 125, no. 1, pp. 205-207, Jan. 2014.

[85] Z. Jia, J. Yu, G. Ellinas, and G.-K. Chang, “Key Enabling Technologies for Optical–Wireless Networks: Optical Millimeter-Wave Generation, Wavelength Reuse, and Architecture,” Journal of Lightwave Technology, vol. 25, no. 11, pp. 3452–3471, 2007.

[86] S. E. Alavi, M. R. K. Soltanian, I. S. Amiri, M. Khalily, A. S. M. Supa'at, H. Ahmad, "Towards 5G: A photonic based millimeter wave signal generation for applying in 5G access fronthaul", Sci. Rep., vol. 6, Jan. 2016.

[87] T. Schneider, M. Junker, D. Hannover, "Generation of millimetre-wave signals by stimulated Brillouin scattering for radio over fibre systems", Electron. Lett., vol. 40, no. 23, pp. 1500-1501, Nov. 2004.

[88] D. Asderah , “photonic based techniques for millimeter wave generation transmission and multiplexing”, University of Denver , Jan. 2009.

[89] J. Ma, X. Xin, J. Yu, C. Yu, K. Wang, H. Huang, L. Rao, "Optical millimeter wave generated by octupling the frequency of the local oscillator", J. Opt. Netw., vol. 7, no. 10, pp. 837-845, Oct. 2008.

[90] G. Danion, C. Hamel, L. Frein, F. Bondu, G. Loas, M. Alouini, "Dual frequency laser with two continuously and widely tunable frequencies for optical referencing of GHz to THz beat notes", Opt. Exp., vol. 22, no. 15, pp. 17673-17678, 2014.

[91] G. Carpintero, R. C. Guzmán, C. Gordón, G. Kervella, M. Chitoui, F. Van Dijk, "Photonic integrated circuits for radio-frequency signal generation", J. Lightw. Technol., vol. 34, no. 2, pp. 508-515, Jan. 2016.

[92] P. D. Maycock, "Thermal conductivity of silicon germanium III-V compounds and III—V alloys", Solid-State Electron., vol. 10, pp. 161-168, 1967.

[93] J. E. Bowers, J. T. Bovington, A. Y. Liu and A. C. Gossard, "A path to 300 mm hybrid silicon photonic integrated circuits," OFC 2014, San Francisco, CA, pp. 1-3, 2014.

[94] N. A. Estep, J. C. Petrosky, J. W. McClory, Y. Kim, A. J. Terzuoli, "Electromagnetic Interference and Ionizing Radiation Effects on CMOS Devices", IEEE Transactions on Plasma Science, vol. 40, no. 6, pp. 1495-1501, June 2012.

[95] E. Rouvalis, C. Renaud, A. Seeds, "Ultra-Fast Photodiodes for Terahertz Generation", [Online]. Available: https://www.researchgate.net/publication/228879969_Ultra-Fast_Photodiodes_for_Terahertz_Generation. [Accessed: 14-May-2019].

[96] H. Ito, T. Furata, S. Kodama, T. Ishibashi, "InP/InGaAs uni-travelling-carrier photodiode with 310 GHz bandwidth", Electron. Lett., vol. 36, no. 21, pp. 1809-1810, Oct. 2000.

[97] C. C. Renaud, M. Robertson, D. Rogers, R. Firth, P. J. Cannard, R. Moore, A. J. Seeds, "A high responsivity broadband waveguide uni-travelling carrier photodiode", Proc. SPIE, vol. 6194, pp. 61940C, 2006.

[98] Efthymios Rouvalis. PhD thesis, University College London, 2011.

[99] M. Martin, E.R. Brown, "Critical comparison of GaAs and InGaAs THz photoconductors", Terahertz Technology and Applications V Pcoc to SPIE, pp. 826102-826102, Mar. 2012.

[100] A. F. Olvera, H. Lu, A. Gossard, and S. Preu, "Continuous-wave 1550 nm operated terahertz system using ErAs: In(Al)GaAs photo-conductors with 52 dB dynamic range at 1 THz," Optics Express, vol. 25, no. 23, pp. 29492–29500, 2017.

[101] T. Nagatsuma, S. Horiguchi, Y. Minamikata, Y. Yoshimizu, S. Hisatake, S. Kuwano, N. Yoshimoto, J. Terada, H. Takahashi, "Terahertz wireless communications based on photonics technologies", Opt. Exp., vol. 21, no. 20, pp. 23736, 2013.

[102] G. Breed, "The mathematics of mixers: basic principles," [Online]. Available: http://www.highfrequencyelectronics.com/Archives/Jan11/HFE0111_Tutorial.pdf [Accessed: 2-Aug-2018].

[103] G. Seniutinas, G. Gervinskas, E. Constable, A. Krotkus, G. Molis, G. Valušis, R. A. Lewis, and S. Juodkazis, "THz photomixer with a 40nm-wide nanoelectrode gap on low-temperature grown GaAs," Proc. SPIE, vol. 8923, pp.1-9, Dec. 2013.

[104] A. Karpov, D. Miller, F. Rice, J. A. Stern, B. Bumble, H. G. LeDuc, J. Zmuidzinas, "Low noise 1 THz–1.4 THz mixers using Nb/Al-AlN/NbTiN SIS junctions", IEEE Trans. Appl. Supercond., vol. 17, no. 2, pp. 343-346, Jun. 2007.

[105] W. Zhang, P. Khosropanah, J. R. Gao, E. L. Kollberg, K. S. Yngvesson, T. Bansal, R. Barends, T. M. Klapwijk, "Quantum noise in a terahertz hot electron bolometer mixer", Appl. Phys. Lett., vol. 96, pp. 111113, 2010.

[106] S.-M. Chen, Y.-K. Fang, F.R. Juang, W.-K. Yeh, C.-P. Chao, and H.-C. Tseng, "Terahertz Schottky barrier diodes with various isolation designs for advanced radio frequency applications", Thin Solid Films, vol. 519, no. 1, pp. 471–474, Oct. 2010.

[107] S. Khanal, T. Kiuru, M. Hoefle, "Characterization of low-barrier Schottky diodes for millimeter wave mixer applications", 2016 Global Symp. On Millimeter Waves Dig., pp. 1-4, Jun. 2016.

[108] J. Treuttel et al., "A 520–620-GHz Schottky Receiver Front-End for Planetary Science and Remote Sensing With 1070 K–1500 K DSB Noise Temperature at Room Temperature," in IEEE Transactions on Terahertz Science and Technology, vol. 6, no. 1, pp. 148-155, Jan. 2016.

[109] M. J. Fice, E. Rouvalis, L. Ponnampalam, C. C. Renaud, A. J. Seeds, "Telecommunications technology-based terahertz sources", Electron. Lett., vol. 460, pp. 28-31, Dec. 2010.

[110] C. C. Renaud, M. J. Fice, L. Ponnampalam, M. Natrella, C. Graham, and A. J. Seeds, "Uni-travelling carrier photodetectors as THz detectors and emitters," Proc. SPIE, vol. 9370, pp. 1-9, Feb. 2015.

[111] C. C. Renaud, M. Robertson, D. Rogers, R. Firth, P. J. Cannard, R. Moore, A. J. Seeds, "A high responsivity broadband waveguide uni-travelling carrier photodiode", Proc. SPIE, vol. 6194, pp. 61940C, 2006.

[112] H. Ito, S. Kodama, Y. Muramoto, T. Furata, T. Nagatsuma, T. Ishibashi, "High-speed and high-output InP-InGaAs unitravelling-carrier photodiodes", IEEE J. Sel. Topics Quantum Electron., vol. 10, no. 4, pp. 709-727, Apr. 2004.

[113] Farran Technology, "Balanced Mixers 40 – 60 GHz – BMC-19". [Online]. Available: www.hxi.com/Datasheets/40 - 60 GHz Balanced Mixer, BMC-19.pdf. . [Accessed: 14-May-2019].

[114] J. Bowers, "Heterogeneous silicon III–V Photonic Integrated Circuits," 2015 Optical Fiber Communications Conference and Exhibition (OFC), Los Angeles, CA, pp. 1-50, 2015.

[115] N. Ishihara, S. Amakawa, and K. Masu, "RF CMOS Integrated Circuit: History, Current Status and Future Prospects," IEICE Transactions on Fundamentals of Electronics, Communications and Computer Sciences, vol. E94.A, no. 2, pp. 556–567, 2011.

[116] J. E. Bowers, T. Komljenovic, J. Hulme, M. Davenport and C. Zhang, "Integrated photonics for MWP," 2016 IEEE Photonics Conference (IPC), Waikoloa, HI, 2016, pp. 1-2.

[117] T. Komljenovic et al., "Heterogeneous silicon photonic integrated circuits", J. Lightw. Technol., vol. 34, no. 1, pp. 20-35, Jan. 2016.

[118] L. Chen, A. Sohdi, J. E. Bowers, L. Theogarajan, J. Roth, and G. Fish,"Electronic and photonic integrated circuits for fast data center optical circuit switches," IEEE Commun. Mag., vol. 51, no. 9, pp. 53–59, Sep. 2013.

[119] L. Wei, R. Q. Hu, Y. Qian, G. Wu, "Key elements to enable millimetre wave communications for 5G wireless systems", Wireless Commun., vol. 21, no. 6, pp. 136-143, Dec. 2014.

[120] A. Asadi, Q. Wang and V. Mancuso, "A Survey on Device-to-Device Communication in Cellular Networks," in IEEE Communications Surveys & Tutorials, vol. 16, no. 4, pp. 1801-1819, 2014.

[121] M. Ali et al., "Smart Heterogeneous Networks: A 5G Paradigm" in Telecommun. Systems, Springer, 2017.

[122] C. Sacchi, T. F. Rahman, I. A. Hemadeh and M. El-Hajjar, "Millimeter-Wave Transmission for Small-Cell Backhaul in Dense Urban Environment: a Solution Based on MIMO-OFDM and Space-Time Shift Keying (STSK)," in IEEE Access, vol. 5, pp. 4000-4017, 2017.

[123] M. N. Tehrani, M. Uysal and H. Yanikomeroglu, "Device-to-device communication in 5G cellular networks: challenges, solutions, and future directions," in IEEE Communications Magazine, vol. 52, no. 5, pp. 86-92, May 2014.

[124] M. A. Zheng, Z. Q. Zhang, Z. G. Ding, P. Z. Fan, H. C. Li, "Key techniques for 5G wireless communications: Network architecture physical layer and MAC layer perspectives", Sci. China Inf. Sci., vol. 58, no. 4, pp. 1-20, Apr. 2015.

[125] S. Mumtaz, K. M. Saidul Huq and J. Rodriguez, "Direct mobile-to-mobile communication: Paradigm for 5G," in IEEE Wireless Communications, vol. 21, no. 5, pp. 14-23, October 2014.

[126] D. Feng, L. Lu, Y. Yuan-Wu, G. Y. Li, S. Li and G. Feng, "Device-to-device communications in cellular networks," in IEEE Communications Magazine, vol. 52, no. 4, pp. 49-55, April 2014.

[127] F. Han, S. Zhao, L. Zhang and J. Wu, "Survey of Strategies for Switching Off Base Stations in Heterogeneous Networks for Greener 5G Systems," in IEEE Access, vol. 4, pp. 4959-4973, 2016.

[128] Y. Kishiyama, A. Benjebbour, T. Nakamura, and H. Ishii, "Future steps of LTE-A: Evolution toward integration of local area and wide area systems," IEEE Wireless Commun., vol. 20, no. 1, pp. 12–18, Feb. 2013.

[129] C. Sacchi, T. F. Rahman, I. A. Hemadeh and M. El-Hajjar, "Millimeter-Wave Transmission for Small-Cell Backhaul in Dense Urban Environment: a Solution Based on MIMO-OFDM and Space-Time Shift Keying (STSK)," in IEEE Access, vol. 5, pp. 4000-4017, 2017.

[130] J. Zhang, X. Ge, Q. Li, M. Guizani and Y. Zhang, "5G Millimeter-Wave Antenna Array: Design and Challenges," in IEEE Wireless Communications, vol. 24, no. 2, pp. 106-112, April 2017.

[131] National Telecommunications and Information Administration, "Radars and the Electromagnetic Spectrum". [Online]. Available:

https://www.ntia.doc.gov/legacy/osmhome/reports/ntia00-40/chapt3.htm. [Accessed: 21-2-2018].

[132] Z. Pi, F. Khan, "An introduction to millimeter-wave mobile broadband systems", IEEE Commun. Mag., vol. 49, no. 6, pp. 101-107, Jun. 2011.

[133] E. Rouvalis, M. J. Fice, C. C. Renaud, A. J. Seeds, "Optoelectronic detection of millimetre-wave signals with travelling-wave uni-travelling carrier photodiodes", Opt. Express, vol. 19, no. 3, pp. 2079-2084, Jan. 2011.

[134] 4G Americas, "5G spectrum recommendations". [Online]. Available: http://www.5gamericas.org/files/9114/9324/1786/5GA_5G_Spectrum_Recommendations_2017_FINAL.pdf. [Accessed: 21-4-2018].

[135] M. Natrella, E. Rouvalis, C. P. Liu, H. Liu, C. C. Renaud, A. J. Seeds, "InGaAsP-based uni-travelling carrier photodiode structure grown by solid source molecular beam epitaxy", Opt. Exp., vol. 20, no. 17, pp. 19279-19288, 2012.

[136] C. C. Renaud, M. Natrella, C. Graham, J. Seddon, F. Van Dijk and A. J. Seeds, "Antenna Integrated THz Uni-Traveling Carrier Photodiodes," in IEEE Journal of Selected Topics in Quantum Electronics, vol. 24, no. 2, pp. 1-11, March-April 2018.

[137] H. Fushimi, T. Furuta, T. Ishibashi, H. Ito, "Photoresponse nonlinearity of a uni-traveling-carrier photodiode and its application to optoelectronic millimeter-wave mixing in 60 GHz band", Jpn. J. Appl. Phys., vol. 43, pp. L966-L968, Jul. 2004.

[138] Friis Transmission Calculator. [Online]. Available: https://www.pasternack.com/t-calculator-friis.aspx. [Accessed: 14-May-2019].

[139] ITU-T Recommendation G.975.1, "Forward error correction for high bit-rate DWDM submarine systems". [Online]. Available: https://www.itu.int/rec/T-REC-G.975.1-200402-I/en. [Accessed: 14-May-2019].

[140] I. Fatadin, “Estimation of BER from Error Vector Magnitude for Optical Coherent Systems,” Photonics, vol. 3, pp. 21, 2016.

[141] H. Shams, M. J. Fice, K. Balakier, C. C. Renaud, F. van Dijk, and A. J. Seeds, “Photonic generation for multichannel THz wireless communication,” Opt. Express, vol. 22, no. 19, pp. 23465–23472, 2014.

[142] R. Sobot, “Electrical noise: solutions”, in Wireless Communication Electronics by Example, Springer International Publishing, 2014, ch. 15, pp. 135.

[143] H. Friis, “Noise Figures of Radio Receivers,” Proc. IRE, vol. 32, no. 7, pp. 419–422, 1944.

[144] Fairview Microwave, "1.0 mm Female to 1.85mm Male Adapter," [Online]. Available: https://www.fairviewmicrowave.com/images/productPDF/SM3974.pdf. [Accessed: 14-May-2019].

[145] SHF Communication Technologies AG, "Preliminary Datasheet SHF BT110 Broadband Bias-Tee”. [Online]. Available: https://www.shf-communication.com/wp-content/uploads/datasheets/datasheet_shf_bt110.pdf. [Accessed: 14-May-2019].

[146] Product Overview, "Agilent 8510XF Vector Network Analyzer Single-Connection, Single-Sweep Systems,” . [Online]. Available: https://www.omlinc.com/images/pdf/Library/Application_Notes/Agilent5965-9888_8510XF_VNA_Single_Connection_Single_Sweep_System.pdf. .

[147] A. Baylón-Fuentes, P. Hernández-Nava, A. García-Juárez, I. E. Zaldívar-Huerta, J. Rodríguez-Asomoza, G. Aguayo-Rodríguez, and R. Gómez-Colín, “Modulation of relaxation oscillation frequency of a DFB laser by using direct detection,” Broadband Access Communication Technologies V, 79580E, 2011.

[148] R. Paschotta, “Relaxation Oscillations,” RP Photonics Encyclopedia - relaxation oscillations, solid-state laser, class A, class B regime, spiking, 20-Oct-2018. [Online]. Available: https://www.rp-photonics.com/relaxation_oscillations.html. [Accessed: 14-May-2019].

[149] A. W. Mohammad, H. Shams, K. Balakier, C. Graham, M. Natrella, A. J. Seeds, and C. C. Renaud, “5 Gbps wireless transmission link with an optically pumped uni-traveling carrier photodiode mixer at the receiver,” Optics Express, vol. 26, no. 3, p. 2884, 2018.

[150] A. W. Mohammad et al., "1 Gbaud QPSK wireless receiver using an opto-electronic mixer," 2017 International Topical Meeting on Microwave Photonics (MWP), Beijing, 2017, pp. 1-3.

[151] A. W. Mohammad et al., "60-GHz Transmission Link Using Uni-Traveling Carrier Photodiodes at the Transmitter and the Receiver," in Journal of Lightwave Technology, vol. 36, no. 19, pp. 4507-4513, Oct.1, 2018.

[152] Ofcom, "United kingdom frequency allocation table", no. 18, Jan. 2017.

[153] Marki Microwave, "GaAs Double balanced mixer: MM1-2567LS". [Online]. Available: https://www.markimicrowave.com/Assets/DataSheets/mm1-2567LS.pdf.

[154] G. Zhou, W. Ebert, S. Mutschall, A. Seeger, P. Runge, Q. Li, A. Beling, "High-Power Waveguide Integrated Modified Uni-Traveling-Carrier (UTC) Photodiode with 5 dBm RF Output Power at 120 GHz", Optical Fiber Communications Conf. Exhib., 2016.

[155] C. C. Renaud, M. J. Fice, L. Ponnampalam, M. Natrella, C. Graham, A. J. Seeds, "Uni-travelling carrier photodetectors as THz detectors and emitters", Proc. SPIE, vol. 9370, Aug. 2015.

[156] A. W. Mohammad et al., "60 GHz Wireless Link Implementing an Electronic Mixer Driven by a Photonically Integrated Uni-Traveling Carrier Photodiode at the Receiver," 2018 International Topical Meeting on Microwave Photonics (MWP), Toulouse, 2018, pp. 1-4.

[157] A. Tomkins et al., "A 60 GHz, 802.11ad/WiGig-Compliant Transceiver for Infrastructure and Mobile Applications in 130 nm SiGe BiCMOS," in IEEE Journal of Solid-State Circuits, vol. 50, no. 10, pp. 2239-2255, Oct. 2015.

[158] K. Okada et al., "Full four-channel 6.3-Gb/s 60-GHz CMOS transceiver with low-power analog and digital baseband circuitry", IEEE J. Solid-State Circuits, vol. 48, no. 1, pp. 46-65, Jan. 2013.

[159] C. Dehos, J. L. González, A. D. Domenico, D. Kténas and L. Dussopt, "Millimeter-wave access and backhauling: the solution to the exponential data traffic increase in 5G mobile communications systems?," in IEEE Communications Magazine, vol. 52, no. 9, pp. 88-95, September 2014.

Appendices

A.1: MATLAB Code for QPSK Data Recovery

```
%% This code is for QPSK demodulation and EVM estimation
close all; clear; clc;

%% Parameters
    fs_scope=80e9;
    BaudRate=10e9;
    M=4; %QPSK            % Size of signal constellation
    patt='PRBS_11.mat';
    fIF=9.4e9;              % Upconversion frequency
    Filter='RRC';          % 'Square' Filter, 'Butter', 'RRC', 'Bessel', or 'No Filter'
    FiltBW=2*BaudRate;      % Filter BW for square Filter
    BPFilter=2*BaudRate;  %BasePand Filter for square Filter
    BBBW=2*BaudRate;        % Baseband Bandwidth fitler

%--------------Calculation based on the Parameters-----------------------%
t_symbol=1/BaudRate;
Samples_per_Symbol=floor(fs_scope/BaudRate);
load(patt,'pattern');
Patt_Leng=length(pattern);
k = log2(M);               % Number of bits per symbol
% RRC filter
RRC.beta=0.1;              % roll off factor for RRC
RRC.spans=20;               % no.of symbols
RRC.sps=Samples_per_Symbol; % Samples per symbol
RRC.shape='sqrt';         % 'normal'; %shape 'normal' or 'sqrt'

n=5; W=BaudRate;
%Wo is the frequency up to which
%the filter's group delay is approximately constant.
 % n filter order

%% Resample to Rsamp_sig
fs_sig=Samples_per_Symbol*BaudRate;
Rec_waveform=resample(Rec_waveform,fs_sig,fs_scope);

%% signal normalize & plotting
Rec_waveform=load('M:\COTs\Results\Experiment\optical coherent tunning\rx.mat');
Rec_waveform_norm=Rec_waveform/max(Rec_waveform);
Rec_waveform_norm=Rec_waveform_norm-mean(Rec_waveform_norm);
t=(0:1/fs_sig:(length(Rec_waveform_norm)-1)/fs_sig)';
[pout,f]=pwelch(Rec_waveform_norm,[],[],[],fs_sig,'centered','power');
figure;plot(f/1e9,10*log10(pout));
legend('After Signal Normalization and DC blocker')
xlabel('Freq(GHz)');ylabel('Power(dB)');grid;
title('Received waveform IQ baseband signal','FontSize',14,'color','r');
axis([0 40 -140 -10])

%% Data length and sampling rate.
N_Samples=length(Rec_waveform_norm);
N_Symbols=floor(N_Samples/Samples_per_Symbol);
dtr=1/fs_sig;
N_Patts=floor(N_Symbols/Patt_Leng);
N_Symbols=N_Patts*Patt_Leng;  % New number of symbols for received No. patterns.
NumPoints=N_Symbols*Samples_per_Symbol;


%% Applying BPFilter before DC
```

```
waveform_BPF=SquareFilter(Rec_waveform_norm,dtr,BPFilter,fIF,2);
[pout,f]=pwelch(waveform_BPF,[],[],[],fs_sig,'centered','power');
figure;plot(f/1e9,10*log10(pout));

%% DownConversion into BB Signal
rec_waveform_DC=DC_Mixer(waveform_BPF,t,fIF,BBBW,2);

%% Applying LPF at the recievers
if strcmp(Filter,'Square')
   rec_waveform_LPF=SquareFilter(rec_waveform_DC,dtr,FiltBW,0,2);
elseif strcmp(Filter,'Butter')
   ftype='low';
   ButterOrder=2;
   Butt_BW=2*BaudRate/(fs_sig/2);

% Baseband filter bandwidth (fcut_off)/(fs/2)
   [d,c] = butter(ButterOrder,Butt_BW,ftype);
% Using Butterworth Filter with order
   rec_waveform_LPF=filter(d,c,Rec_waveform_norm);
elseif strcmp(Filter,'RRC');

%downsampling to match the transmitter
%     AWG_sampling=50e9;
rec_waveform_DC=resample(rec_waveform_DC,AWG_sampling/BaudRate,Samples_per_Symb
ol);

%RRC.sps=AWG_sampling/BaudRate;
   rec_waveform_LPF=RRC_Filter(rec_waveform_DC,RRC);

elseif strcmp(Filter,'Bessel');

   % Using Bessel filter
[z,p,l] = besself(n,W);        % Lowpass filter prototype
[num,den] = zp2tf(z,p,l);       % Zero and pole to Transfer function.data3
% freqs(num,den)
[numd,dend]=bilinear(num,den,fs_sig/10); % analog to digital Transfer function
 rec_waveform_LPF=filter(numd,dend, rec_waveform_DC);%data_filt1=data_filt1(2*n+1:end);

elseif strcmp(Filter,'No Filter');
   %% No Filter
   rec_waveform_LPF=rec_waveform_DC;
end

%% Downsampling into 2Samples/sec
rec_waveform_DS=resample(rec_waveform_LPF,2,Samples_per_Symbol);

%% Baseband waveform Normalization;
BBand_waveform=rec_waveform_DS-mean(rec_waveform_DS);
BBand_waveform=BBand_waveform/max(BBand_waveform);
% BBand_waveform=rec_waveform_DS./max(abs(rec_waveform_DS));

% Equalizer using CMA
   N_taps=21;
   Step_size=[0.01 0.001 0.0001];
   rec_QPSKsymbols=QPSK_CMA(BBand_waveform,N_taps,Step_size);

% frequency offset estimation;
   rec_QPSK_FO=FOE(rec_QPSKsymbols,t_symbol);
   scatterplot(rec_QPSK_FO)
```

```
% Phase rotation
     BL=100; %block length
   CPE_QPSKsymbols=CPE(rec_QPSK_FO,BL,M);

% Decision Directed
    step_vector=[0.01 0.001 0.0001];
    taps=41;
    eq_signal=QPSK_decision(CPE_QPSKsymbols,taps,step_vector);
    scatterplot(eq_signal);grid

% BER Measurements
    BER=QPSK_BER(eq_signal,patt);
    EVM=EVM_calc(eq_signal,log2(M));
```

A.2: MATLAB Code for OOK Data Recovery

```
% This code is for OOK demodulation and BER count
t=rec_signal.t;
Signal=rec_signal.signal;
plot(t,Signal);
fs_scope=80e9;
BaudRate=0.5e9;
t_symbol=1/BaudRate;
dt=1/fs_scope;
Samples_per_Symbol=fs_scope/BaudRate;
BBBW=BaudRate*2;
Patt='PRBS_11.mat';
load(Patt,'pattern');
Patt_Leng=length(pattern);

set = 0
cat = 0
fIF=        11.99e+09
for fIF = 12.05e+09:10e6:12.1e+09
 set= set+1
% Upconversion frequency
Rec_waveform_norm=Signal/max(Signal);
Rec_waveform_norm=Rec_waveform_norm-mean(Rec_waveform_norm);
t=(0:1/fs_scope:(length(Rec_waveform_norm)-1)/fs_scope)';
[pout,f]=pwelch(Rec_waveform_norm,[],[],[],fs_scope,'centered','power');
figure;plot(f/1e9,10*log10(pout));
legend('After Signal Normalization and DC blocker')
xlabel('Frequency (GHz)');ylabel('Power(dBm)');grid;
title('Received waveform IQ baseband signal','FontSize',14,'color','r');
axis([0 40 -140 -10])

%% Envelope detection
waveform_BPF=real(SquareFilter(Rec_waveform_norm.*exp(1j*2*pi*10e9),dt,1.0*BBBW,fIF,
2));
[pout,f]=pwelch(waveform_BPF*exp(-j),[],[],[],fs_scope,'centered','power');
figure;plot(f/1e9,10*log10(pout));
Signal_ED=real(sqrt(2*(waveform_BPF).^2));
[pout,f]=pwelch(Signal_ED,[],[],[],fs_scope,'centered','power');
figure;plot(f/1e9,10*log10(pout));
legend('After Signal Normalization and DC blocker')
xlabel('Freq(GHz)');ylabel('Power(dB)');grid;
title('Received waveform IQ baseband signal','FontSize',14,'color','r');
axis([0 40 -140 -10])

waveform_LPF=SquareFilter(Signal_ED,dt,1.2*BBBW,0,2);
[pout,f]=pwelch(waveform_LPF,[],[],[],fs_scope,'centered','power');
figure;plot(f/1e9,10*log10(pout));
figure;plot(waveform_LPF);
waveform_norm=waveform_LPF-mean(waveform_LPF);
figure;plot(waveform_norm);

% Downsampling into 2Samples/sec
rec_Data_DS=resample(waveform_norm,2,Samples_per_Symbol);

% Data Normalization;
rec_Data_AC=rec_Data_DS-mean(rec_Data_DS);
rec_Data_Norm=rec_Data_AC/max(rec_Data_AC);
```

```
% Equalization using CMA

count = 0;
X(1:501)= 10000;
N_taps=5;
for N_taps = 1:2:101
Step_size=[0.005 0.0001 0.000000001];
rec_BPSKbits=BPSK_CMA(rec_Data_Norm,N_taps,Step_size);
eyediagram(rec_BPSKbits,3,3*10^-9)                                    % EYE DIA

% Received Pattern
hDem_bpsk=comm.BPSKDemodulator;
rec_bits=step(hDem_bpsk,rec_BPSKbits);

%% Bit error rate checking
N_Patts=floor(length(rec_bits)/Patt_Leng);
N_Symbols=N_Patts*Patt_Leng;
rec_bits=rec_bits(1:N_Symbols);
patt_in=repmat(pattern,N_Patts,1);
Tx_bits=[patt_in 1-patt_in];
for col=1:2;
Trans_bits=Tx_bits(:,col);
xx=xcorr(Trans_bits,rec_bits);
% figure;plot(xx)
[x_max_value, x_Index]=max(xx);
x_Index_shift=length(patt_in)-x_Index;
Isync=circshift(rec_bits,[-x_Index_shift 0]);

% Calculate BER
% Error detection
Er_BPSK(col)=sum(abs(Isync-Trans_bits));
end
error=min(Er_BPSK);
timebase=dt*length(t);
BER=error/(length(Isync));
 X(N_taps)=error;
fprintf('Pattern Type %s \n',Patt)
fprintf('Time window =%d \n',timebase);
fprintf('No. of Symbols=%d \n Min Error Rate =%e \n',N_Symbols,1/N_Symbols);
fprintf('Number of errors = %d \n Error rate = %e\n', ...
     error, BER);
end
cat(set) = min(X);
end
  close all
min(cat)
```